



UNIVERSITEIT • STELLENBOSCH • UNIVERSITY
jou kennisvennoot • your knowledge partner

In-core Temperature Measurement for the PBMR Using Fibre-Bragg Gratings

by

Gerrit Johannes de Villiers



*Thesis presented at the University of Stellenbosch in
partial fulfilment of the requirements for the degree of*

Masters of Engineering

Department of Electrical Engineering
University of Stellenbosch
Private Bag X1, 7602 Matieland, South Africa

Study leader: Mr. J. Treurnicht

March 2009

Declaration

I, the undersigned, hereby declare that the work contained in this thesis is my own original work and that I have not previously in its entirety or in part submitted it at any university for a degree.

Signature:

G.J. de Villiers

Date:

Copyright © 2009 University of Stellenbosch
All rights reserved.

Abstract

The PBMR has called for research into the possibility of distributed in-core temperature measurement. In this thesis, several methods for distributed temperature measurement in high-pressure, -radiation and -temperature environments have been investigated by means of a literature study. The literature study has revealed FBG temperature sensors as the most feasible solution to the temperature measurement challenge.

Various parameters affecting the propagation of light in optical fibres and consequently the FBG reflection profile was researched. The differential equations describing FBG structures were solved and implemented in Matlab in order to simulate WDM of a distributed FBG sensing system. Distributed sensing with apodized FBGs written in sapphire optical fibre show the most promise of becoming a solution to the measurement challenge.

However, practical testing of sapphire FBGs exposed to the environment in the PBMR core is required. With this long-term goal in mind, a general test platform for FBG temperature sensors was assembled. A heater controller was built for a specialized fibre heating element capable of controlling the temperature of a single FBG up to 1600°C. Temperature measurement using wavelength division multiplexing of apodized FBGs written in silica optical fibre were demonstrated in the test platform with great success. The measured results corresponded very well with the theory.

Finally, the implementation of FBGs in the PBMR is discussed and recommendations are made for future work.

Opsomming

Die PBMR benodig navorsing op die moontlikheid van 'n verspreide temperatuur sensor in die reaktor-kern. In die tesis was verskeie metodes van verspreide temperatuur meting in hoe druk, radiasie en temperatuur omgewings nagevors. 'n Ekstensiewe literatuurstudie het daarop gewys dat FBG temperatuur sensors die beste oplossing vir die toepassing is.

Verskeie parameters wat die propagasie van lig in die optiese vesel en dus ook die FBG refleksie spektrum affekteer is ondersoek. Die differensiele vergelykings wat die FBG se refleksie spektrum beskryf was opgelos en geïmplimenter in Matlab sodat golflengte gemoduleerde verspreide FBG temperatuur stelsels gesimuleer kan word. Verspreide temperatuur meting met *apodized* FBGs geskryf in saffier vesel toon die meeste potentiaal om 'n oplossing te wees vir die temperatuur meting probleem.

Praktiese toetse op saffier FBGs wat blootgestel is aan die omgewings parameters teenwoordig in die PBMR kern word verlang. Met hierdie langtermyn doelwit in gedagte was 'n algemene toetsplatform vir FBGs opgestel. 'n Beheerstelsel vir 'n gespesialiseerde vesel verhittings element was gebou wat in staat is om die temperatuur van n enkele FBG tot en met 1600°C te kan beheer. Golflengte gemoduleerde *apodized* FBGs wat in silikon vesel geskryf is was getoets op die FBG toets platform met groot sukses. Die gemete resultate korrespondeer baie goed met die gesimuleerde refleksie patrone.

Ten slotte word die implementering van FBGs in die PBMR ondersoek en voorstelle gemaak vir werk wat nog gedoen moet word.

Acknowledgements

The author would like to thank the following people for their contribution towards this project:

- My Parents, Piet and Louise. Thank you for supporting me on every possible level. But most of all, thank you for giving me a place that I can always call home.
- Cobie and Mari. A brother could not wish for better sisters than the two inspiring ones I have.
- Mr. J. Treurnicht for his patience and valuable insight.
- PBMR for their financial support and making this project possible.
- My creator, Jesus Christ, to whom I dedicate all of my life.

Romans 1:20 *For ever since the creation of the world His invisible nature and attributes, that is, His eternal power and divinity, have been made intelligible and clearly discernible in and through the things that have been made.*

Contents

Declaration	i
Abstract	ii
Opsomming	iii
Acknowledgements	iv
Contents	v
Nomenclature	viii
List of Figures	xiii
List of Tables	xx
1 Introduction	1
1.1 Background for Conducting the Research	1
1.2 Problem Definition	2
1.3 Objectives of This Study	3
1.4 Outline of Work	4
2 Temperature Sensors	8
2.1 Introduction	8
2.2 Thermocouples	10
2.3 Johnson Noise Thermometry	16
2.4 Optical Fibre Temperature Sensors	21
2.5 Conclusion	33

3	Optical Fibres	35
3.1	Light Propagation in an Optical Fibre	35
3.2	Intermodal and Chromatic Dispersion	41
3.3	Mechanisms of Attenuation	43
3.4	Noise in Optical Fibres	51
3.5	Sapphire Optical Fibre	53
4	Fibre-Bragg Gratings	58
4.1	FBG Modelling and Simulation	58
4.2	Radiation Effects on FBG Sensing Systems	73
4.3	Distributed Sensing	77
4.4	FBG System Design Considerations	79
4.5	Conclusion	80
5	Test Platform	82
5.1	FBG Test Setup Overview	82
5.2	Optical Instrumentation Selection	84
5.3	Heating Element Selection	87
5.4	Heater Controller Design	89
5.5	Operating Conditions	104
5.6	Safety	108
6	FBG Measured Results	109
6.1	FBG Test Setup	109
6.2	Performing Measurements with the Agilent HRS	111
6.3	Optical Fibre Calibration and Characterization	115
6.4	Measurements in the Fibheat 200	124
6.5	Interpretation of Results	131
7	Temperature Sensing in the PBMR Using FBGs	133
7.1	Equipment Selection and Design	133
7.2	FBG Interrogation and Demodulation	144
8	Conclusion	147
8.1	Future Work	148
	Appendices	151

<i>CONTENTS</i>	vii
A HRS Wiring Diagram	152
B Software Flow Diagrams	154
C Matlab Code	159
D C++ Code	161
Bibliography	165

Nomenclature

Greek Letters

τ	Thomson effect
σ_M	Absolute Seebeck coefficient
λ	Wavelength
λ_L	Free-space wavelength of the forward propagating light
λ_B	Bragg wavelength
λ_d	Design peak reflection wavelength for a weak grating
ϵ	Strain or permittivity of the medium
φ_0	Phase of the laser light source or grating chirp model
Λ	FBG period
θ_{crit}	Acceptance angle
μ	Permeability of the medium
μ_0	Permeability constant in a vacuum
κ	Propagation constant of light in the x-axis
β	Propagation constant of light along the fibre length (z-axis) or coupling between propagating modes
Γ	Wavenumber
α	Attenuation
ξ^+	General DC self coupling coefficient
ξ	Absorption loss in FBG
δ_d	Detuning parameter

Small Letters

k	Boltzman's constant
-----	---------------------

e	Electrical charge
v_B	Brillouin shift
n	Refractive index
n_{eff}	Effective refractive index
n_{cl}	Refractive index of the cladding
n_{co}	Refractive index of the core
v_A	Acoustic velocity
x_0	Phase of the laser light source
k_i	Incident wavevector
k_s	Reflected wavevector
s	Fringe visibility
ν	Poissons ratio
p	Strain optic constant
t_{meas}	Measurement time

Capital Letters

S	Seebeck coefficient
P	Pressure
E_{FO}	Fermi energy at 0K
L	Fibre length
M	Number of optical modes travelling in a fibre
A	Rayleigh scattering coefficient
K	Grating wavevector
A_m	Varying amplitude of the m th mode in the positive direction
B_m	Varying amplitude of the m th mode in the negative direction
A^+	Amplitude of the forward propagating wave
B^+	Amplitude of the backward propagating wave
C_{qm}^T	Transverse coupling coefficient
C_{qm}^L	Longitudinal coupling coefficient
R	Resistance or reflectivity
D	Distance between successive gratings

T_{abs}	Absolute temperature of the material
D	Distance between successive gratings
R_T	Calibrated Resistance

Acronyms

ADC	Analog to Digital Converter
APD	Avalanche Photo Diode
BNC	Bayonet Neill Concelman
CAD	Computer Aided Graphics
CMOS	Complimentary metal-oxide-semiconductor
CSV	Comma Separated Values
DAQ	Data Acquisition
DC	Direct Current
DTS	Distributed Temperature Sensor
DPP	Demonstration Power Plant
DUT	Device Under Test
EDFFG	Edge-defined Film-fed Growth
EMF	Electromotive Force
EMI	Electromagnetic Interference
FBG	Fibre-Bragg Grating
FC/APC	Fibre Connector / Angled Polished Connection
FFPI	Fibre Fabry-Perot Interference
FPE	Final Prediction error
FWHM	Full Width Half Maximum
GA	Genetic Algorithms
GPIB	General Purpose Interface Bus
GUI	Graphic User Interface
HRS	High Resolution Spectrometer
IAEA	International Atomic Energy Agency
ICDS	In Core Delivery System
IEEE	Institute of Electrical and Electronics Engineers

IR	Infrared
IST	Imaging & Sensing technology for nuclear systems
ITER	International Thermonuclear Experimental Reactor
JNT	Johnson Noise Thermometry
LAN	Local Area Network
LED	Light Emitting Diode
LHPG	Laser Heated Pedestal Growth
LCD	Liquid-crystal Display
MHI	Micropyretics Heaters International
NBOHC	Non-bridging Oxygen Hole Centres
OD	Optical Density
ORNL	Oak Ridge National Laboratory
OSA	Optical Spectrum Analyzer
PBMR	Pebble Bed Modular Reactor
PC	Personal Computer
PID	Proportional Integral Derivative
PSD	Power Spectral Density
PWM	Pulse Width Modulation
RCD	Resistor, Capacitor and Diode
RF	Radiofrequency
RIA	Radiation-induced Attenuation
RL	Radioluminescence
RMS	Root Mean Square
RTD	Resistance Temperature Detectors
SBS	Stimulated Brilluin Scattering
SID	System Identification
SLS	Side Lobe Suppression
SNR	Signal to Noise Ratio
SSE	Source Spontaneous Emission
SSI	Synchronous Serial Interface
SWI	Swept Wavelength Interferometry

TDM	Time Division Multiplexing
TE	Transverse Electric
TLS	Tunable Laser Source
TM	Transverse Magnetic
USB	Universal Serial Bus
UV	Ultraviolet
WDM	Wavelength Division Multiplexing

List of Figures

1.1	Literature study work breakdown.	5
1.2	FBG test setup work breakdown.	6
1.3	Final measurement system illustrating the technical challenges addressed and work done.	7
2.1	Nuclear core temperature sensing system.	10
2.2	A possible setup using thermocouples to measure the temperature inside the PBMR nuclear core.	15
2.3	Basic Johnson noise thermometry system. Note the parallel measurement of Johnson noise and DC resistance.	17
2.4	A modern JNT setup similar to the system developed by the ORNL.	20
2.5	General block diagram illustrating the core elements of a fibre-optic sensor.	21
2.6	An illustration of a fluorescence decay signal.	27
2.7	The general operation of an FBG.	30
2.8	FBG distributed temperature sensing. Note that the dashed lines on the fibre illustrates individual FBGs.	32
3.1	Geometrical structure of a step index optical fibre.	36
3.2	Light propagation in a multimode fibre.	36
3.3	Wave propagation in an optical fibre illustrating the magnetic field constituents.	38
3.4	The effects of chromatic dispersion on a rectangular pulse traveling in an optical fibre. A rectangular pulse has several high-order frequency components and is therefore exceptionally susceptible to chromatic dispersion.	43

3.5	Radiation-induced attenuation for dry silica fibres with polymer and metal jackets [10].	49
3.6	Radiation induced attenuation in sapphire fibres for different radiation levels at room temperature [63]. The length of fibre tested was 1 m.	50
3.7	The general structure of RL measured in optical fibres. Dose rate: 5.6 MGy/h. Gamma total dose: 30 MGy. Total neutron flux: 1.01×10^{14} n/cm ² s. Total fluence 2.91×10^{18} n/cm ² [9].	52
3.8	Measured attenuation versus frequency for two (denoted by 1 and 2) sapphire optical fibres [63]. Attenuation is indicated in dB where a 1 m fibre is used.	54
3.9	Measured attenuation versus wavelength for different levels of gamma radiation [63]. Attenuation is indicated in dB where a 1 m fibre is used.	55
3.10	Measured attenuation versus wavelength for different levels of neutron radiation [63]. Attenuation is indicated in dB where a 1 m fibre is used.	56
4.1	Illustrating the change induced in the reflective index to create an FBG in the fibre core.	59
4.2	Illustrating the boundary conditions necessary to solve the coupled mode differential equations.	63
4.3	Uniform FBG with parameters: $n_{\text{eff}} = 1.447$, $\Lambda = 535.5$, $\overline{\delta n_{\text{eff}}} = 0.002$ and $L = 20$ mm.	64
4.4	FBG reflection where the grating length is varied from 3 to 20 mm. The grating parameters are $\Lambda = 535.5$ nm, $\overline{\delta n_{\text{eff}}} = 0.8 \times 10^{-4}$ and $n_{\text{eff}} = 1.447$	65
4.5	FBG reflection where the grating strength is varied from $\overline{\delta n_{\text{eff}}} = 0.5 \times 10^{-4}$ to 5×10^{-4} . The grating parameters are $\Lambda = 535.5$ nm, the length is equal to 10 mm and $n_{\text{eff}} = 1.447$	65
4.6	FBG reflection where the grating period Λ is varied from 535 to 536 nm. The grating parameters are $\overline{\delta n_{\text{eff}}} = 1.5 \times 10^{-4}$, the length is equal to 10 mm and $n_{\text{eff}} = 1.447$	66
4.7	Gaussian apodization of an FBG. Note that the warmer colours indicate a larger change, whereas the cooler colours indicate a smaller change in the refractive index change.	68

4.8	FBG with Gaussian apodization in order to eliminate the reflective side lobes. The parameters of the grating are: $n_{\text{eff}} = 1.447$, $\Lambda = 535.5$, $\overline{\delta n_{\text{eff}}} = 0.002$ and $L = 20$ mm. With a Gaussian parameter $a = 15$	69
4.9	A typical curve illustrating the thermal expansion coefficient change for sapphire fibre versus temperature. This curve is representative of Kyocera sapphire fibres.	71
4.10	The variation of the refractive index for sapphire fibre with temperature. Error bars reflect propagation of measurement errors of the elongation length [24].	72
4.11	The change in centre reflection wavelength of an apodized FBG in a silica fibre with parameters $\Lambda = 535.5$ nm, $\overline{\delta n_{\text{eff}}} = 4 \times 10^{-4}$, $L = 15$ mm and $n_{\text{eff}} = 1.447$. The FBG on the left is at room temperature where the same FBG at 300°C is depicted on the right.	73
4.12	Illustrating the possible effects of RIA and RL on the measured reflection profile of an FBG. The reflection profile of the FBG is attenuated by 50% while the noise added was Gaussian in nature with a mean $\mu = 0.05$ and a standard deviation $\sigma = 0.03$	74
4.13	Illustrating the effect of radiation on four WDM FBGs. Note the lower reflectivity due to RIA and the change in Bragg wavelength although the temperature is kept constant [18].	75
4.14	Illustrating the saturation of the FBG centre frequency shift when irradiated. Also note the how the fibre partially recovers when irradiation is discontinued [17].	76
4.15	Illustrating WDM with FBGs. D_1 to D_k denotes the distance between successive gratings and λ_1 to λ_k denotes the centre reflected wavelength of the individual FBGs.	78
4.16	A simulation illustrating the reflection spectrum of five FBGs on a single fibre. All fibres are Gaussian apodized and have the same parameters, except for the grating period which is from left to right $\Lambda = 535$ nm, 535.7 nm, 536.4 nm, 537.1 nm and 537.8 nm, respectively.	79
4.17	Illustrating the required wavelength separation between FBGs on a single fibre. The FWHM parameter is used as a safety factor.	81
5.1	Test setup configuration.	83

5.2	A CAD drawing of the Fibheat 200 with an optical fibre in red and the steel enclosure.	89
5.3	Heater controller block diagram.	90
5.4	The heater controller and the Fibheat 200 in the containment box. The two red buttons control the duty cycle when in standalone mode. The serial connection, which is not visible, is connected to the PC. The two thick power cables are connected to the heater element and the thin BNC cable is connected to the thermocouple. The green power button is visible in the lower left corner.	91
5.5	An example of the Mosfet configuration in a synchronous buck converter with three Mosfets in parallel.	92
5.6	Circuit diagram of the control system for the heating element. . .	96
5.7	Circuit diagram of the power electronics section of the heater controller.	97
5.8	A screenshot of the Borland C++ control program on the PC. . . .	99
5.9	Current output to the heating element versus duty cycle which will be used as the model derivation data.	100
5.10	Model output compared to the measured output current for the given duty cycle. A second set of data, called the model validation data, was used to verify the model accuracy.	101
5.11	The temperature changes measured in the heating element due to several changes in the current control setpoint. This data will be used as the model derivation data.	101
5.12	The temperature model for the heater versus measured temperature values. With the model provided in Equation 5.4.7, an 88.2% least squares fit was obtained with a pure simulation on the model derivation data.	102
5.13	Current control in the heating element. Note the noise in the current during start-up. The current measurement settles after a while and remains fairly constant.	103
5.14	Functional block diagram in Simulink of the temperature controller for the heating element.	105
5.15	A Simulink simulation illustrating the closed-loop temperature response of the heating element. Due to the coarse control over the duty cycle, the output temperature fluctuates $\pm 1^\circ\text{C}$ around the setpoint.	106

5.16	Temperature control of the heating element. The temperature set-point is changed from 100°C to 200°C to 300°C and back to room temperature.	106
5.17	The Fibheat 200 at 1600°C.	107
6.1	Functional diagram illustrating the test setup.	110
6.2	Illustrating the placement as well as the requested design parameters of the FBGs in the two optical fibres. Note the optical terminators at the fibre ends to minimize back reflections and contain the laser light. The FBGs were manufactured by a company called AOS GmbH situated in Germany.	110
6.3	The test setup during calibration and temperature measurements. In the background we have from left to right the HRS, laser module, control PC for the HRS, Agilent RTD measurement unit, heater controller and the PC from where the heater is controlled. In the foreground is the oil bath in which the the RTD and optical fibres are immersed for calibration. The weather station is not visible.	111
6.4	Illustrating the noise floor as well as the measured spectrum when the laser output is connected to the HRS input. laser sweeping speed was set to 1 nm/s and the laser power was set at 1 mW.	113
6.5	A histogram illustrating the signal to noise ratio of the laser and optical spectrometer. The noise can mathematically be represented by the normal distribution in red with a standard deviation of $\sigma = 0.273$ dB.	114
6.6	Cyclic power variations observed when the laser output is 7.5 mW. The cyclic power variations are minimized by keeping the laser output power below 1 mW.	114
6.7	A screenshot of the Agilent software used to control the laser and HRS. Visible in the screenshot is the typical spectral response of a FBG.	116
6.8	A diagram illustrating the positioning of the platinum RTD and optical fibres within the oil bath. The brass block and oil surrounding it ensures that the RTD and optical fibres are at the same temperature.	117

6.9	Illustrating the measured reflection spectrum of FBG1 at 25.64°C. The simulated reflection profile of a FBG whose parameters were adjusted to best fit the measured FBG is illustrated in red.	118
6.10	The result obtained when the simulated FBG and the measured reflection spectrum is correlated. From this figure it is possible to accurately calculate the Bragg wavelength of the FBG.	120
6.11	The reflection profiles of FBG1 at 25.64°C, 62.36°C and 103.08°C.	120
6.12	Illustrating the measured change in wavelength versus temperature for FBG1 together with Equation 6.3.2.	121
6.13	Illustrating the reflection spectrum of the multiple FBG fibre. The three FBGs are clearly visible and marked accordingly.	122
6.14	The simulation results for each of the FBGs in the multiple FBG fibre is compared to the measured data. In subfigures (a) to (c) the simulation results as well as the measured data is presented in red and blue respectively. Subfigure (d) illustrates the correlation result of FBG2 (red), FBG3 (blue) and FBG4 (green) with their simulation result.	123
6.15	Illustrating the Bragg frequency shift of the FBGs with temperature. The measured Bragg frequencies are in red whereas the blue lines represent the linear Equations 6.3.3 to 6.3.5.	124
6.16	An illustration of the optical fibre inserted in the Fibheat 200. Note the J-type thermocouple in the front that is used to measure the heater temperature.	125
6.17	Illustrating the spectral widening of the FBG reflection profile when the temperature reached 160°C in the Fibheat 200. Please note that the curve in red is FBG1 at 160°C whereas the blue curve was superimposed on the image to provide a visual illustration of the spectral widening.	126
6.18	The blackbody radiation emitted from the Fibheat 200 produced the image and illustrates the temperature gradient present across the length of the inserted fibre.	127
6.19	The FBG and thermocouple is covered in foil to prevent a large temperature gradient across the optical fibre and to ensure that the correct temperature is measured by the thermocouple.	127
6.20	The Bragg wavelength shift of FBG1 versus temperature in the Fibheat 200 heating element.	128

6.21	Illustrating the distribution of the detected Bragg frequency even though the temperature of the FBG is held constant.	130
6.22	The average reflection profile of the FBG1 before any temperature tests were performed is illustrated in blue. An average reflection profile of the same FBG after several temperature cycles were performed is provided in red.	131
7.1	Illustrating the interaction between and effect of temperature, pressure and radiation on the Bragg wavelength of the FBG and how a correction algorithm would be implemented.	137
7.2	Illustrating temperature measurement in the PBMR core and the effect of long FBGs on the measured temperature.	139
7.3	Optical switches can be used to extend the measurement capabilities of the optical spectrometer and laser.	142
7.4	The reflection profile of a distributed FBG cluster on a sapphire fibre when at room temperature and at 1600°C.	143
7.5	Corrupted reflection data of a WDM FBG system. The attenuation is 60% and the noise added is Gaussian in nature with a mean $\mu = 0.06$ and standard deviation $\sigma = 0.2$	145
7.6	Correlation result of five noisy FBGs with their original reflection spectrum.	146
8.1	A diagram illustrating some of the future work required for the PBMR FBG sensor system.	149
8.2	A future vision of the FBG temperature measurement system in the PBMR.	150
A.1	Illustrating the physical connections to the HRS system. Please note that the wiring instructions in the manual is INCORRECT. . .	153
B.1	Software flow diagram of the PIC microcontroller.	155
B.2	Software flow diagram for the interrupt sequence of the microcontroller.	156
B.3	Software flow diagram of the main control program on the PC. . .	157
B.4	Software flow diagram of the automatic control system on the PC. .	158

List of Tables

2.1	Temperature sensing methods not suitable for the PBMR nuclear core.	11
2.2	Selecting the correct temperature sensing technology for the PBMR.	34
5.1	Comparing the most popular FBG interrogation techniques.	85
6.1	Environmental conditions recorded when FBG1 was interrogated on the 9th of November 2008.	117
6.2	The manufacturing values that was found through simulation to best represent the reflection profile of FBG1.	118
6.3	Environmental conditions recorded when the optical fibre with multiple FBGs were analyzed on the 11th of November 2008.	121
6.4	The estimated manufacturing parameters of FBG2, 3 and 4.	122
6.5	Environmental conditions recorded when FBG1 was inserted in the Fibheat 200 heating element on the 14th of November 2008.	125
7.1	The effects that the length of an FBG has on the temperature sensing system as a whole.	138
7.2	How the optical spectrometer and tunable laser source combination are perfectly suited to and will deal with some of the main temperature measurement challenges in the PBMR.	141

Chapter 1

Introduction

This Chapter will serve as an introduction to how the research topic has originated. Background information to the origins of the research is provided as well as a detailed problem definition in order to clearly identify the associated technical difficulties. The objectives for this study is provided next in which the role that this research plays in the project as a whole is outlined. Finally, an outline of the work done will be provided.

1.1 Background for Conducting the Research

The Pebble Bed Modular Reactor (PBMR) project has answered the global need for cleaner and more effective power generation when the company was founded in 1999. At present the project is in its late design stage and construction on the foundations of the Demonstration Power Plant (DPP) has already started at Koeberg South Africa in the beginning of 2007. The PBMR is a first-of-its-kind 400 MWt (165 MWe) helium-cooled nuclear reactor; plant data is therefore not available. A temperature profile of the nuclear core during operation would assist in the improvement of current plant models and the control of the plant itself. A temperature profile of the PBMR core would also be of great interest to the nuclear industry because of its unique design.

In order to address the need for a temperature profile of the PBMR core, it has been suggested to insert multiple temperature sensors along the centre and side reflectors of the nuclear core. This would provide the operators and control systems with real-time temperature measurements that can be used to monitor and optimize plant control. Integrating a thermodynamic

model with several temperature measurements along the reflector wall will in theory allow calculations to be made relating to the positions of the fuel spheres (those pressing against the reflector walls) and consequently their movement and speed through the reactor. Hotspots inside the reactor will cause bending of the citadel; this phenomenon can be closely monitored if temperature measurements are available. The information that a Distributed Temperature Sensor (DTS) inside the core can provide is therefore invaluable.

The DPP will contain an In-core Delivery System (ICDS) that is capable of inserting or removing temperature sensors into machined holes close to the side of the central reflector. Provision has therefore been made for temperature sensors, but unfortunately current technology does not allow accurate temperature measurements in the harsh nuclear environment that is present inside the core. The technical challenges faced when making distributed temperature measurements inside the nuclear core are subsequently the topic of this thesis and the defining feature that makes this work unique.

1.2 Problem Definition

The future vision of this project is that of making accurate temperature measurements inside the PBMR core, but a secondary objective exists: to determine the movement and consequently the speed of the fuel spheres through the core. This project will serve the purpose of identifying and studying a suitable sensor to perform distributed temperature measurement inside the PBMR nuclear core.

Extreme environmental conditions within the PBMR core present the most significant obstacle. The combination of high temperatures, pressures and radiation calls for a specialized measurement technology. Limited space and the immense amount of point measurements required to correctly determine a thermodynamic image of the core poses another engineering challenge.

The secondary objective places an upper limit on the sampling interval or measurement interval. A thermodynamic model, developed by the University of Stellenbosch, will determine the maximum temperature measurement interval in order to discern between consecutive fuel spheres (if possible). By incorporating the model with the temperature measurement data, it is speculated that the speed of the fuel spheres can be determined. For the purposes of this report it is assumed that the sampling interval required for the tem-

perature sensor is half the diameter of the fuel spheres (30 mm, in accordance with Nyquists' sampling theorem).

No stringent requirement is placed on the sampling time of the temperature sensors. Temperature fluctuations along the centre reflector of the core occur primarily because of two factors: (1) The movement of fuel spheres through the core, and (2) variations in the neutron flux resulting in the fission process. The fuel spheres inside the core will move at a maximum average speed of 1 m per day. The thermal capacitance of the graphite spheres and graphite side reflectors filter any fluctuation in the fission process, resulting in maximum predicted temperature gradients of 100°C per hour [62].

Temperature measurement accuracy, on the other hand, must preferably be as accurate as possible, as this parameter will directly affect the probability of distinguishing between consecutive fuel spheres. The exact temperature measurement accuracy required is unknown.

The nuclear power plant will operate for long periods of time without the possibility of servicing the sensors; ruggedness, durability and stability are therefore of utmost importance to ensure continual operation of the temperature sensors. If, however, the temperature sensors are of such a kind that they can be inserted and removed from the core using the ICDS, the stringent requirements on the long-term survivability can be relaxed.

The final requirement is for the data gathered from the temperature sensors to be logged and visually displayed. Practical ways of collecting the data from the array of temperature sensors are necessary. Sensor health will also be a valuable parameter to be monitored/predicted if sensor degradation is expected.

1.3 Objectives of This Study

The objectives of this study are listed as follows:

- The claim made by Luna Innovations that fibre-Bragg gratings (FBGs) can be used as a distributed in-core temperature measurement system must be verified through a literature study. Whether or not FBGs are the most suited temperature measurement technology must also be investigated.

- A general knowledge of optical fibres and FBG temperature measurement is required. This includes a literature study of the effects of radiation, pressure and temperature on the FBG.
- A general test platform for FBG temperature sensors must be assembled. The test platform should preferably be flexible and accurate enough that it would suffice for any future tests of FBGs that the project might require.
- As a first step on the practical side of the project, silica FBGs should be acquired to demonstrate temperature measurement. Wavelength division multiplexing of FBGs in silica must also be demonstrated and the results documented.
- Finally, the test results must be interpreted and conclusions drawn. An outline of how the FBG technology would be applied to the PBMR is also required to identify future technical challenges.

1.4 Outline of Work

In order to achieve the above-mentioned goals, a thorough literature study regarding temperature measurement techniques is required. An overview of the available temperature sensors that shows the relevant potential to perform accurate temperature readings inside of the core is provided in Chapter 2. The overview is comprised of a detail description of the working principles of the sensors where each sensor will be broken down into its constituent parts and evaluated according to the criteria set forth in Section 2.1.

Preliminary technology evaluations by Luna Innovations have identified FBGs as the most promising solution. This fact will be verified as far as possible by means of a literature study. Fibre optics in general were subsequently be the topic of research in the second part of the literature study. Factors influencing the propagation of light signals in fibre optics were discussed, as well as sapphire optical fibres, which have been found capable of withstanding the high temperatures and radiation levels inside the nuclear core. FBGs have been investigated where special attention was paid to their practical operation and characteristics. Figure 1.1 provides a graphical representation illustrating the line of thought and work done concerning the literature study.

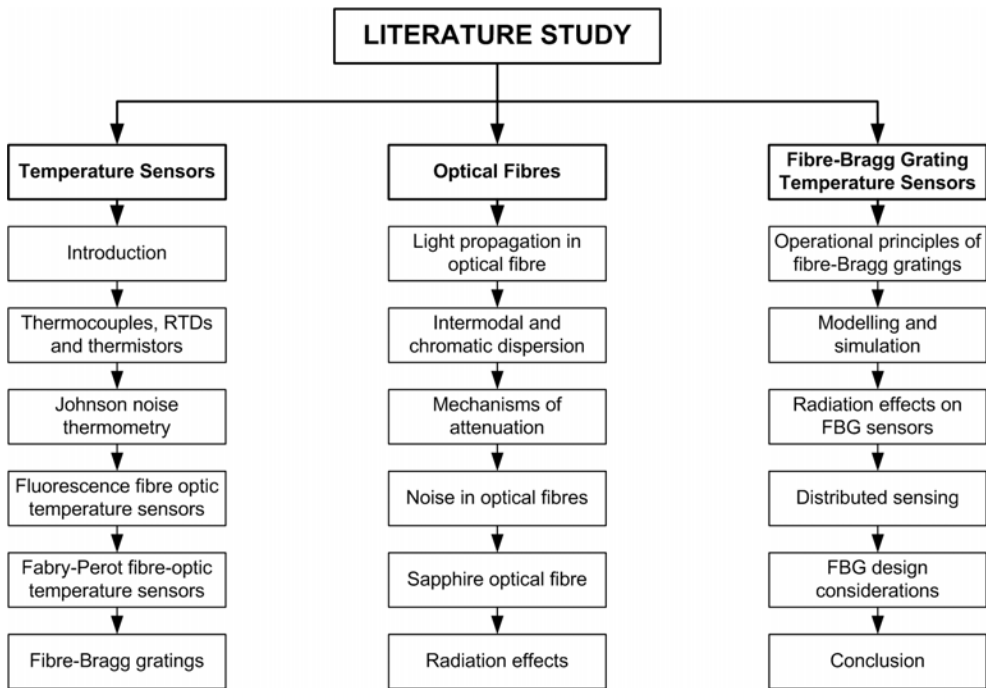


Figure 1.1: Literature study work breakdown.

The knowledge gained through the literature study was further developed and applied in order to find a suitable engineering solution to measure the temperature inside the core using FBGs. In this thesis, certain aspects of the sensor system are investigated in detail, whereas only recommendations are made regarding other foreseen difficulties.

A test setup was constructed in order to characterize the FBGs and correlate the measured data with the theoretically predicted reflection spectra. An optical laser and spectrometer from Agilent form the basis of the test setup constructed. A heating element from MHI was acquired and a power controller constructed that is capable of controlling the temperature of the element by adjusting the electrical power delivered to the heating element. Controlled temperatures up to 1600°C can be achieved by the fibre heating element. An oil bath was used for the accurate temperature calibration of the FBGs and the heating element for high temperature tests.

The mathematical algorithms used to model FBGs were implemented in Matlab and a description of the model derivation is provided in Chapter 4. Other algorithms capable of modelling WDM of FBGs and their response to environmental effects were also implemented and studied. The work break-

down structure of the second part of this thesis is presented in Figure 1.2.

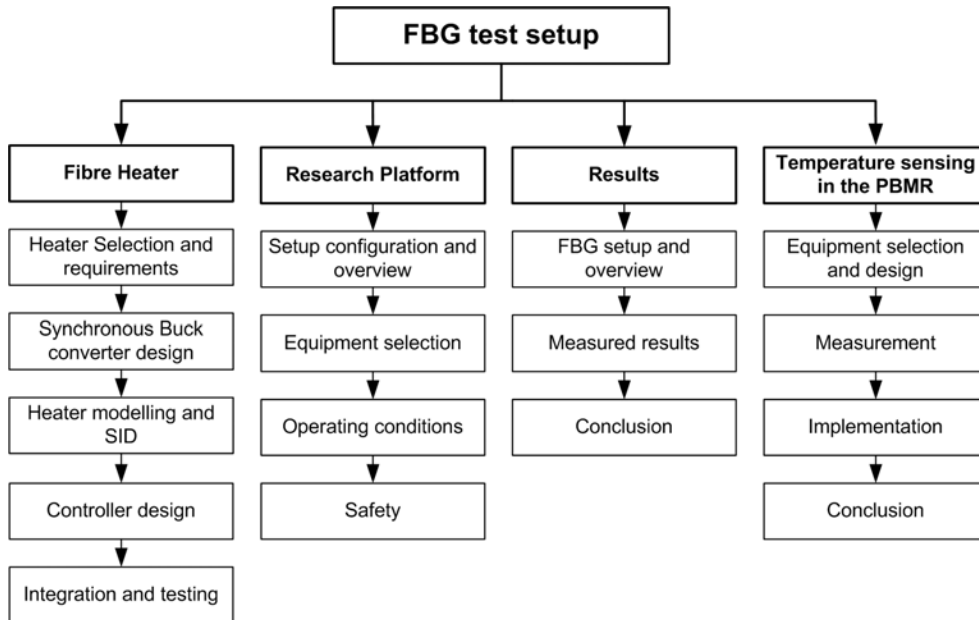


Figure 1.2: FBG test setup work breakdown.

In Figure 1.3, the final measurement system as well as the problems addressed are presented. An overview of the system as well as the work done are provided in Figure 1.3 and discussed in detail in Chapter 5. The selection of the fibre heater and the design of the controller that forms an integral part of the test setup are provided in Sections 5.3 and 5.4, respectively.

The measured results from the FBG test setup can be found in Chapter 6. In Chapter 7, aspects regarding the implementation of the temperature sensor system are discussed and several recommendations are made as to how the sensor system should be implemented. Finally, conclusions are drawn as to the suitability of the FBG technology to the measurement challenge in the PBMR, and several suggestions made for future work.

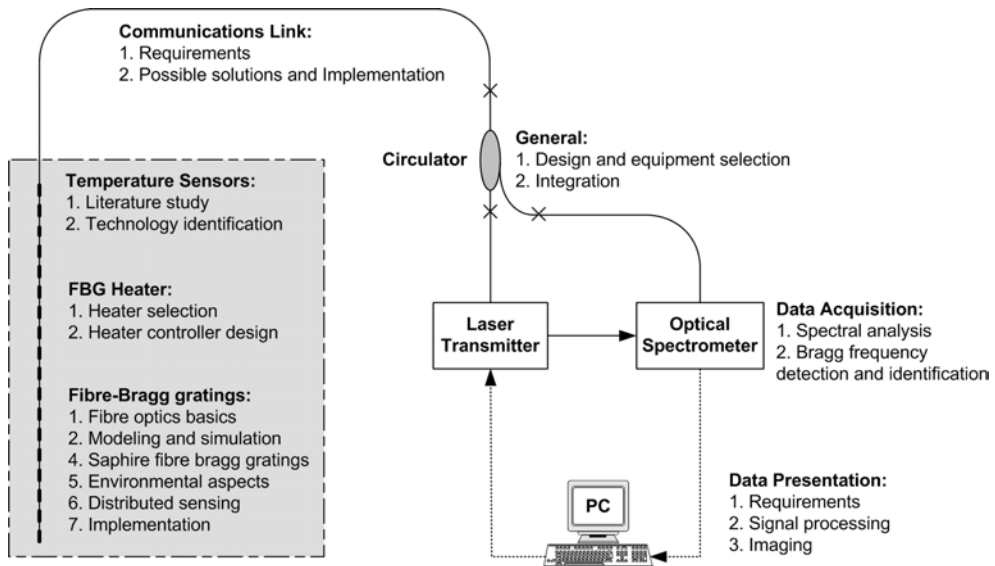


Figure 1.3: Final measurement system illustrating the technical challenges addressed and work done.

Chapter 2

Temperature Sensors

A comprehensive study of presently available as well as emerging temperature sensor technology follows, together with a short description of how these temperature sensors operate. In each case the specified sensor's applicability to solving the core temperature measurement problem will be evaluated, based on the selection guide provided. From the information provided here, FBGs were selected as the preferred in-core temperature sensor and is discussed in further detail in the Chapters to come. A few definitions and basic concepts regarding temperature measurement is presented in the introduction.

2.1 Introduction

Temperature is a measure of the energy of the particles from which the substance is comprised. This energy may be in the form of translational motion of the particle, or as a result of the internal energy due to molecular vibration or the excitation of an electron energy level. Temperature becomes a quantity definable either in terms of macroscopic thermodynamic quantities such as heat and work, or, with equal validity and identical results, in terms of a quantity which characterizes the energy distribution among the particles in a system [54].

The first method of thermal energy transfer from one body to another is through molecular collisions and motions. This method of thermal energy transfer by contact is called conduction. A second method of energy transfer entails bodily movement of higher-energy molecules and is called convec-

tion. Thermal radiation, on the other hand, concerns a form of energy that travels as a vibratory electric and magnetic disturbance through space in a direction perpendicular to the disturbance.

Temperature measurement is generally performed by measuring the effect that these methods of energy transfer have on the temperature sensor; typically some physical property of the temperature sensor is altered and measured. This property change may include the volume occupied by a certain liquid, measuring the electrical noise created over a resistive medium, or the change in the refractive index of an optical fibre. Several factors other than temperature might influence the temperature measurement and are consequently perceived as measurement errors.

When evaluating the different available sensor technologies and their respective applicability to the conditions present in the PBMR, the ability to operate in the following conditions will serve as a selection guide for the temperature sensors:

1. The maximum attainable core temperature in the event of a total loss of coolant is in the order of 1600°C and the sensor must consequently be able to withstand and measure these extreme temperatures. Under normal operating conditions, the core is expected to operate at 900°C .
2. Radiation tolerance is critical. Ionizing neutron radiation, gamma radiation and strong electric fields are prone to influence the correct operation of many types of sensors.
3. Pressure levels inside the core under normal operating conditions may reach 9 MPa and will not necessarily remain constant. It is therefore required that the sensor be relatively insensitive to fluctuations in the ambient pressure.
4. Distributed temperature sensing is required and limited space is available in the shaft for sensors and wiring. Easy removal and insertion of the sensor configuration with the ICDS is desirable.
5. The operational lifetime of the PBMR is estimated at 40 years and it is preferable that in this period the sensor remains fully operational and experiences minimal drift and degradation. Measurement accuracy and stability over the sensor's life cycle is therefore critical.

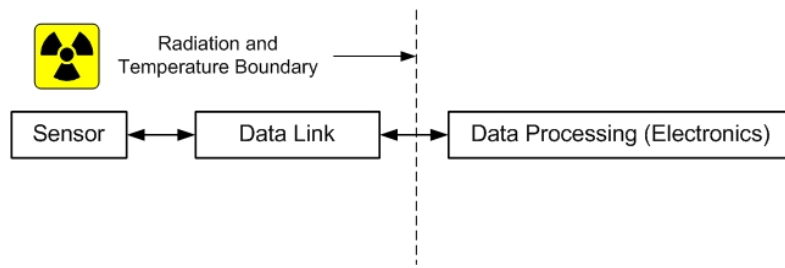


Figure 2.1: Nuclear core temperature sensing system.

Each temperature sensor discussed forms part of the system illustrated in Figure 2.1. The temperature sensor itself has the specific requirements as stated in the paragraphs above, the data link and data processing elements, on the other hand, will be evaluated according to a different set of performance parameters. Undistorted communication between the temperature sensor and the data processing electronics (and vice versa if necessary) is required from the data link. Any interaction between the immediate surroundings and the data link must be kept to a minimum which requires the link to be chemically inert as well as robust and insensitive to high pressures, radiation levels and temperatures. Due to the unnecessarily high cost, testing and amount of time required to issue electronic instrumentation for the nuclear environment, it will be assumed that all of the electronics (data processing) will reside outside of the containment area.

An off-the-shelf commercial solution to the stated problem does not exist as yet, but those technologies that illustrate the most potential in successfully operating in the core will be discussed. Table 2.1 lists some of the most popular temperature sensing methods that could immediately be removed from the list of possible solutions. Reasons for their elimination are also stated.

The temperature sensing methods that illustrate the necessary qualities to present a possible solution to the measurement problem are further discussed in the following Sections. Finally, the different sensor technologies will be compared according to the performance parameters set forth, and a selection made.

2.2 Thermocouples

Thermocouples are one of the most widely used temperature sensors available. In thermocouples the Seebeck effect or thermoelectric effect is fully

Technology	Method of Operation	Reasons for Elimination
RTDs and thermistors (resistive thermometers)	Resistance of the material changes with temperature. A lookup table is then used to determine the temperature.	<ol style="list-style-type: none"> 1. Radiation causes a change in the resistance of metals and the magnitude of change is a complex function of the radiation intensity as well as the temperature during and after irradiation. 2. Gamma ray absorption can lead to localized temperature increases along the resistance wires and results in significant temperature measurement errors. 3. Radiation affects the insulative materials and can introduce shunting errors [12].
Infrared (IR) thermometers	Works on the principle of measuring the distribution of radiated energy from a blackbody, i.e. the measured surface. Blackbody radiation lies predominantly in the IR region of 0.5 – 14 μm .	<ol style="list-style-type: none"> 1. Distributed temperature sensing with multiple blackbody radiators along the core is not practical. 2. Processing the IR radiation requires it to be guided out of the containment area since electronics do not function in the harsh radiation environment. This necessitates fibre optics/ lightpipes to act as a waveguide. Radioluminescence, multipath and radiation-induced attenuation will corrupt the IR data beyond recognition. 3. IR radiation is affected by the emissivity and surface conditions of the graphite or blackbody implemented.
Semiconductor junction thermometers	Relies on the temperature dependence of the pn junction in a transistor. A current is passed through the base emitter current and results in a temperature-dependent voltage between the base and emitter.	<ol style="list-style-type: none"> 1. Accurate temperature measurements can only be made over the temperature range of -55°C to 150°C. 2. The harsh conditions inside the core will destroy the semiconductor pn junction.

Table 2.1: Temperature sensing methods not suitable for the PBMR nuclear core.

exploited. A short description of the working principle of thermocouples follows, after which their tolerance is discussed.

The Seebeck effect describes the situation where a voltage difference occurs between two points on a metal as a result of a temperature difference between these two points. The thermoelectric voltage developed per unit of temperature change in a metal is defined as the Seebeck coefficient and is given by [36]:

$$S = \frac{dV}{dT} \approx \frac{\pi^2 k^2 T}{2eE_{FO}} \quad (2.2.1)$$

where k is defined as Boltzmann's constant, T the absolute temperature in Kelvin, e the electron charge (magnitude only) and E_{FO} the Fermi energy at 0K for the specific metal used. If two metals are joined at one end with the joined junction used to sense the temperature T and the other maintained at a reference temperature T_0 , a potential difference results. The potential difference is proportional to the difference in temperature $\Delta T = T - T_0$ and therefore the difference in the Seebeck coefficients $S_A - S_B$. The measured electromotive force (EMF) between the two wires $V_{AB} = V_A - V_B$ becomes:

$$V_{AB} = \int_{T_0}^T (S_A - S_B) dT = a\Delta T + b(\Delta T)^2 \quad (2.2.2)$$

which results in the familiar thermocouple equation where a and b are thermocouple coefficients dependent on the metals used. It is clear that the difference in Seebeck coefficients between the two metals must preferably be as large as possible in order to obtain a measurable potential difference. This potential difference is typically amplified, passed through a low-pass filter in order to remove high-frequency noise, and the temperature determined from a lookup table or formula. There exists potentially as many thermocouple types as metal alloys, but certain combinations function better than others.

Various types of thermocouple sensors can easily operate in the required temperature range of 200°C to 1600°C [67]. Thermocouples are, however, not radiation-resistant and require proper shielding and special precautions need to be taken in order to reduce the radiation sensitivity. Neutron-induced de-calibration effects of various types of thermocouples are widely noted [19]. Erroneous temperature readings with thermocouples in the PBMR core will occur through three processes, namely (1) structural damage, (2) transmuta-

tion, and (3) electromagnetic fields. These effects will be discussed in further detail in the following paragraphs.

1. Structural damage in the thermocouple wire is as a result of fast neutrons that may cause vacancy clusters or dislocations in the metal structure. These vacancy clusters or dislocations results in changes in the Electromotive Force (EMF) generated and have theoretically been determined to result in errors of 2% at most [47]. This effect is, however, expected to be annealed out at temperatures exceeding 0.6 times the absolute melting point [29] and has also been demonstrated experimentally [43]. Taking into account the above-mentioned fact and the relatively small temperature measurement error of 2%, the error due to this method of radiation-induced decalibration can safely be ignored.
2. The second and most severe method of radiation-induced decalibration occurs through a process called transmutation. Transmutation reactions in thermocouples result in changes in the physical composition of the alloys which in turn result in changes in the homogeneity of the thermocouple [12]. The absolute Seebeck coefficient, σ_M for an individual material is often used to describe its inhomogeneity. The absolute Seebeck coefficient physically exists but is not easily measurable; it can however, be indirectly determined by measuring the Thomson effect, τ , of the specific material and applying the Kelvin effect [67]:

$$\sigma_M = \int_0^{T_{\text{abs}}} \frac{\tau}{T_{\text{abs}}} dT \quad (2.2.3)$$

where T_{abs} is defined as the absolute temperature. The thermocouple drift or instability often experienced in a high-radiation environment is invariably as a result of progressing inhomogeneity. This effect can potentially lead to a thermocouple temperature reading with indefinite uncertainty [56].

3. Strong transient as well as steady electromagnetic fields exist within the nuclear reactor. Varying electromagnetic waves will according to Faraday's law:

$$V_E = \frac{-d\phi}{dt} \quad (2.2.4)$$

create a voltage V_E across the thermocouple wires. The variable ϕ is defined as the magnetic flux. This effect is, however, easily mitigated by twisting the thermocouple wires since the EMF created in different sections of the wires are cancelled out.

Steady magnetic fields, on the other hand, affect the accuracy and stability of thermocouples through three different thermomagnetic methods, namely: (1) Ettingshausen-Nernst effect in a transverse field, perpendicular to the temperature gradient, (2) longitudinal effects, in a transverse and a longitudinal field, and (3) through the Righi-Leduc effect perpendicular to the temperature gradient. In this case, a longitudinal field is defined as being parallel to the thermocouple wires, whereas a transverse field is perpendicular to the thermocouple wires. Changes in the Seebeck coefficient for the material used occur with the longitudinal effects [47].

Only the Ettingshausen-Nernst effect can potentially cause serious errors with thermocouple temperature measurements under the following conditions:

- In the presence of a transverse magnetic field above one Tesla.
- If at least one of the thermocouples wires is ferromagnetic.
- If the thermocouple is operated below the curie temperature of the ferromagnetic wire used.
- When the temperature gradient is perpendicular to the thermocouple wires.

An in-depth discussion of the thermomagnetic effects that influences thermocouples is provided by J.P. Jan [33]. By proper shielding and using non-ferromagnetic materials in the thermocouples, it is possible to make accurate temperature measurements within the harsh environment of the nuclear core. Experiments concluded that the radiation-induced electromotive force generated between the thermocouple wires and sheath has no significant ($< 0.5\%$) effect on the temperature measurement [47].

Recommendations regarding the type of thermocouples to use have been made by Nieuwenhove and Vermeeren [47]: Chromel/Alumel (type K) and Nicrosil/Nisil (type N) thermocouples are recommended for use well below 1300°C since the effect of transmutation in the neutron spectrum of a fission

reactor for these thermocouples is negligible. This assumption was made based on the small cross sections for transmutation reactions at a neutron energy of 14 MeV. For temperature measurements up to 2200°C, tungsten-rhenium thermocouples are recommended.

Commercial in-core thermocouple temperature sensors are available from IST (Imaging & Sensing Technology for Nuclear Systems). IST claims they can manufacture thermocouple assemblies that are able to make accurate and reliable temperature measurements inside a nuclear core. Long-term testing of these thermocouples in a PBMR-like environment has, however, not been done.

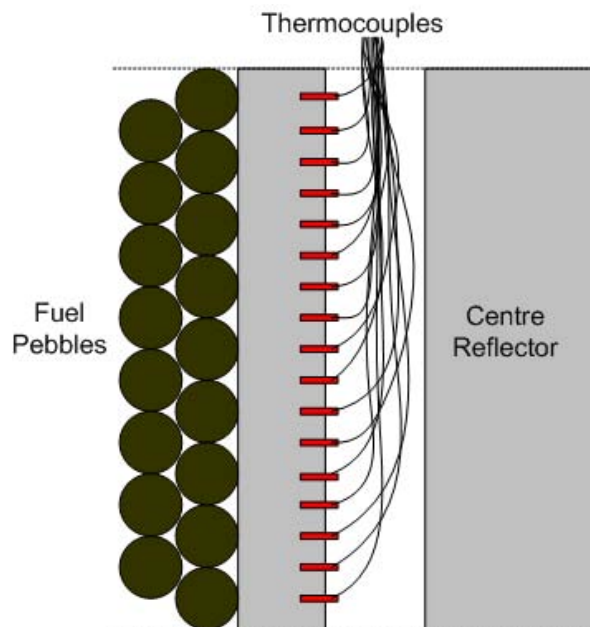


Figure 2.2: A possible setup using thermocouples to measure the temperature inside the PBMR nuclear core.

These radiation-resistant thermocouples could hypothetically be embedded into the wall of the centre reflector, as illustrated in Figure 2.2. The disadvantages of using thermocouples in the configuration illustrated in Figure 2.2 (assuming that accurate temperature measurements can indeed be made) include the fact that the thermocouples cannot easily be removed for inspection or repair. The amount of wiring needed to connect all of the thermocouples to the front end of the signal conditioning unit also presents a significant problem if the entire 25 m shaft down the core is fitted with thermocouples at

intervals of 30 mm. A configuration like this would require 830 thermocouples and 1660 radiation-shielded wires.

2.3 Johnson Noise Thermometry

Temperature sensors in general rely on a change in some physical property of the sensing material (the material in contact with the environment whose temperature is measured) and it is the extent of this property change that is exploited in order to calculate the temperature. Regular calibration of sensors relying on property changes of a sensing material is consequently required since the sensing method does not exclusively rely on the fundamental changes that are synonymous with a change in temperature. Instead, several other changing ambient conditions such as pressure and radiation also have an influence on many material properties used to calculate temperature.

Johnson Noise Thermometry (JNT), on the other hand, relies on the temperature defining random variations of the atomic ensemble within a material. A temperature increase within a material results in an increase in the natural Brownian motion of electrons. This motion results in noise voltage created across any resistance. The noise created is entirely random with a zero mean and amplitude that is directly related to the temperature of the material. The noise power for frequencies below 1 MHz and temperatures above 25 K is given by the Nyquist formula (accurate to within 0.0001%),

$$V_{n,rms} = \sqrt{4kTR_T\Delta f} \quad (2.3.1)$$

where $V_{n,rms}$ is the Root Mean Square (RMS) of the voltage created over the calibrated resistance R_T , k is the Boltzmann's constant 1.374×10^{-23} J/K, T the temperature, and Δf is the equivalent noise bandwidth for the measurement [49].

The basic idea behind JNT is to amplify the Johnson noise over a bandwidth that is, as far as possible, 'clean' from foreign noise sources and, by using Equation 2.3.1, statistically determine the temperature. Johnson noise signals at 300 K over a bandwidth of 100 Hz with a resistance of 300 Ω result in an RMS noise voltage of 2.22×10^{-8} V. Small signals such as these are exceptionally susceptible to Electromagnetic Interference (EMI), triboelectric, piezoelectric and shot noise sources. Band-pass filters and low-noise ampli-

fiers are a must in order to provide Johnson noise that is distinguishable from extraneous sources as those mentioned.

Modern JNT architectures implement the Johnson noise measurement system and the resistance measurement system in parallel [31]. The resistance measurement can provide a quick estimation of the temperature, while the Johnson noise provides an accurate temperature measurement over several measurements. Depending on the bandwidth over which the noise is sampled and the accuracy required, a measurement can take as long as a few days. A mathematical formula for estimating the integration time is provided further in this Section. Figure 2.3 illustrates a basic setup used to measure the Johnson noise over a resistance.

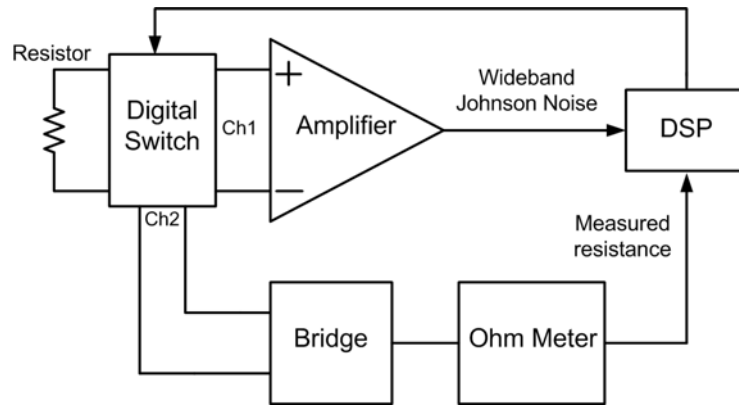


Figure 2.3: Basic Johnson noise thermometry system. Note the parallel measurement of Johnson noise and DC resistance.

Every precaution must be taken to prevent extraneous noise from entering the system. A single amplifier stage is most often used, employing a low-noise topology and a large gain since in any circuit the noise will almost completely be controlled by the transducer and the first amplifier stage.

The front-end amplifier electronics is placed as close as possible to the sensor itself in order to mitigate transmission line effects. Special care must also be taken to ensure that the cable connections are shielded and twisted to further help minimize electromagnetic interference. Typical cables exhibit a capacitance of about 100 pF/m and are usually lengthy since the pre-amplifiers are some distance away from the sensors. The frequency response of the transmission line, $X(f)$, must therefore be incorporated into the measurement as illustrated in Equation 2.3.2.

$$V_T^2 = 4kTR_T \int_0^\infty |X(f)|^2 |H(f)|^2 df \quad (2.3.2)$$

In Equation 2.3.2, $H(f)$ is defined as the frequency response of the bandwidth over which the Johnson noise is measured.

The maximum available bandwidth versus cable length, for example a $100\ \Omega$ resistance that exhibits a noise power loss of less than 0.1%, was examined by Holcomb et al. [32]. The bandwidth for this hypothetical system where the cable length from the resistor to the front-end electronics is 25 m, would be 25 kHz. This would be a very good indication of the available bandwidth for the farthest sensor if such a JNT system is implemented in the PBMR. A smaller bandwidth translates to a longer measurement time before a certain degree of accuracy can be attained since the noise signal is random and must be averaged for long periods of time to eliminate statistical fluctuations. The statistical uncertainty for a single noise power measurement is defined in Equation 2.3.3, where $\sigma_{V_T^2}$ is defined as the noise variance [3].

$$\frac{\sigma_{V_T^2}^2}{V_T^2} = \frac{1}{2t_{\text{meas}}\Delta f_c} \left[\left(\frac{V_T^2 + V_n^2}{V_T^2} \right)^2 + 1 \right] \quad (2.3.3)$$

Equation 2.3.3 can be used to calculate the measurement time required in order to achieve a certain degree of accuracy where t_{meas} is the measurement time, Δf_c is the correlation bandwidth of the system, V_T is the Johnson noise source and V_n is the uncorrelated noise due to the amplifiers and transmission lines. Depending on the JNT system setup the measurement time required to obtain an accuracy of 0.1% with a 25 kHz bandwidth can take anything from a few hours to a few days. Considering that the temperature inside the PBMR core can change dramatically within an hour, it is clear that this JNT configuration will not be a viable measurement solution and methods to reduce the integration times are necessary.

Radiation, on the other hand, has the effect of continually changing the transfer function of the transmission line. This effect is as a result of the radiation damaging and changing the molecular structure of the cable connections. Even if the connecting cables were short enough to allow a sufficiently large bandwidth to minimize integration times, one would still need to continually measure the cables' impedance and adjust the algorithm. Changes in the resistance of the sensor are also inevitable and occur through the same

mechanism as the changes in the cable connections. The noise amplitude will vary at the same temperature as a result of the changing resistance which requires the resistance to be continually measured and the necessary adjustments made. The need to measure the input impedance (which includes the sensor resistance) while at the same time measuring the Johnson noise voltage is one of the reasons why most modern JNT systems have a digital switch before the front-end electronics to allow the switching between the first stage amplifiers and the input impedance measuring circuitry.

Various methods exist to improve the accuracy and integration times of the JNT systems. One of the most successful and widely used techniques to improve the accuracy of JNT systems is the switched-input digital correlator developed by Brixy et al. [11]. The correlator switches between two channels where one is connected to a known resistance R_0 at a known temperature T_0 and the other to a known resistance R at an unknown temperature T . Once the noise signals from these two sources have been digitized, the correlation algorithm is performed during which the amplifier gain fluctuations and noise as well as the transmission line noise are eliminated. Since the RMS Johnson noise of the resistor is known, fluctuations in the amplifier gain and bandwidth can easily be corrected by mathematically determining the RMS noise and measuring the frequency spectra over the reference resistor and then correcting the Johnson noise received from the sensing resistor accordingly. The unknown temperature T is then calculated using Equation 2.3.4.

$$T = \frac{V_T^2 R(T_0)}{V_0^2 R(T)} T_0 \quad (2.3.4)$$

Much progress has been made in developing quantized voltage sources suitable for calibrating JNT systems [3]. Such a source would then replace the reference resistor as a more accurate Johnson noise reference.

A JNT system which has shown great potential is under development by the Oak Ridge National Laboratory (ORNL). The main feature of their system is the cross-power spectral density employed to remove uncorrelated amplifier noise. Two high-gain front-end amplifiers are connected to the sensing resistance and the noise from these two channels is then correlated to remove the uncorrelated amplifier noise but to retain the Johnson noise signal. A third channel can then be switched to and the DC resistance of the sensing

resistor measured. Figure 2.4 illustrates the general system where the Power Spectral Density (PSD) 3 is the Johnson noise contained in PSD 1 and PSD 2.

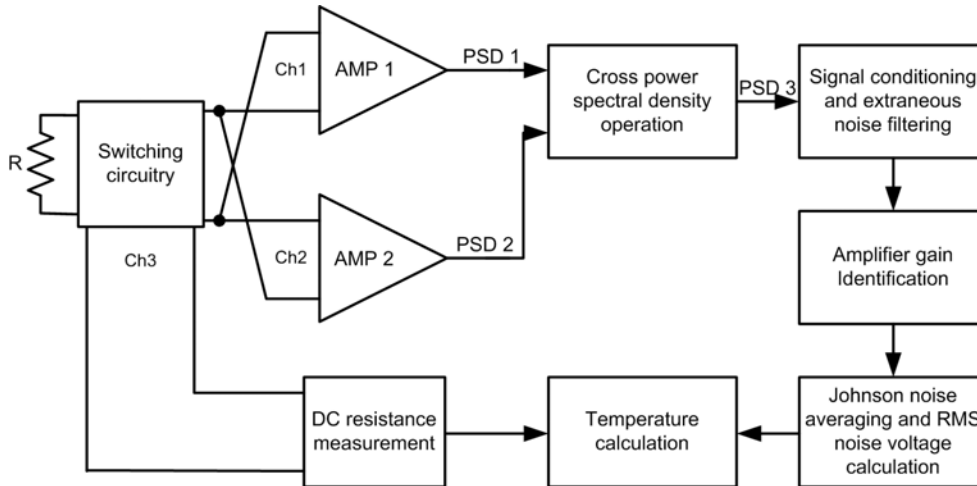


Figure 2.4: A modern JNT setup similar to the system developed by the ORNL.

The attenuation caused by long runs of cable connections can be compensated for up to a point by adding a constant amplitude swept frequency signal to the transmission line and measuring the attenuation over the measured bandwidth [30].

The latest Johnson noise measurement topologies discussed do show significant improvements over their earlier counterparts concerning extraneous noise cancellation, measurement speed and accuracy. Unfortunately the basic bandwidth limitation imposed by the lengthy cable connection between the sensing resistance and the front-end electronics is not yet solved and measurement accuracy and speed remains a serious problem with this type of temperature measurement technology. Radiation-hardened front-end amplifier electronics would seem like the only solution to the problem but this approach poses the difficult problem of developing high-gain low-noise amplifiers that are able to withstand the extreme radiation levels inside the nuclear core.

Distributed sensing along the PBMR core using JNT introduces the situation where an immense amount of front-end amplifiers and wiring is required down the graphite shaft. A setup similar to that of Figure 2.2 would be required together with the front-end amplifiers (if possible) close to the

sensors. This is not an ideal solution given the confined space in which the sensors need to be inserted.

JNT is not suitable for temperature measurement inside the PBMR core given the current status of this technology. It seems highly unlikely, to the best knowledge of the author, that this type of temperature measurement technology will advance to such a level that it will be able to perform the required temperature measurements for the PBMR in the near future.

2.4 Optical Fibre Temperature Sensors

The nuclear industry has over the past few years shown an increasing interest in fibre-optic sensors due their unique sensing abilities and radiation resistance. A short introduction and discussion of the fibre-optic temperature sensors that could possibly be implemented is provided in the following paragraphs.

Optical fibre temperature sensors operate on the principle of guiding light through a thin strand of silica and modulating the reflected or transmitted light in the fibre. All optical fibre sensors are comprised of a transmitter, fibre guide and a receiver as illustrated in Figure 2.5.

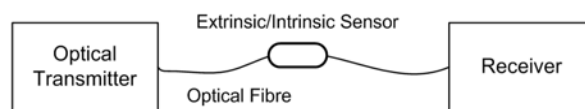


Figure 2.5: General block diagram illustrating the core elements of a fibre-optic sensor.

Optical transmitters can include lasers, Light Emitting Diodes (LEDs) or other light sources depending on the required light frequency, bandwidth and power. In general, LEDs are used when a low-power wide-bandwidth source is required and lasers for high-power narrow-bandwidth applications. Some laser sources' centre frequency can be varied over a specified bandwidth which adds to their versatility. On the other end of the fibre, a receiver detects the light signals that have been modified by the sensor in whatever way and include photodetectors, pin photodiodes, Avalanche Photodiodes (APDs) or even an optical spectrometer, depending on the nature of the application.

The light-carrying medium or optical fibre consists of an optically transparent silica/sapphire core (that may contain various dopants) and surrounding cladding with a higher refractive index in order to support total internal reflection. Sensor information can be imprinted on the transmitted or reflected light inside the fibre through one of many methods that include light intensity, phase, polarization or frequency modulation. Sensors may be intrinsic, where the light never leaves the fibre and is altered in some way by an external phenomenon, or extrinsic when the fibre merely acts as a light delivery and collection system.

Some of the main advantages of fibre-optic temperature sensors in the PBMR are as follows:

1. Fibre-optic temperature sensors are immune to EMI since they are non-conductive. An optical fibre does not absorb significant amounts of electromagnetic radiation and does not become heated by strong electromagnetic fields [5].
2. Optical fibres can operate over a wide range of temperatures (up to 2000°C if sapphire optical fibres are used) and present excellent mechanical and chemical properties.
3. Optical fibres are near-invisible in certain light frequencies and therefore present very little attenuation which makes them ideal for remote measurements. Some temperature sensors can be placed up to 1500 m from radiation-sensitive optoelectronic devices.
4. Distributed temperature sensing can be done with a single fibre. Temperature information can then easily be extracted through interferometric or wavelength separation techniques.
5. The small size and weight of optical fibres also make them ideal sensors for the confined space allocated in the PBMR for temperature measurement.

Radiation effects on fibre optics and the sensor in question's ability to perform accurate temperature measurements for long periods of time in a radiation environment will be taken into account when evaluating the sensors. When referring to the effects of radiation on fibre optics, the reader is referred to Chapter 3 where this aspect is covered in detail.

New developments are made continuously in the field of fibre-optic temperature sensors' and as such many of these methods are still in the development stages where not much is known about their long-term stability and radiation tolerance. Existing optical fibre temperature sensors will be discussed in the following paragraphs together with what is known and not known regarding the sensors' ability to perform long-term accurate temperature measurements in harsh nuclear environments. This list of temperature sensors is by no means complete but represents the most promising technologies for the application.

2.4.1 Rayleigh, Brillouin and Raman Scattering Based Sensors

Rayleigh, Brillouin and Raman scattering are naturally occurring phenomena in fibre optics when certain conditions are met. When light is launched into an optical fibre, changes in density and composition as well as molecular and bulk vibrations cause a portion of the light to be backscattered to the source. The backscattered light consists of a Rayleigh, Brillouin and Raman component [58]. In telecommunications these are undesired effects that interfere with the normal transmission of data but they have been shown to be useful in distributed temperature sensing.

With Rayleigh, Brillouin and Raman scattering based temperature sensing techniques, the fibre itself is the sensor (i.e. an intrinsic sensor) and no further treatment and/or machining is required. These effects, together with their suitability for temperature measurement in the PBMR, will be discussed in the following paragraphs.

In normal fibre-optic operation, the two main loss mechanisms are material absorption and Rayleigh scattering [55]. Rayleigh scattering arises because of microscopic fluctuations in the density of the light-bearing medium (silica/sapphire). These density changes result in changes in the index profile along the fibre length. Each fibre has its own 'fingerprint' due to its random and unique index change along the fibre which in turn can be modelled as a weak FBG with a random period. Ambient temperature changes will result in a change of the Rayleigh scatter and therefore the reflected spectrum. Swept Wavelength Interferometry (SWI) can be used to measure the Rayleigh backscatter as a function of length in an optical fibre with high spatial resolution [21]. According to Giffard et al. [21], they have achieved an SWI-based system that relies on Rayleigh scattering to make distributed temperature

measurements over a normal 20 m strand of silica with a resolution of 5 mm and an accuracy of $\pm 0.3\%$.

The performance of a Rayleigh scattering temperature measurement system in ionizing radiation is not well documented. It is well known that optical fibres need to be radiation-hardened and other special precautions taken (as discussed in Chapter 3) in order to suppress the effects of radiation-induced attenuation, luminescence and refractive index changes. Rayleigh scattering temperature measurement relies on the temperature changes to the weak random refractive index of the fibre which is one of the parameters that radiation will influence according to Primak [53], Taylor et al. [64] and Fernandez [17]. Information concerning the high-temperature measurement performance as well as the radiation effects on the sensor at these elevated temperatures is not well (if at all) documented in the literature. Further research and experimentation is required in this field and it is uncertain whether this temperature-sensing method will be a viable solution.

Brillouin scattering or Stimulated Brillouin Scattering (SBS) occurs as a result of the nonlinearity of the silica/sapphire light-bearing medium. As light propagates in an optical medium, the incident photons interact with acoustic phonons and an upshifted photon (anti-Stokes) and a downshifted (Stokes) photon is produced. The result is that light is reflected back towards the source at a different frequency. This frequency shift is provided by Equation 2.4.1.

$$v_B = \frac{2n_{co}v_A}{\lambda_L} \quad (2.4.1)$$

where v_B is the Brillouin shift, n_{co} is the refractive index of the core, v_A is the acoustic velocity and λ_L is the free-space wavelength of the forward propagating light [51]. The acoustic velocity is dependent upon both strain ϵ and temperature T and since the Brillouin frequency shift is inversely proportional to the acoustic velocity according to Equation 2.4.1, it shares the same dependence on these parameters. The coefficients that relate the temperature and strain to the Brillouin frequency shift can be determined through experimentation where one of the parameters is kept constant and the others' influence on the Brillouin frequency shift is measured and vice versa. Equation 2.4.2 is then solved to determine the temperature.

$$\Delta\nu_B = C_{\text{strain}}\Delta\epsilon + C_{\text{temp}}\Delta T \quad (2.4.2)$$

If Equation 2.4.2 is to be solved by measuring the Brillouin frequency shift alone, the strain on the optical fibre must be known and stay constant. In the harsh environment of a nuclear core the strain on the optical fibre will not be known to such an accuracy required to perform accurate temperature measurements. Parker et al. [51] proposed a method where the temperature and strain can be uniquely determined by measuring the Brillouin power and frequency shift. It is expected that the temperature will be proportional to the Brillouin power and have a small negative dependence on the strain. The Equation in 2.4.2, together with the Brillouin power dependence on temperature, are then solved simultaneously to determine the temperature and strain.

Radiation-induced attenuation due the generation of colour centres in optical fibres varies dramatically among different types of optical fibres, wavelengths and radiation dose rates (please refer to Chapter 3 for a detailed discussion) which renders sensors based on light intensity measurements useless. Another effect discussed in Chapter 3 is that of Radioluminescence (RL). The main contributor to RL in optical fibres originates from Cherenkov emission induced by the gamma radiation in the nuclear core which will, together with radiation-induced attenuation, corrupt light intensity measurements. When taking the above-mentioned facts into account, it becomes clear that the Brillouin power cannot be measured accurately, which renders this method of temperature sensing inadequate for the PBMR.

Brillouin scattering is associated with the nonlinear effects of photons colliding with acoustical phonons, whereas Raman scattering is associated with the event where optical photons collide with optical phonons. In telecommunications Raman scattering is observed when two laser beams with somewhat different wavelengths propagate in the same fibre and the longer-wavelength beam experiences amplification at the cost of the lower-wavelength beam. Spontaneous Raman scattering can also occur as a result of quantum noise effects [1].

With Raman backscatter the anti-Stokes component is strongly dependent upon temperature whereas the Stokes component is weakly dependent on temperature. Molecular vibrations within the sapphire/silica core in-

crease with temperature and cause the Raman backscatter to change as well, hence the temperature sensitivity. A ratio between the Stokes and anti-Stokes provides an absolute value of the temperature irrespective of the fibre laser power and other attenuation effects if these effects are broadband effects (in other words, affect the Stokes and anti-Stokes signals equally). Considering the Raman backscatter's stokes and anti-Stokes ratio as well as the time of flight of the light provides distributed temperature measurements to be made along the fibre with sub-metre accuracy [58]. The ultimate theoretical resolution for this technology is 200 mm for a 2 ns pulse. As with Brillouin scattering, RL will corrupt the reflected data. These facts unfortunately eliminates Raman-based sensor technology if evaluated by the performance parameters of this project since a minimum resolution of 30 mm is required in order to comment on the feasibility of distinguishing between consecutive fuel spheres.

2.4.2 Fluorescence Temperature Sensors

Fluorescence-based optical fibre temperature sensors are probably some of the most commonly used fibre-optic temperature sensors available. Their relative ease of operation and low cost compared to other fibre-optic sensor make them a popular choice.

When a fluorescent material like phosphorous is excited by an incident light pulse, an exponentially decaying signal is emitted by the material. The decay time constant k is highly dependent upon the ambient temperature and can thus be measured in order to determine the temperature. Figure 2.6 provides a graphical representation of the exponential decay signal as well as the excitation pulse. This phenomenon is the working principle of fluorescence temperature sensors.

A typical fluorescence decay temperature sensor would consist of a phosphorous-like material attached to the tip of the fibre and a 50:50 coupler attached to the other end. The induced light emission from the phosphorous tip is then relayed back by the 50:50 coupler to an APD used to detect the light intensity. The decay signal can be modelled by an exponential function as illustrated in Equation 2.4.3.

$$I = I_0 e^{-(t-t_1)/k} \quad (2.4.3)$$

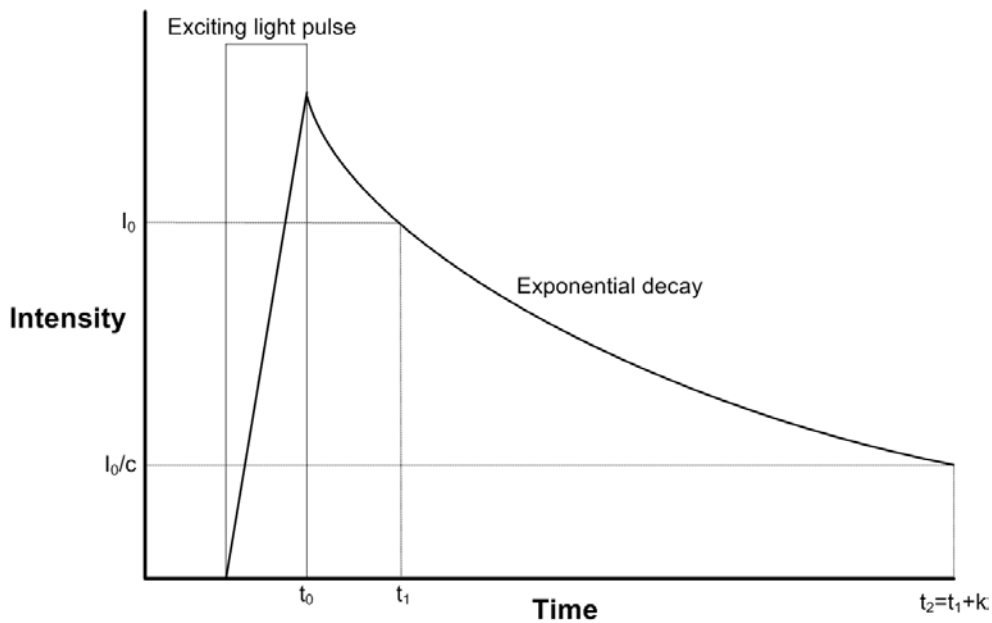


Figure 2.6: An illustration of a fluorescence decay signal.

Fluorescence decay temperature sensing is not suited for temperature measurement inside the nuclear core of the PBMR for several reasons, as discussed in the following list:

- Current commercial fluorescence decay sensors can only operate at temperatures between -200°C to 300°C . The fluorescence intensity at higher temperatures is weak due to the quenching effect [59].
- These sensors have been shown to fail when exposed to even low doses of gamma radiation [5]. This is due to Radiation Induced Attenuation (RIA) in the optical fibre which affects the light intensity observed by the receiver.
- Neutron radiation negatively affects the operation of fluorescence sensors resulting in erroneous temperature readings [45].
- RL (Cherenkov emission induced by gamma radiation) will influence the amplitude of the decay signal perceived by the receiver and lead to erroneous temperature readings.
- Distributed temperature sensing is complicated using this method since only point measurements can be made (if time division multiplexing is

not considered) and in order to measure the temperature along the entire core, several hundred fibre strands will be required. A 25 m core would require 830 strands if the minimum resolution of 30 mm is used.

One fibre can be used to facilitate a few sensors if the fluorescent material is side-etched on the fibre on several locations. The number of sensors that can be multiplexed in this way depends on the source power and absorption characteristics of the fluorescent material. Demultiplexing the received signal requires far more complicated time division demultiplexing equipment.

Fluorescence decay temperature sensing is not suited for the PBMR and will therefore not be further investigated due to the reasons stated.

2.4.3 Fabry-Perot Temperature Sensors

Fibre-optic interferometers can be divided into two main groups: (1) Mach-Zehnder and (2) Fabry-Perot interferometers. Fabry-Perot interferometers are suited for measuring temperature as well as strain, depending on the physical construction of the sensor.

The working principle of Fabry-Perot interferometers is as follows: As light propagates along the fibre core, an abrupt change in fibre density or a reflective surface reflects a portion of the incident light back along the fibre where a photo diode converts the light intensity to a measurable electrical signal. A change in temperature/strain, depending on the sensor type, will influence the path length of the light before it reaches the reflective surface or changes in density. This change in path length of the light causes the incident and reflected light to interfere, thus modulating the reflected light intensity as the path length changes. The light intensity is modulated as follows:

$$I = I_0 \left[1 + \cos \left(\frac{4\pi}{\lambda} x_0 + \varphi_0 \right) \right] \quad (2.4.4)$$

The variable I denotes the light intensity, I_0 is the intensity of the laser source, λ is the centre wavelength of the laser source, x_0 is the path length at some reference temperature and φ_0 is the phase of the laser light source.

A myriad of ways exists to create Fabry-Perot interferometers. Some of the most common ways are fusing fibres with different cores together or attaching reflective surfaces to the tips of fibres that are either temperature-

or strain-sensitive. Due to the variety of sensors available, the measurable temperature ranges as well as accuracies vary dramatically.

Typical Fabry-Perot temperature sensors are constructed from Pyrex reflective surfaces, have accuracies of $\pm 2^\circ\text{C}$, and operate at temperatures between -270°C and 300°C . This type of Fabry-Perot sensor is known to degrade monotonously with gamma and neutron radiation [5]. This type of sensor is therefore not suitable for use in the PBMR due to its radiation sensitivity as well as the limited temperature range.

Radiation-resistant Fabry-Perot sensors have been developed that uses unique signal processing techniques. The sensor signal conditioner employs a Fizeau interferometer and a charge-coupled device array to locate the position of the maximum interference fringe intensity rather than the absolute light intensity [42]. The basic sensing mechanism is therefore independent of the light intensity which is most likely to be affected by the radiation. Fabry-Perot sensors have unfortunately not been proven to operate at high temperatures.

Another radiation-resistant sensor in this technology class is the Fibre Fabry-Perot Interference (FFPI) sensor. The performance of an FFPI sensor has been tested in the presence of radiation levels up to 1 MGy by Lai C.C. et al. [40]. The experiments have shown that the thermo-optic coefficient increases by only 2.1% and saturates at a total dose of 300 kGy. This sensor proves to be radiation-resistant but was unfortunately only tested between temperatures of 0°C and 150°C . Operation at elevated temperatures in harsh environments is again unknown.

Fabry-Perot temperature sensors have been proven to operate satisfactorily in low-temperature radiation environments but much research and experimentation is still required in order to determine whether this temperature sensing technology can be used in the harsh radiation and temperature conditions present in the PBMR core.

2.4.4 FBG Temperature Sensors

A Fibre-Bragg Grating (FBG) is a periodic or aperiodic perturbation in the effective refractive index of an optical fibre core. The FBG is most commonly achieved by 'inscribing' or 'writing' a variation in the refractive index of a silica optical fibre core using an Ultraviolet (UV) laser source. This UV laser

source is then used to write the FBG using either one of two methods: Interference or masking.

The operation of an FBG is very much the same as a notch filter with the difference being that the filtered light frequency is reflected back towards the source instead of being attenuated as in electrical filters. FBGs are therefore used as filters, add/drop elements and dispersion compensators in the optical telecommunications industry. Figure 2.7 graphically illustrates the operation of FBGs.

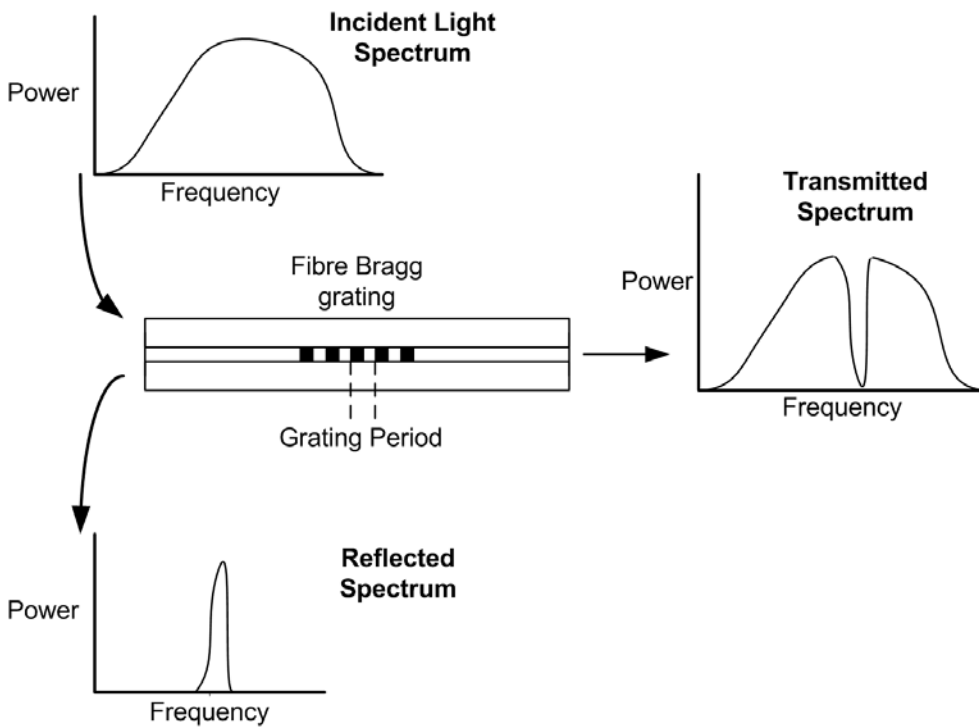


Figure 2.7: The general operation of an FBG.

The centre frequency of the FBG or Bragg wavelength (λ_B) is dependent on the period of the grating Λ and the effective refractive index n_{eff} of the core. A change in temperature causes a change in the refractive index as well as the period of the grating which in turn changes the Bragg wavelength of the FBG. Equation 2.4.5 provides the relationship between the effective index and the period of the grating [55].

$$\lambda_B = 2n_{\text{eff}}\Lambda \quad (2.4.5)$$

Various deviations from the basic FBG described exist and the six most common types are [15]: (1) uniform positive-only index change, (2) Gaussian apodized, (3) raised-cosine apodized, (4) chirped, (5) discrete phase shifted and (6) superstructures. All of these different methods change and modify the wavelength response of the FBG. FBGs are normally apodized in order to mitigate the side lobes resulting from the abrupt beginning and ending of the grating. The physical length of an FBG must be a few millimetres in order to achieve a bandwidth of less than one nanometre and near-total reflection within this bandwidth.

It is widely known in the literature that intensity measurements must be avoided in order to achieve accurate and dependable temperature measurements with fibre optics in the presence of radiation. This is due to the wavelength-dependent attenuation increase (colour centres) resulting from ionizing radiation [23]. The amount of attenuation at each frequency cannot be accurately determined and depends on many factors including the molecular structure and amount of defects within the fibre. FBGs are therefore ideally suited for the conditions present in the PBMR since the temperature information is contained within a very narrow spectral bandwidth where the light intensity does not influence the temperature reading.

The radiation sensitivity of FBGs in silica at low temperatures (below 400°C) has been extensively analyzed and it was experimentally found that radiation can induce a change in λ_B of up to 0.1 nm or 10°C [66] [46] [16]. When using the proper manufacturing technique, and stabilizing the fibres using pre-irradiation techniques; FBG can become less affected by the harsh radiation environment of a nuclear core [17].

Silica optical fibres with FBGs cannot be used at elevated temperatures above 400°C. At temperatures above 400°C the grating diffuses in the fibre, resulting in the erasure of the FBG. It is therefore necessary to use sapphire FBGs which have been proven to operate at temperatures exceeding 1500°C with no observed degradation of the grating strength [24]. It was also noted by Grobncic et al. [24] that FBGs written into sapphire optical fibres using femto-second laser radiation could potentially operate up to 2000°C.

FBGs possess very desirable attributes for use in the PBMR. The ability to multiplex several gratings into one fibre and the ease with which the spectral information can be demultiplexed to attain the temperature at each grating is a tremendous advantage over other temperature measurement techniques.

An elementary setup in Figure 2.8 illustrates the basic concept of how such a sensor system would be implemented in the PBMR. The circulator acts as a router for the optical light; more detail on the operation thereof is provided in Chapter 5. It might be necessary to switch between different fibres running down the core if a fine sampling interval is required. This is due to the limited bandwidth available to operate the FBG when taking into account the spectral shifts that the gratings experience with changing temperature conditions.

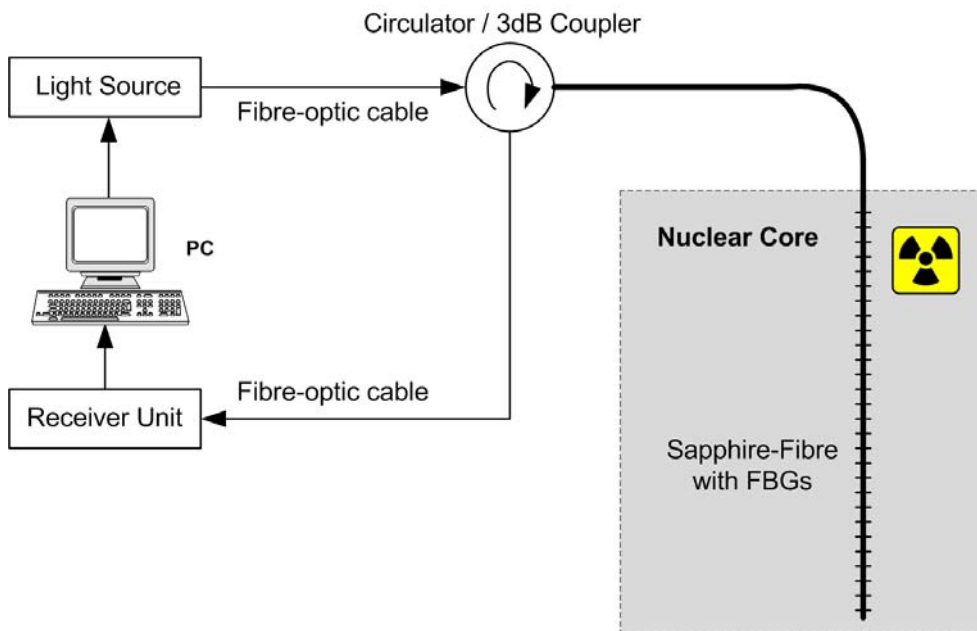


Figure 2.8: FBG distributed temperature sensing. Note that the dashed lines on the fibre illustrates individual FBGs.

Sapphire fibre is known for its excellent temperature characteristics as well as being fairly resistant to radiation. Not nearly enough research have been done to investigate the combined effect that radiation and elevated temperatures will have on the spectral response of FBGs. The prospect of this technology operating satisfactorily in these conditions shows far more potential than any of the other sensor types. A far more detailed discussion regarding this technology is provided in Chapter 4.

2.5 Conclusion

The major temperature-sensing mechanisms have been discussed and evaluated according to the criteria set forth in Section 1.2. Table 2.2 serves as a summary of the research as well as a comparison of the sensing mechanisms in order to make a decision as to which sensor is fit for temperature measurement inside the PBMR. Please note that the survivability of the sensors have not been taken into account as none of these sensors have been adequately evaluated in such a manner that commenting on lifespan in a nuclear core is justifiable.

The International Thermonuclear Experimental Reactor or ITER sparked a worldwide interest in the development and research of FBG-based temperature sensing inside a nuclear core. Many of the developments and radiation-hardening techniques have been researched as a result of the ITER. Many of the challenges faced in the ITER will also be faced in the PBMR. Specialists in the field of FBGs such as Alberto Fernandez Fernandez and Francis Berghmans have all shown discriminating interest into FBGs for in-core distributed temperature measurement.

From Table 2.2 it is clear that FBGs illustrate the most potential in performing adequate temperature measurements inside the PBMR core. Although little is known regarding the high-temperature radiation resilience of FBGs, the low-temperature performance is promising. FBGs will therefore be the topic of this thesis.

Sensing Mechanism	Temperature Range	Radiation Resilience	Suitability for Distributed Sensing	Resolution Achievable
Thermocouples	Well over 1600C when using the correct materials. Depends on the resistive sensing element.	Requires extensive radiation shielding.	Not particularly suited, will require an immense amount of wiring and space.	More than 30 mm
JNT	Depends on the resistive sensing element.	Requires shielding as well as radiation-resistant electronics.	Not particularly suited, will require an immense amount of wiring and space.	More than 30 mm
Rayleigh scattering	Depends on fibre, potentially up to 2000°C if sapphire is used.	Unknown. Further research is required.	Perfectly suited.	Maximum 200 mm
Fluorescence-type sensors	Range limited from -200°C to 300°C due to the quenching effect.	Not radiation-resistant.	Will require an immense amount of fibres and sensing elements.	More than 30 mm
Fabry Perot sensors	Potentially suited for temperatures over 1600°C.	Unknown at high temperatures.	Will require an immense amount of fibres and sensing elements.	More than 30 mm
FBGs	Proven to be well over 1600°C when using sapphire optical fibre.	Excellent at low temperatures. Potentially satisfactory at higher temperatures with sapphire fibre; further testing is required.	Perfectly suited.	More than 30 mm

Table 2.2: Selecting the correct temperature sensing technology for the PBMR.

Chapter 3

Optical Fibres

The literature study will focus on FBGs since this sensor type demonstrates the most potential in overcoming all of the stated difficulties. Since an FBG is an all-optical device, it was deemed necessary to identify all the possible effects in optical fibres that might influence the performance of such a sensor. A discussion of optical fibres is therefore presented in this Chapter. Sapphire fibre will ultimately be used as the preferred light transmission medium but silica fibre is discussed as many effects are synonymous.

3.1 Light Propagation in an Optical Fibre

An optical fibre consists of three main parts that include the core, cladding and the coating or jacket. Light propagation mainly takes place in the innermost part of the optical fibre, namely the core, whose main constituent is silica or sapphire. The cladding is a thin dielectric layer with a lower refractive index in order to confine the light inside the fibre and limit attenuation. Finally the coating or jacket serves to protect the optical fibre mechanically and chemically. Figure 3.1 illustrates the geometric structure of an optical fibre.

One can obtain a simplified understanding of light propagation in an optical fibre using ray theory or geometrical optics. Geometrical optics is only valid for multimode fibres whereas ray theory is more commonly used to describe light propagation in single-mode fibres. An optical fibre is defined as a multimode fibre when the core radius a is far larger than the operating wavelength, thus supporting multiple modes of light propagation.

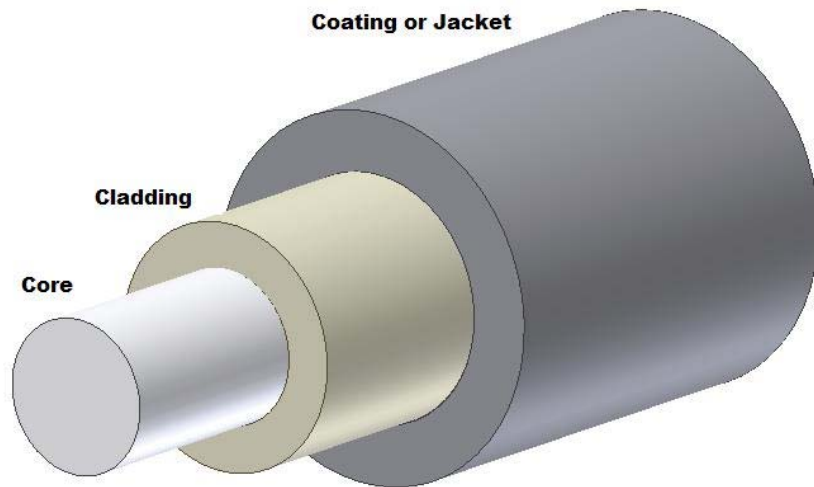


Figure 3.1: Geometrical structure of a step index optical fibre.

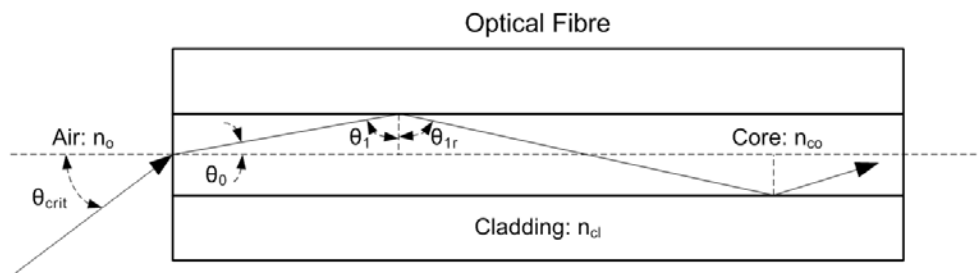


Figure 3.2: Light propagation in a multimode fibre.

When light propagates from one homogeneous isotropic material to another, the light will be bent at the interface and refraction as well as reflection occurs. A condition for total internal reflection is that the core refractive index must be larger than the cladding's refractive index. Referring to Figure 3.2, the laws of optics state that $\theta_1 = \theta_{1r}$ and according to Snell's law:

$$n_{co} \sin(\theta_1) = n_{cl} \sin(\theta_{1r}) \quad (3.1.1)$$

where n_{cl} and n_{co} is defined as the refractive index of the cladding and core, respectively. From a geometrics viewpoint, light propagates and is contained within an optical fibre through a series of internal reflections that occur at the interface between the core and the cladding.

A critical angle θ_{crit} (also called the acceptance angle) exists where the

light entering the optical fibre is completely reflected and no longer enters the optical fibre. Using Snell's law it can be shown that only light waves incident at an angle smaller than θ_{crit} can enter the fibre and undergo total internal reflection. The critical angle is also a measure of the ability of the fibre to couple light into the fibre and is provided by Equation 3.1.2 where n_0 is defined as the refractive index of air.

$$\theta_{\text{crit}} = \sin^{-1} \left(\frac{\sqrt{n_{\text{co}}^2 - n_{\text{cl}}^2}}{n_0} \right) \quad (3.1.2)$$

Optical fibres have different core diameters and refractive index profiles to achieve certain desired characteristics. In order to reduce the effects of intermodal dispersion or multipath (which will be discussed later) various techniques have been developed, such as graded index fibres and optical fibres with cores in the micrometre range called single-mode fibres. In single-mode fibres only a single mode is allowed to propagate which is also called the fundamental mode, while in multimode optical fibres up to millions of modes can travel along the fibre.

A single-mode fibre is generally referred to as a fibre with a core diameter less than 10 times the wavelength of the propagating light in it. These fibres cannot be modelled using geometrics and are analyzed as an electromagnetic structure using Maxwell's equations. Maxwell's equations in a lossless homogeneous medium are expressed by the following equations in terms of the electric and magnetic field [50]:

$$\Delta \times \mathbf{e} = -\mu \frac{\partial \mathbf{h}}{\partial t} \quad (3.1.3)$$

$$\Delta \times \mathbf{h} = -\epsilon \frac{\partial \mathbf{e}}{\partial t} \quad (3.1.4)$$

In Equations 3.1.3 and 3.1.4 the electric and magnetic fields in phasor form are represented by \mathbf{e} and \mathbf{h} , respectively. The coefficient ϵ denotes the permittivity of the medium and is related to its value in a vacuum $\epsilon_0 = 8.854 \times 10^{-12}$ F/m by Equation 3.1.5 where n_{co} is the refractive index of the fibre core.

$$\epsilon = \epsilon_0 n_{\text{co}}^2 \quad (3.1.5)$$

The permeability of the medium, on the other hand, is represented by μ and is equal to its value in a vacuum $\mu = \mu_0 = 4 \times 10^{-7}$ H/m. Within the fibre core we have the propagation constants κ and β in the lateral and forward direction, respectively, as illustrated in Figure 3.3.

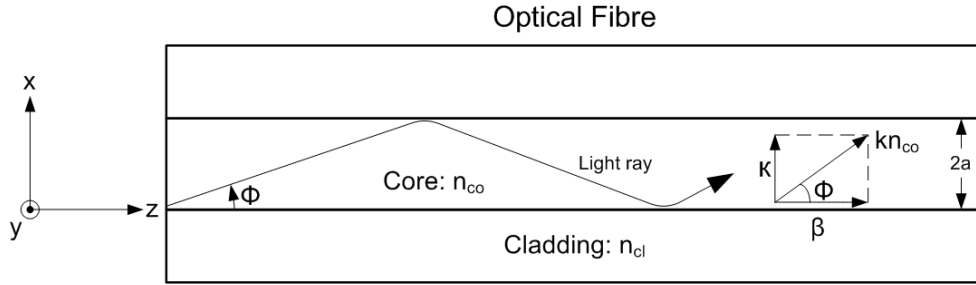


Figure 3.3: Wave propagation in an optical fibre illustrating the magnetic field constituents.

The wavenumber is then defined as the propagation constant in the direction of the travelling light ray and is mathematically expressed as in Equation 3.1.6.

$$\Gamma = \omega \sqrt{\epsilon \mu} = \omega n_{\text{co}} \sqrt{\epsilon_0 \mu_0} = \kappa n_{\text{co}} = \frac{\omega n_{\text{co}}}{c} \quad (3.1.6)$$

In Equation 3.1.6, the speed of light, c , is defined at 2.998×10^8 m/s and the symbol k as the wavenumber in a vacuum. The angular frequency of the light ray ω is related to the wavelength through Equation 3.1.7 where the relationship $\omega = 2\pi f$ is made use of.

$$\lambda = \frac{c}{f} = \frac{\omega}{kf} = \frac{2\pi}{f} \quad (3.1.7)$$

In order to express the electric and magnetic waves propagating within the optical fibre, one has to make use of phasors (in bold) since these electromagnetic waves are sinusoidal functions of time with an angular frequency of ω . The electric and magnetic waves that travel in the z direction (please refer to Figure 3.3) with a propagating constant β are mathematically expressed by Equations 3.1.8 and 3.1.9, respectively.

$$\mathbf{e} = \mathbf{E}(\mathbf{r})e^{j(\omega t - \beta z)} \quad (3.1.8)$$

$$\mathbf{h} = \mathbf{H}(\mathbf{r})e^{j(\omega t - \beta z)} \quad (3.1.9)$$

The forward propagation constant β is computed using the following trigonometric relation (refer to Figure 3.3):

$$\beta = kn_{\text{co}} \cos \phi \quad (3.1.10)$$

When substituting Equations 3.1.8 and 3.1.9 into Equations 3.1.3 and 3.1.4, the following set of equations determining the electromagnetic fields within the optical fibre are obtained [50]:

$$\frac{\partial E_z}{\partial y} + j\beta E_y = -j\omega\mu_0 H_x \quad (3.1.11)$$

$$-j\beta E_x - \frac{\partial E_z}{\partial x} = -j\omega\mu_0 H_y \quad (3.1.12)$$

$$\frac{\partial E_y}{\partial x} - \frac{\partial E_x}{\partial y} = -j\omega\mu_0 H_z \quad (3.1.13)$$

$$\frac{\partial H_z}{\partial y} + j\beta H_y = j\omega\epsilon_0 n_{\text{co}}^2 E_x \quad (3.1.14)$$

$$-j\beta H_x - \frac{\partial H_z}{\partial x} = j\omega\epsilon_0 n_{\text{co}}^2 E_y \quad (3.1.15)$$

$$\frac{\partial H_y}{\partial x} - \frac{\partial H_x}{\partial y} = j\omega\epsilon_0 n_{\text{co}}^2 E_z \quad (3.1.16)$$

Equations 3.1.11 to 3.1.16 describe the electromagnetic waves in Cartesian coordinates. Optical fibres are axially symmetric and are therefore better described when written in terms of cylindrical coordinates:

$$\frac{1}{r} \frac{\partial E_z}{\partial \theta} + j\beta E_\theta = -j\omega\mu_0 H_r \quad (3.1.17)$$

$$-j\beta E_r - \frac{\partial E_z}{\partial r} = -j\omega\mu_0 H_\theta \quad (3.1.18)$$

$$\frac{1}{r} \frac{\partial}{\partial r}(rE_\theta) - \frac{1}{r} \frac{\partial E_r}{\partial \theta} = -j\omega\mu_0 H_z \quad (3.1.19)$$

$$\frac{1}{r} \frac{\partial H_z}{\partial \theta} + j\beta H_\theta = j\omega\epsilon_0 n_{co}^2 E_r \quad (3.1.20)$$

$$-j\beta H_r - \frac{\partial H_z}{\partial r} = j\omega\epsilon_0 n_{co}^2 E_\theta \quad (3.1.21)$$

$$\frac{1}{r} \frac{\partial}{\partial r}(rH_\theta) - \frac{1}{r} \frac{\partial H_r}{\partial \theta} = j\omega\epsilon_0 n_{co}^2 E_z \quad (3.1.22)$$

Maxwell's equations do not define the electromagnetic field entirely and out of the infinite possible solutions to these equations, those that satisfy the boundary conditions must be calculated. Boundary conditions occur where there are variations in the refractive index of the fibre core as in, for example, an FBG. The tangential components of both the magnetic and electric fields must be equal at the boundary where the change in medium is present.

All of the equations discussed thus far (Equations 3.1.11 to 3.1.22) are applicable to birefringent, graded index, step index and other available optical fibre configurations. The operation of FBGs written in silica optical fibres are governed by the Equations 3.1.11 to 3.1.22.

Sapphire optical fibre, on the other hand, is a multimode step index fibre which allows for some further simplification of the electromagnetic field equations. If we consider that the sapphire fibre is axially symmetric the electromagnetic field relations become independent from θ and can be replaced by $n(r)$. The transverse electromagnetic waves then become:

$$E_r = \frac{-j}{k^2 [n(r)]^2 - \beta^2} \left(\beta \frac{\partial E_z}{\partial r} + \frac{\omega\mu_0}{r} \frac{\partial H_z}{\partial \theta} \right) \quad (3.1.23)$$

$$E_\theta = \frac{-j}{k^2 [n(r)]^2 - \beta^2} \left(\beta \frac{\partial E_z}{\partial \theta} - \omega\mu_0 \frac{\partial H_z}{\partial r} \right) \quad (3.1.24)$$

$$H_r = \frac{-j}{k^2 [n(r)]^2 - \beta^2} \left(\beta \frac{\partial E_z}{\partial r} - \frac{\omega\epsilon_0 [n(r)]^2}{r} \frac{\partial E_z}{\partial \theta} \right) \quad (3.1.25)$$

$$H_\theta = \frac{-j}{k^2 [n(r)]^2 - \beta^2} \left(\beta \frac{\partial H_z}{\partial \theta} + \omega\epsilon_0 [n(r)]^2 \frac{\partial H_z}{\partial r} \right) \quad (3.1.26)$$

The Transverse Electric (TE) and Transverse Magnetic (TM) waves are obtained by substituting either $E_z = 0$ for the TE modes or $H_z = 0$ for the TM modes. When analyzing the reflection and transmission spectra of FBGs,

these electromagnetic wave equations are instrumental in the characterization process.

3.2 Intermodal and Chromatic Dispersion

The term dispersion is given to any effect wherein the different components of the transmitted signal travel at different velocities in the fibre, therefore arriving at different times at the receiver. Both intermodal and chromatic dispersion (group velocity dispersion) result in data corruption at the receiver side and pose a threat to the data integrity of fibre sensing systems. The working principles, effects and possible ways of avoiding these phenomena will be discussed in the following paragraphs.

Intermodal dispersion within an optical fibre is concerned with the number of modes that propagates through an optical fibre. A mode can be thought of as a possible path that a light ray might follow through an optical fibre. Some rays might travel in a more-or-less straight line, whereas the majority of light propagating in an optical fibre will undergo numerous reflections. In general these propagating modes are skew rays [35] but in order to simplify the analysis only meridional (non-skewed) rays will be considered when calculating the time spread effect due to intermodal dispersion.

The fastest ray within the fibre will travel along the centre of the core while the slowest ray is incident at the critical angle and undergoes the maximum amount of reflections. The time spread of the injected light power is therefore calculated as follows:

$$\delta T = T_{\text{slowest}} - T_{\text{fastest}} = \frac{Ln_{\text{co}}^2}{cn_{\text{cl}}} - \frac{Ln_{\text{co}}}{c} \quad (3.2.1)$$

In Equation 3.2.1, c is defined as the speed of light in a vacuum. The length of the fibre L is directly proportional to the time of flight of the slowest and fastest mode and therefore the time spread of the pulse. When considering the PBMR, the maximum fibre length that will be encountered is approximately 30 m. The effect of intermodal dispersion is effectively doubled when using FBGs as sensing elements due to the fact that light is reflected from the grating and back to the sensing equipment.

The number of modes M travelling along the core is dependent on the operating wavelength λ , the core refractive index n_{co} , the cladding refractive

index n_{cl} and the core radius as illustrated in Equation 3.2.2.

$$M = \frac{2\pi^2 a^2}{\lambda^2} (n_{co}^2 - n_{cl}^2) \quad (3.2.2)$$

Intermodal dispersion can cause significant time pulse spreading if data is sent over long lengths of fibre. It is therefore advisable to use graded index fibres which will significantly reduce intermodal dispersion or single-mode fibre to completely eliminate intermodal dispersion. Sapphire fibre has the disadvantage of having a larger-diameter core which will naturally allow a myriad of modes to propagate. The time spread of the reflected signals must be considered when a Time Division Multiplexing (TDM) FBG system is used.

Chromatic dispersion, on the other hand, is the term given to the phenomena where different spectral components of a pulse travel at different velocities. Single-mode fibre is usually associated with chromatic dispersion since intermodal dispersion overshadows the effects of chromatic dispersion in multimode fibres.

Chromatic dispersion arises for two reasons as discussed in the following paragraphs:

1. The principle cause of chromatic dispersion is due to the inherent frequency dependence of the refractive index of the silica in an optical fibre. The frequency-dependence of the refractive index of silica influences the propagation constant of the transmitted signal. Unfortunately this property of silica results in different frequency components of the transmitted signal arriving at different times, thereby causing frequency smearing and distortion of the data. This component of chromatic dispersion is termed material dispersion.
2. The second component of chromatic dispersion is called waveguide dispersion. Although most of the power travelling in a fibre is confined to the core, a certain proportion does propagate within the cladding. The power distribution of a mode between the core and cladding is a function of the wavelength of the mode. Longer wavelengths results in a greater portion of the light power propagating in the cladding and vice versa. The effective index of the fibre is therefore frequency-dependent which in turn influences the propagation constant of the different propagating modes.

Figure 3.4 illustrates the practical implications of chromatic dispersion on a rectangular data pulse.

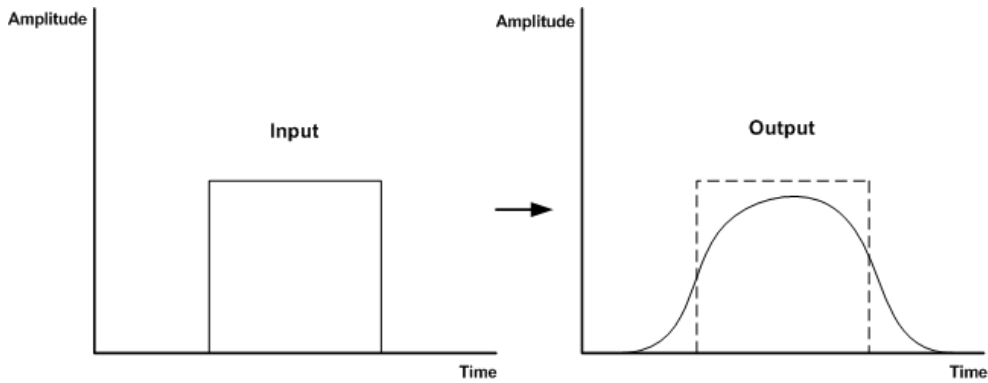


Figure 3.4: The effects of chromatic dispersion on a rectangular pulse travelling in an optical fibre. A rectangular pulse has several high-order frequency components and is therefore exceptionally susceptible to chromatic dispersion.

Fortunately, the use of FBGs allows the grating to be interrogated by a monochromatic light signal which will not be affected by chromatic dispersion. The reflected light from the grating will also possess a narrow spectral width and the effects of chromatic dispersion can therefore be assumed negligible when using FBGs.

Assuming that sapphire fibre will be used in the PBMR core, the biggest concern regarding dispersion will be caused by intermodal dispersion with TDM FBG systems. Fibre lengths should therefore be kept to a minimum and the manufacturing of sapphire fibres with smaller core diameters (in order to limit the amount of propagating modes) should be further researched.

3.3 Mechanisms of Attenuation

In typical optical fibre communication systems a signal can undergo an attenuation of about 20 – 30 dB before amplification or regeneration is required. Standard optical fibre exhibits attenuation losses of 0.25 dB/km, which relates to distances of 80 – 120 km where no amplifiers or regenerators are required [55]. In this Section, attenuation in optical fibres will be discussed in further detail in order to determine the main mechanisms of signal attenua-

tion due to the materials used, radiation and other environmental factors. In each case attenuation, α , is defined as:

$$\alpha = 10 \log_{10} \left(\frac{P_{\text{out}}}{P_{\text{in}}} \right) \quad (3.3.1)$$

The three main loss mechanisms under normal operating conditions in optical fibres are material absorption, scattering and bending losses. This does not include the optical power loss resulting from splicing, connectors and couplers. Material absorption, scattering and bending losses are discussed in further detail in the following Sections.

3.3.1 Material Absorption

Material absorption is defined as the portion of attenuation where the light energy is converted to another form, such as heat. Absorption in optical fibres can be explained by three factors:

1. Imperfections in the atomic structure of the optical fibre induce absorption. Missing molecules or oxygen defects are usually the cause.
2. Intrinsic absorption is the minimum amount of attenuation that light would experience in a perfect fibre and is caused by the basic fibre material (silica/sapphire) itself.
3. Extrinsic absorption, on the other hand, is as a result of impurities introduced into the fibre. Trace metals such as iron, nickel and chromium are often introduced into the fibre during fabrication. Hydroxyl ions OH^- introduced into the fibre forms a silicon-hydroxyl bond SiOH which results in absorption peaks at 1383 nm, 1250 nm and 950 nm.

Optical fibres available today have very low impurity levels and excellent structural integrity (especially silica fibres), the result being extremely low (negligible) absorption from 800 nm to 1600 nm.

3.3.2 Scattering

Another source of attenuation in optical fibres is as a result of light interaction with density fluctuations in the fibre. Density changes in fibres are introduced during the manufacturing process and cause the incident light

to partially scatter in all directions. A portion of the light is reflected back to the source while another portion of the scattered light power is coupled into the cladding and therefore evanescent. In commercial fibres, the main source of signal attenuation is Rayleigh scattering which occurs when the size of the density fluctuation is less than one-tenth of the operating wavelength. Optical power loss due to Rayleigh scattering α_R can be quantified mathematically as [55]:

$$\alpha_R = \frac{A}{\lambda^4} \quad (3.3.2)$$

In Equation 3.3.2, A denotes the Rayleigh scattering coefficient and λ the operating wavelength. Rayleigh scattering rapidly decreases with an increase in wavelength due to the λ^{-4} dependence. Material absorption in silica becomes quite severe at higher frequencies and sets an upper bound on the operating frequency.

If, however, the size of the defect is larger than one-tenth of the operating frequency, the scattering mechanism is called Mie scattering. Incident light is once again scattered out of the fibre core and lost. The occurrence of such large defects in modern fibres is very unlikely and this form of scattering can therefore be ignored.

3.3.3 Bending Loss

Bending loss is another major source of attenuation in optical fibres. Macrobend losses occur when the fibre's bend radius becomes small in relation with the fibre diameter. When a fibre's bend radius becomes a few centimetres, light travelling on the inner bend travels a shorter distance than light on the outer bend. When the bend radius decreases to some critical radius, the mode velocity is forced greater than the speed of light, which is impossible. This condition causes some of the light to propagate in higher modes which are lost or radiated out of the fibre. Handling optical fibres must be done with extreme care to ensure that the maximum bend radius specified by the manufacturer is not exceeded. Not adhering to this requirement will result in severe signal attenuation or even damage to the fibre itself. The fibre's sensitivity to bending loss can be reduced by either increasing the refractive index of the core or increasing the core diameter.

Microbends are small imperfections or discontinuities in the fibre. Im-

proper or uneven coating and cabling of optical fibres result in increased microbend loss. External forces can also damage the fibre jacket and cause small bends in the optical fibre. Microbends distort the propagating paths of the modes and results in an increase in attenuation because low-order modes get coupled into higher-order modes which are naturally lossy.

3.3.4 Radiation-induced Attenuation

Radiation-induced attenuation or RIA can result in significant transmitted power loss in optical fibres exposed to the harsh radiation conditions inside the PBMR. RIA and fibre-optic radiation-hardening techniques are actively being researched by many institutions as a result of the proposed applications of fibre technology in the ITER. As previously mentioned, environmental conditions within the PBMR will include high levels of neutron fluence, gamma radiation and elevated temperatures. The amount of attenuation and the wavelength at which the attenuation is experienced depends mainly on the following seven factors:

1. The chemical composition of the fibre is a major factor influencing the overall attenuation experienced by the fibre as well as the wavelengths experiencing attenuation.
2. Neutron fluence (ionizing radiation) in the core affects the molecular structure of materials and high-energy neutrons are capable of knocking oxygen atoms from the fibre structure [10]. Altering the molecular structure of the fibre inevitably results in frequency-dependent attenuation.
3. Gamma radiation is a major contributor to RIA. Total dose and dose rate are important factors to be considered.
4. Injected light power influences the amount of RIA experienced by the fibre.
5. The amount of RIA experienced is dependent on the geometry of the fibre.
6. Care should be taken in selecting a proper jacket or fibre coating to prevent possible diffusions and effects brought on by the coating's chemical nature.

7. RIA is finally also dependent upon the temperature at which the radiation is administered.

Proper long-term evaluation of RIA in silica, doped silica and sapphire fibres in high radiation (similar to that of the PBMR) at elevated temperatures (1600°C) does not exist to the best knowledge of the author. A great deal of research and testing is therefore needed to determine the survivability of sapphire optical fibre in a radiation environment. However, various research groups have conducted radiation tests on silica as well as sapphire fibres at temperatures below 400°C. In the following paragraphs the author will present a short summary of the most relevant research conducted and state its conclusions. Assumptions will, however, not be made on the RIA at elevated temperatures and this will remain as one of the unknowns in the project.

Irradiated fibres show an increase in attenuation due to the creation of various types of defects, sometimes referred to as 'colour centres'. A thorough review of RIA can be found in Dooryhee et al. [13]. RIA is generally understood as a combination of absorption bands which will be discussed in the following paragraphs.

In fibres with chloride impurities, RIA may be dominated by the absorption tail extending from UV wavelengths up to approximately 1000 nm [22]. In the manufacturing of silica, care should be taken to ensure the purity content thereof since attenuation caused by chloride contamination will render the fibre unusable in harsh radiation environments. The second most dominating cause of RIA is due to the build-up of Non-bridging Oxygen Hole Centres (NBOHC) which leads to an absorption peak in the 600 – 630 nm range. The reaction that occurs during the formation of NBOHC colour centres in silica fibres is as follows [6]:



In Equation 3.3.3, the symbols \equiv and $*$ represent a trivalent bond and an unpaired electron, respectively. Hydrogen loading of fibres is a proven method to passivate the formation of NBOHC centres and irradiated fibres impregnated with H show a decrease in RIA [22]. There is evidence that radiolytic release of H from the plastic jacket layers can also reduce the NBOHC concentration [23]. Hydrogen loading is consequently used to decrease the

attenuation in optical fibres and the possible reaction explaining this observation is explained by Equation 3.3.4 where the right-hand side of the equation is less effective in absorbing incident light [41].



Radiation-hardening often occurs when observing some absorption bands such as the visible region where attenuation slightly decreases with an increase in radiation dose [61]. This phenomenon has been proposed to be as a result of the radiolytic creation of E' centres, $\equiv Si^*$ which can also react with NBOHC states to form peroxy radicals, $\equiv Si - O - O^*$ that are less effective absorption centres [22].

Various other minor defects and methods of attenuation exist that depends on the core dopants and fabrication techniques. The induced loss is often reported to be dose-rate-dependent due to the competing defect creation and deactivation mechanisms. Steady state can be reached when the rate of creation of defects equals the rate of deactivation of defects [22]. Frequency bands that are suitable for operation within radiation environments have to be identified since it is widely known that for, example, the visible frequency spectrum experiences unacceptably high levels of attenuation in radiation environments, rendering this frequency band useless for data transmission. Several off-the-shelf fibres have been tested by many research institutions and their attenuation monitored for certain levels of radiation at set temperatures. Figure 3.5 illustrates the attenuation versus frequency for a dry silica fibre (OH content below 2 ppm) at radiation levels similar to that encountered inside a fission reactor and temperatures between 130 and 290°C.

Note that in Figure 3.5 two fibres are tested, one with a metal coating and the other with a polymer coating. Injected light at frequencies lower than 800 nm will be almost completely attenuated by silica fibre when exposed to ionizing radiation in the MGy levels. Wavelengths between 800 nm and 1600 nm are useful for data transmission; data transmitted at any other wavelength will be completely attenuated within a few metres. Even when operating at 1600 nm an attenuation of 3 dB per metre (for 150 MGy) is unacceptable when considering that light roughly needs to travel a maximum of 60 m within the core (30 m down and 30 m back up again when reflected

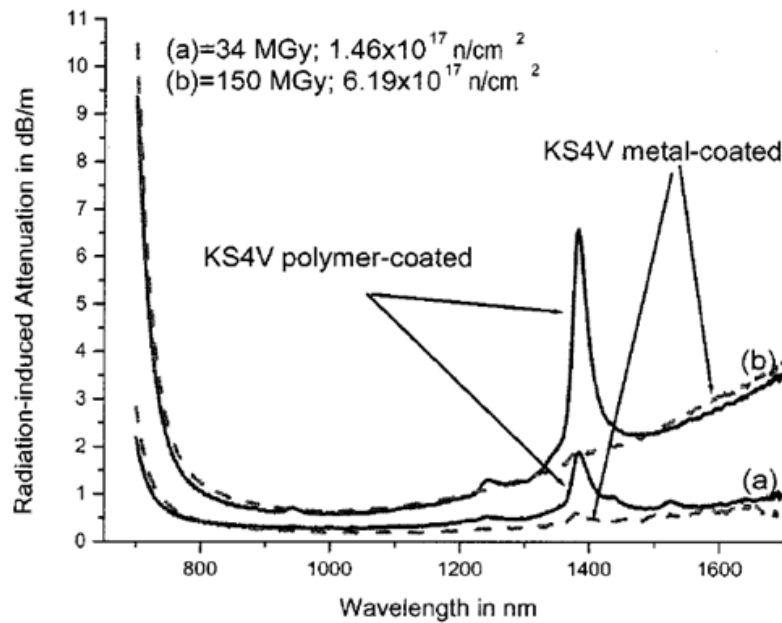


Figure 3.5: Radiation-induced attenuation for dry silica fibres with polymer and metal jackets [10].

from the furthest grating) and will therefore be attenuated by as much as 180 dB. Small signals such as these will not be recognizable by most photonic instrumentation, not even mentioning the added noise levels associated with radiation environments.

Another absorption peak is evident in the 1350 – 1450 nm range due to neutron knock-on that produces recoil protons from the polymer coating and contributes to the increase of OH in the fibre [10]. This absorption band is not present with the metal-coated fibre. Care should therefore be taken in determining a suitable jacket or coating for the optical fibre to prevent unforeseen diffusions and effects.

In general it is also known that an increase in temperature results in a decrease in RIA [20] which can improve the application applicability considering that the PBMR operates at the very high temperature of 900°C. Higher injected light power, on the other hand, will cause photo bleaching, which in turn might also result in reduced RIA, particularly if the fibre contains large amounts of impurities [20].

Proper radiation testing with respect to RIA of sapphire fibre and the publication thereof is not readily available and needs to be further researched. In

a recent publication from D. Sporea and A. Sporea [63] the optical attenuation as a result of gamma radiation was measured for sapphire fibre at room temperature and is illustrated in Figure 3.6.

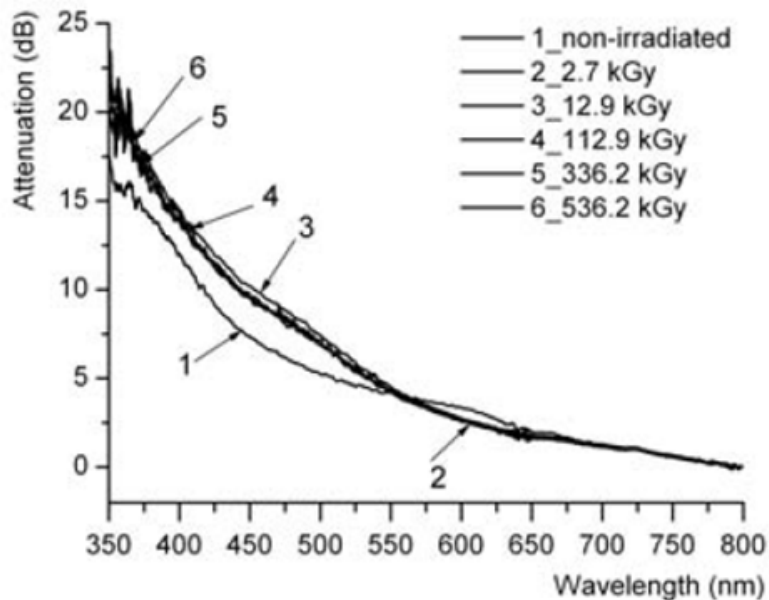


Figure 3.6: Radiation induced attenuation in sapphire fibres for different radiation levels at room temperature [63]. The length of fibre tested was 1 m.

Sapphire fibre is barely usable for data transmission in the visible light regions and below. Above 700 nm, however, the natural and radiation-induced attenuation in the fibre reaches acceptable levels. From Figure 3.6, it is clear that sapphire fibre is immune to various types of irradiations for quite high total irradiation doses (536.2 kGy) [63]. Proper gamma, neutron and mixed gamma neutron radiation data that exceeds the MGy level is required to properly assess sapphire's survivability in the core.

RIA values differ dramatically for each fibre type and sometimes even for each fibre within a batch. Every possible precaution must therefore be taken to ensure that the fibre specimens tested and the fibres used in the core are identical.

In conclusion, both sapphire- and silica-based optical fibres can potentially be used in radiation environments, provided the necessary precautions are taken in ensuring that RIA is kept to a minimum and selecting the cor-

rect operating frequency. Operating at frequencies below 800 nm should be avoided for silica as well as sapphire fibres.

3.4 Noise in Optical Fibres

Even though optical fibres are immune to interference from EMI or Radiofrequency (RF) noise sources, there exists other sources of noise that can potentially corrupt the data signal from the temperature sensor. Temperature sensing methods using amplitude encoding and extinction ratios are not recommended due to their sensitivity to any form of noise interference. FBGs, on the other hand, are frequency-encoded and the temperature is determined by calculating the frequency at which the maximum optical power is reflected. With extensive noise even this encoding method may prove to be ineffective. The main sources of noise in radiation environments are introduced in the following Sections.

3.4.1 Radioluminescence

Reactor tests done at the fission reactor SCKCEN in Belgium indicated that a strong Radioluminescence (RL) was observed in all fibre types [7]. The main contributor to the RL is believed to come from the Cherenkov emission induced by the gamma radiation. Other contributors to the luminescence also include defect creations at 420 nm and a sharp emission line at 1275 nm resulting from molecular oxygen. The general structure of the luminescence emanating from the fibre is provided in Figure 3.7.

Referring to Figure 3.7, it is clear that RL is a minimum in optical fibres around 1400 nm up until 1600 nm but remains a notable noise source throughout the wavelength spectrum.

Contrary to the expectation, RL does not decrease with a rise in temperature since the RL in the visible spectrum is dominated by the Cherenkov effect which is weakly temperature-dependent. Instead, it was noted by Brichard et al. [10] that a temperature increase results in a drastic decrease in RIA which improves the transmission of Cherenkov light. This improved transmission results in an apparent increase in the RL at the receiver side. RL is an important issue and is likely to be the dominant source of noise during sensor operation [8].

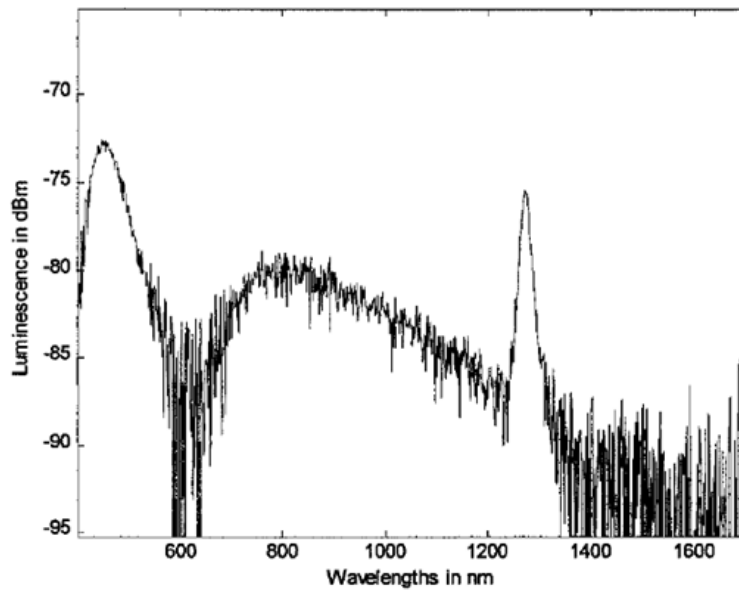


Figure 3.7: The general structure of RL measured in optical fibres. Dose rate: 5.6 MGy/h. Gamma total dose: 30 MGy. Total neutron flux: 1.01×10^{14} n/cm²s. Total fluence 2.91×10^{18} n/cm² [9].

The RL profile of sapphire optical fibres under gamma and neutron radiation in the MGy levels is not available in the literature to the best of the author's knowledge.

3.4.2 Backscatter and Laser Source Instability

Light propagating within a fibre will encounter many impurities and variations in the refractive index of the fibre, both of which will result in reflected light power back to the source. Other sources of reflected or backscattered light may include splices, FBGs and certain optical equipment. Many laser sources have isolators or similar devices that allow light propagation in the forward but not in the backward direction in order to prevent any reflected light power from reaching the laser source which would otherwise degrade their performance. This degradation in performance takes the form of laser intensity fluctuations [55].

Normally, reflected light from fibres is attenuated using isolators and the output to the receiver is the transmitted light, but since FBGs will be used as temperature sensors the reflected light is used to determine the temperature. Bad splices and imperfections in the fibre are therefore considered as poten-

tial noise sources because of their interference with the reflected light signals from the FBGs. High-quality pure fibres and correct splicing methods are therefore required to keep the Signal to Noise Ratio (SNR) as low as possible. It is essential that where connectors are required, angled connectors such as the Fibre Connector/Angled Polished Connection (FC/APC) kind are used to minimize the amount of reflected light power.

Even without reflected light entering the laser source, this instrumentation introduces a certain amount of noise into the system. Laser sources must be allowed a certain 'warm up time' to ensure wavelength and intensity stability. Source Spontaneous Emission (SSE), is the sum of all spontaneous emissions that do not include the monochromatic light signal of the laser. SSE is used to determine the total amount of noise that the laser source introduces to the system and affects the noise floor as well as the dynamic range of the measurements in the temperature sensor system. Clearly a laser source with a low SSE and narrow line width is a necessity.

3.5 Sapphire Optical Fibre

As mentioned in Chapter 1, the temperatures within the PBMR core will average at around 900°C and possibly reach 1600°C when a complete loss of coolant is experienced. Silica glass fibres can unfortunately not withstand temperatures exceeding 1000°C. Even well below 1000°C the dopants within the fibre start to diffuse and adversely affect the waveguide modal properties of the fibre, which leads to increased attenuation. The mechanical properties of the fibre are also affected since silica starts to soften and melt [27]. Sapphire optical fibre, Al_2O_3 , on the other hand, has a melting point of approximately 2054°C and can easily operate as a waveguide at 1600°C. Although sapphire fibres can operate at extreme temperatures, there are a few drawbacks in using this material as a light guide which are pointed out in this Section.

Sapphire fibre is grown with synthetic corundum, also known as $\alpha - Al_2O_3$, using either the Edge-defined Film-fed Growth (EDFFG) method or the more widely used and optically superior Laser Heated Pedestal Growth (LHPG) method. Attractive features of sapphire fibre include its ability to operate in chemically harsh environments as well as high temperatures. It is both a brittle and hard material but has been observed to decrease in strength and flexibility at high temperatures [52]. Handling sapphire fibres will in-

evitably result in surface damage and consequently a reduction in strength; cladding is therefore a necessity. Sapphire has not been widely adopted as a result of difficulties in the crystal growth processes leading to a more lossy and expensive optical guide than silica.

Sapphire fibre is usable as a light guide over the 240 nm to 4000 nm wavelength band and achieves a minimum theoretical attenuation of 0.0034 dB/km at 1780 nm. The main loss mechanisms present in sapphire fibres are Urbach, Brillouin and Multiphonon. More information on these loss mechanisms can be found in Nubling and Harrington [48]. Significant differences in the theoretical and measured attenuation in sapphire fibres occur due to unrefinements in the mechanical system used to grow these fibres [48]. The result is that sapphire fibre exhibits a large amount of impurities, colour centres, voids, inhomogeneities and surface perturbations which contributes to scattering and extrinsic losses. Impurities result from either the source material or gaseous species such as H_2O [34]. Figure 3.8 illustrates the typical measured attenuation for a sapphire fibre over the wavelength range of 600 nm to 1700 nm. It is evident that these fibres can only effectively be used over a frequency range of 1000 nm to 1700 nm even without any radiation present.

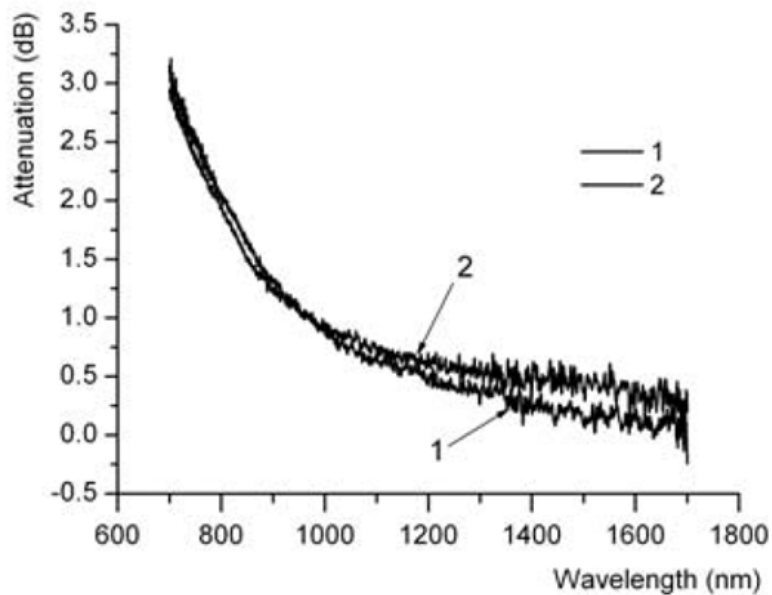


Figure 3.8: Measured attenuation versus frequency for two (denoted by 1 and 2) sapphire optical fibres [63]. Attenuation is indicated in dB where a 1 m fibre is used.

As previously seen with silica optical fibres, RL occurs predominantly below 1400 nm and is assumed to be in the same wavelength band with sapphire fibre since no conclusive information regarding this phenomenon was available. A trend can be observed in Figures 3.9 and 3.10 where the sapphire fibre is less sensitive to radiation with an increase in wavelength and has acceptable RIA within the wavelength band of 1000 nm to 1600 nm.

Sapphire fibre inserted in the core of the PBMR will be exposed to a total mixed radiation dose far higher than the gamma and neutron radiation levels that the fibres in Figures 3.9 and 3.10 were exposed to. Tests indicating the effects of higher mixed gamma and neutron radiation are currently not available to the best knowledge of the author. Sapphire fibres do, however, show excellent radiation resilience as indicated by Figures 3.9 and 3.10 and there exists no evidence that higher doses will lead to severe attenuation within the 1400 nm to 1600 nm wavelength band.

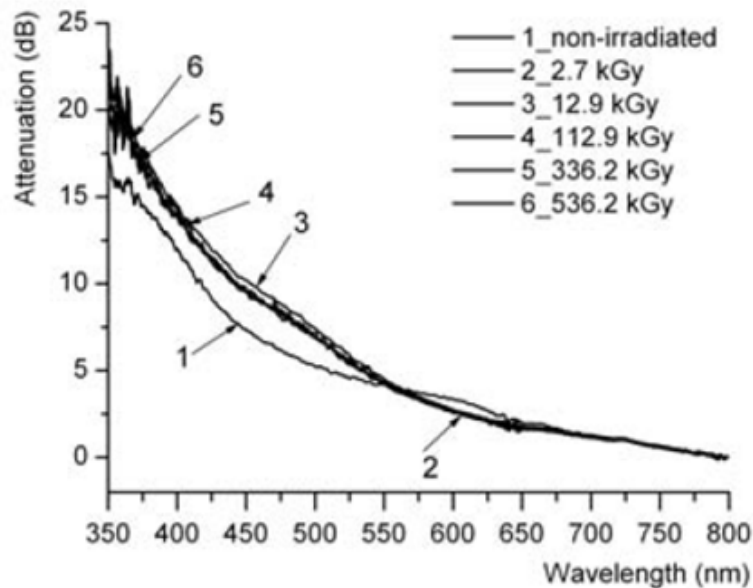


Figure 3.9: Measured attenuation versus wavelength for different levels of gamma radiation [63]. Attenuation is indicated in dB where a 1 m fibre is used.

Above 1600 nm, optical equipment becomes less common and nonlinear effects such as chromatic dispersion increases dramatically. When taking into account all of the mentioned factors it becomes clear that sapphire fibre

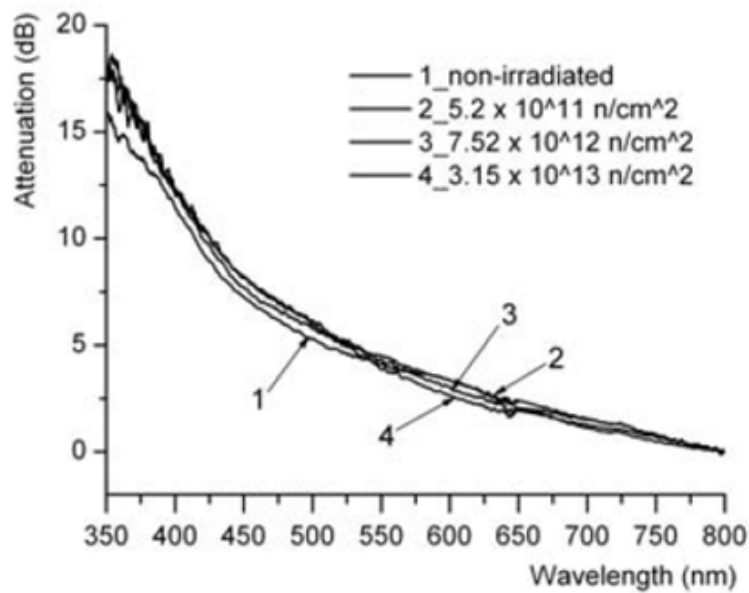


Figure 3.10: Measured attenuation versus wavelength for different levels of neutron radiation [63]. Attenuation is indicated in dB where a 1 m fibre is used.

should preferably be used in the 1400 nm to 1600 nm wavelength band where the RL, natural and radiation-induced attenuation are all at a minimum. In this range, operation with sapphire fibre down a 30 m shaft with acceptable attenuation should be possible.

Unlike silica fibre, sapphire fibres are grown without cladding, which leads to a number of undesirable characteristics. Sapphire fibres are single-crystal fibres and cannot be grown as a core-clad structure from rod-in-tube source rods, because convective currents in the molten zone quickly act to destroy the geometrical structure of the source rod [37]. Contaminants on the surface of the unclad fibre with an optical index of more than the fibre core will result in radiation losses by defeating total internal reflection. Similarly, if the refractive index of the contaminant in contact with the fibre has a refractive index lower than that of the fibre core and different than the ambient air, scattering will result at the points of discontinuity [39].

A significant problem exists where sapphire is known to incorporate impurities into its structure at elevated temperatures present in the PBMR core, which will inevitably lead to losses through scattering [65]. Cladding the sapphire fibre will potentially permit single-mode operation, improve the

waveguide properties of the fibre, prevent radiation losses, and provide mechanical support to the core of the fibre [52]. It is therefore clear that sapphire fibre must be clad and protected. Unfortunately identifying suitable materials to act as coating and cladding is a daunting task due to the number of requirements that it must meet. An ideal cladding material for use in the PBMR would have the following characteristics:

- The cladding material must be able to withstand 1600°C for short periods of time.
- The cladding must act as a successful barrier between the fibre core and the harsh environment within the core. Graphite particles must not be allowed to come into contact with the fibre core as this will result in optical power losses.
- A good bond is required between the cladding material and the core to ensure that the cladding material does not crack or peel off. This requires the cladding material to have the same thermal expansion coefficient as the sapphire core.
- Sapphire fibre is fairly radiation-resistant, as previously stated, and the cladding material should therefore be equally radiation resistant to ensure that the cladding material does not degrade and adversely affect the waveguide properties of the sapphire core under radiation.

A cladding material that is both transparent and capable of surviving temperatures in excess of 1000°C is so rare that it is believed not exist [52]. There has been some success with Al_2O_3 but unfortunately this coating is considered prohibitively expensive [14]. Other materials that have their own respective pros and cons include (x/y ratios may be varied to give different refractive indices) SiO_xN_y , Mg_xSiO_y , $\text{Ti}_x\text{Si}_y\text{O}$, alumina, silicon carbide, zirconia and niobium all of which are discussed in further detail by Pedrazzani [52].

Chapter 4

Fibre-Bragg Gratings

In this Chapter the basic operation, modelling and simulation of Fibre-Bragg Gratings (FBGs) is discussed. The radiation tests conducted on FBGs available to date in the literature was investigated and related to the PBMR. Finally, distributed sensing and general design considerations regarding FBG temperature measurement systems are presented.

4.1 FBG Modelling and Simulation

The relation between the spectral response and the corresponding FBG is the primary model that is desired. Other variables such as group delay and dispersion are not of value in this particular research. In this Section, the relationship between the FBG's manufacturing parameters and the spectral response is investigated with a mathematical and theoretical description.

A mathematical description of an FBG can be obtained by considering the energy and momentum conservation laws as described in [2]. Referring to Figure 4.1, these laws state that the incident wavevector, k_i , added to the grating wavevector, K , must equal the wavevector of the scattered radiation k_s . The grating wavevector, K , has a direction normal to the grating planes with an amplitude of $2\pi/\Lambda$. Combining the law of energy conservation and simplifying, one arrive at the familiar first-order Bragg condition:

$$2 \left(\frac{2\pi n_{\text{eff}}}{\lambda_B} \right) = \frac{2\pi}{\Lambda}$$
$$\lambda_B = 2n_{\text{eff}}\Lambda \quad (4.1.1)$$

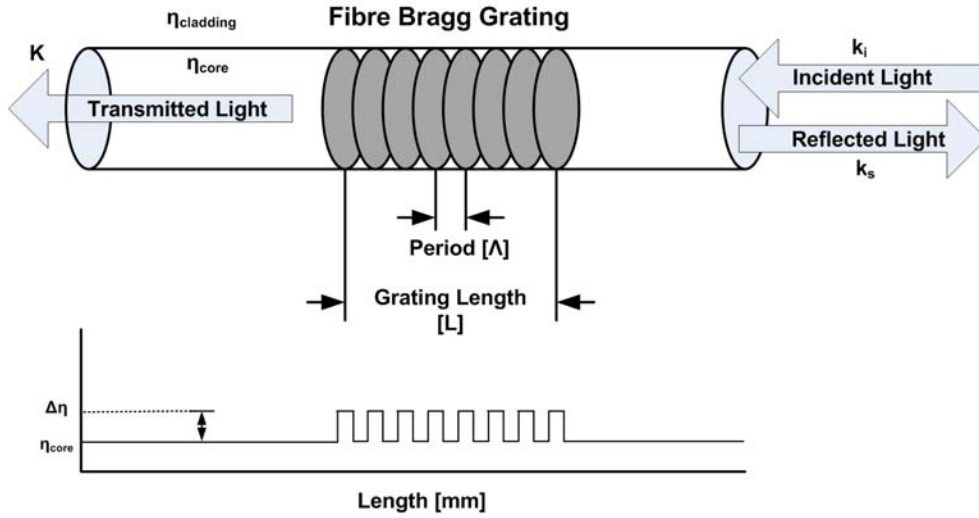


Figure 4.1: Illustrating the change induced in the refractive index to create an FBG in the fibre core.

where the Bragg wavelength λ_B is the free space centre wavelength of the reflection profile and n_{eff} is the effective refractive index of the fibre core. From Equation 4.1.1 it is clear that the Bragg wavelength is dependent on two parameters of the grating, namely the effective refractive index n_{eff} and the grating period Λ . Both the grating period and the effective refractive index are manufacturing parameters that are adjusted depending on the FBG required. The effective change to the refractive index profile $\delta n_{\text{eff}}(z)$ is often modelled as in Equation 4.1.2.

$$\delta n_{\text{eff}}(z) = \overline{\delta n_{\text{eff}}}(z) \left[1 + s \cos \left(\frac{2\pi}{\Lambda} z + \varphi(z) \right) \right] \quad (4.1.2)$$

where $\overline{\delta n_{\text{eff}}}(z)$ is the spatially averaged DC change across the fibre created by the grating, s is the fringe visibility and $\varphi(z)$ is used to model grating chirp. Chirped gratings are often used in telecommunications as dispersion compensators but are of no use in for this project and will therefore not be discussed or modelled.

The light waves travelling in an optical fibre with no perturbations are accurately modelled using Maxwells' equations. The Maxwell equations for an optical fibre have been provided in Chapter 2. Several methods exist for solving the electromagnetic waves for a perturbed waveguide where the most popular is the coupled mode equations which are the topic of the next

Section.

4.1.1 The Coupled Mode Theory

The relationship between the spectral response of an FBG and the grating itself is commonly expressed using the coupled mode theory. The coupled mode theory provides accurate solutions for the spectral response of a grating under the assumptions listed below:

- It is assumed that the fibre is lossless in the wavelengths considered.
- Only one mode of light coupling is assumed in the frequency of interest.
- The assumption is made that the difference between the refractive index of the core and the cladding is very small, in other words, it is assumed that the fibre is weakly guided.

Derivations for the coupled mode equations are provided in several articles such as [38] and [68] and will therefore not be discussed in detail. Some of the results will, however, be reproduced here. The concept behind the coupled mode theory is that the waveguide with the FBG can mathematically be represented by linear superposition of the modal field distribution without the perturbations. The different modes are designated by the index m and is given by the following equation:

$$\mathbf{E}^T(x, y, z, t) = \sum_m \left[A_m(z)e^{i\beta_m z} + B_m(z)e^{-i\beta_m z} \right] \mathbf{e}_m^T(x, y)e^{-i\omega t} \quad (4.1.3)$$

In Equation 4.1.3, the variables $A_m(z)$ and $B_m(z)$ are slowly varying amplitudes of the m th mode travelling axially within the fibre in a positive and negative direction respectively. The coefficient β is called the propagation constant for the specific medium and is described by:

$$\beta = \frac{2\pi n_{\text{eff}}}{\lambda}. \quad (4.1.4)$$

Due to the presence of a dielectric perturbation in the optical waveguide, there exists coupling between the different modes. The variables A_m and B_m , together with the transverse coupling coefficient $C_{qm}^T(z)$, are provided in Equations 4.1.5 to 4.1.7 and represents the amount of cross-coupling between the forward- and backward-travelling waves.

$$\begin{aligned} \frac{dA_m}{dz} = & i \sum_q A_q (C_{qm}^T + C_{qm}^L) e^{i(\beta_q - \beta_m)z} \\ & + i \sum_q B_q (C_{qm}^T + C_{qm}^L) e^{-i(\beta_q + \beta_m)z} \end{aligned} \quad (4.1.5)$$

$$\begin{aligned} \frac{dB_m}{dz} = & -i \sum_q A_q (C_{qm}^T - C_{qm}^L) e^{i(\beta_q + \beta_m)z} \\ & - i \sum_q B_q (C_{qm}^T + C_{qm}^L) e^{-i(\beta_q - \beta_m)z} \end{aligned} \quad (4.1.6)$$

$$C_{qm}^T(z) = \frac{\omega}{4} \int_{-\infty}^{\infty} \int \Delta\epsilon(x, y, z) \mathbf{e}_m^T(x, y) dx dy \quad (4.1.7)$$

In Equation, 4.1.5 and 4.1.6, the transverse coupling coefficient $C_{qm}^T(z)$ is defined as in Equation 4.1.7, but the longitudinal coupling coefficient, $C_{qm}^L(z)$, is usually omitted because of its negligible size with respect to the transverse coupling coefficient. Furthermore, we have the permittivity perturbation, $\Delta\epsilon(x, y, z)$, which can be approximated to $2n\delta n$ if δn is much smaller than n .

Equations 4.1.5 and 4.1.6 are called the coupled mode equations and are used to model the spectral response of FBGs in general. These equations can be further simplified when the assumption is made that index change $\delta(x, y, z)$ is approximately uniform across the core and that the dominant interaction lies near the wavelength for which reflection occurs from a mode with amplitude $A(z)$ into an opposite but identical mode with amplitude $B(z)$ [2]. When taking these assumptions into account, the new coupled mode equations become:

$$\frac{dA^+}{dz} = i\zeta^+ A^+(z) + i\kappa B^+(z) \quad (4.1.8)$$

$$\frac{dB^+}{dz} = i\zeta^+ B^+(z) - i\kappa^* B^+(z) \quad (4.1.9)$$

where the coefficients $A^+(z)$ and $B^+(z)$ are the amplitudes of the forward- and backward-propagating modes, respectively. These propagation mode

coefficients are defined in Equations 4.1.10 and 4.1.11.

$$A^+(z) = A(z) \exp(i\delta_d z - \varphi/2) \quad (4.1.10)$$

$$B^+(z) = B(z) \exp(i\delta_d z + \varphi/2) \quad (4.1.11)$$

The general DC self coupling coefficient, ζ^+ , is defined as:

$$\zeta^+ = \delta_d + \zeta - \frac{1}{2} \frac{d\varphi}{dz} \quad (4.1.12)$$

where $\frac{1}{2} \frac{d\varphi}{dz}$ is the possible chirp that the grating might have and will once again be omitted for this thesis as it serves no purpose in this application. The detuning parameter δ_d is represented by:

$$\begin{aligned} \delta_d &= \beta - \frac{\pi}{\Lambda} \\ &= \beta - \beta_D \\ &= 2\pi n_{\text{eff}} \left(\frac{1}{\lambda} - \frac{1}{\lambda_d} \right) \end{aligned} \quad (4.1.13)$$

where $\lambda_d = 2n_{\text{eff}}\Lambda$ is the design peak reflection wavelength for a very weak grating, $\delta n_{\text{eff}} \rightarrow 0$. In Equation 4.1.12, the coefficient, ζ , represents the absorption loss in the FBG and is defined in Equation 4.1.14.

$$\zeta = \frac{2\pi}{\lambda} \overline{\delta n_{\text{eff}}} \quad (4.1.14)$$

The coupling coefficient $\kappa(z)$ is defined in Equation 4.1.15 and represents the coupling between the forward and backward propagating modes which in turn depends on the position in the grating z when the grating is apodized by an arbitrary function $g(z)$. For a uniform FBG the function $g(z)$ is equal to one.

$$\kappa(z) = \kappa^*(z) = \frac{\pi}{\lambda} \overline{\delta n_{\text{eff}}} g(z) s \quad (4.1.15)$$

In Equation 4.1.15, s is the fringe visibility and is usually estimated at 1. If the FBG is uniform, then δn_{eff} is constant and the variables κ , ζ and ζ^+ also become constants. This simplifies the coupled mode equations to first-order differential equations with the following boundary conditions (refer to Figure 4.2):

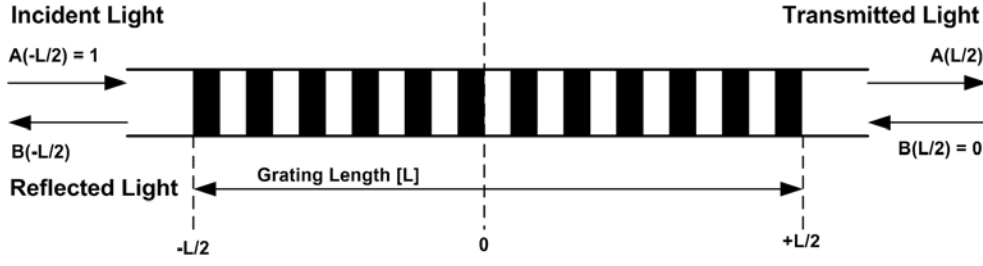


Figure 4.2: Illustrating the boundary conditions necessary to solve the coupled mode differential equations.

$$\begin{aligned} A(-L/2) &= 1 \\ B(L/2) &= 0 \end{aligned} \quad (4.1.16)$$

The amplitude of the reflection profile is then simply $R = |B(-L/2)/A(-L/2)|^2$ and is given in Equation 4.1.17.

$$\begin{aligned} R &= \frac{-\kappa \sinh \sqrt{(\kappa L)^2 - (\zeta + L)^2}}{\zeta + \sinh \sqrt{(\kappa L)^2 - (\zeta + L)^2} + i \sqrt{\kappa^2 - \zeta^2} \cosh \sqrt{(\kappa L)^2 - (\zeta + L)^2}} \\ &= \frac{\sinh^2 \sqrt{(\kappa L)^2 - (\zeta + L)^2}}{-\frac{\zeta^2}{\kappa^2} \cosh^2 \sqrt{(\kappa L)^2 - (\zeta + L)^2}} \end{aligned} \quad (4.1.17)$$

A 20 mm grating with $n_{\text{eff}} = 1.447$, a grating period of $\Lambda = 535.5$ and $\overline{\delta n_{\text{eff}}} = 0.002$ is simulated in Matlab using Equation 4.1.17 and is presented in Figure 4.3.

When analysing the returned reflection spectrum of an FBG, there are a few useful equations that can aid in determining the grating profile. Using Equation 4.1.17, we find that the maximum reflectivity for the uniform FBG is:

$$R_{\text{max}} = \tanh^2(\kappa L) \quad (4.1.18)$$

and occurs at the frequency determined by the following equation:

$$\lambda_{\text{max}} = \left(1 + \frac{\overline{\delta n_{\text{eff}}}}{n_{\text{eff}}} \right) \lambda_d \quad (4.1.19)$$

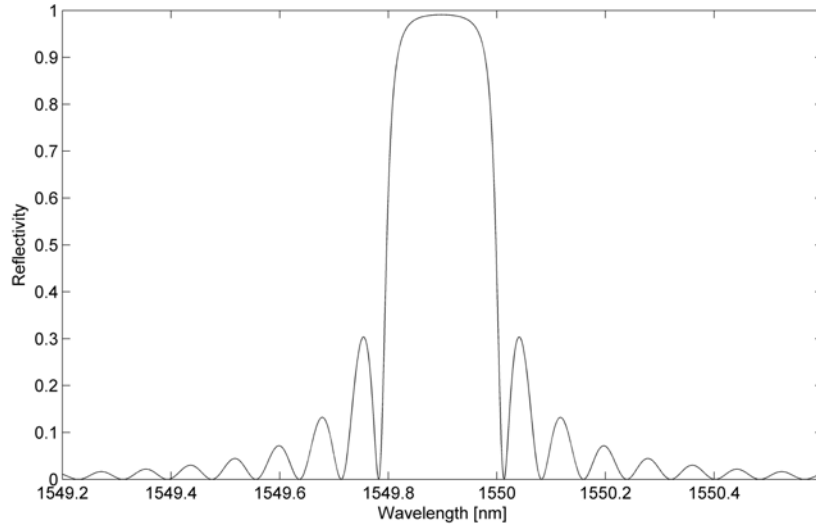


Figure 4.3: Uniform FBG with parameters: $n_{\text{eff}} = 1.447$, $\Lambda = 535.5$, $\overline{\delta n_{\text{eff}}} = 0.002$ and $L = 20$ mm.

4.1.1.1 Interpretation

To obtain a better understanding of the reflection profile of a uniform FBG, the influence of the design parameters will be evaluated graphically. The grating length L , the grating strength $\overline{\delta n_{\text{eff}}}$ and the period of the grating Λ are the parameters of interest.

The FBG length has a strong influence on the bandwidth and reflectivity of the FBG. The longer a grating the smaller its Full Width Half Maximum (FWHM) becomes and the stronger the reflectivity. When designing an FBG, it should be taken into account that making the grating longer also increases the side lobe amplitude which is generally not a desirable feature. This effect is illustrated in Figure 4.4 where the grating length is varied between 3 and 20 mm. It is also clear from Equation 4.1.18 that the maximum reflection is highly dependent on the grating length.

The grating strength, $\overline{\delta n_{\text{eff}}}$, has a more profound influence on the FBG bandwidth as well as the side lobes and maximum reflectivity. This is illustrated through Equation 4.4 since κ is directly dependent on the grating strength. Figure 4.5 visually illustrates the influence on the bandwidth, side-lobes and reflectivity where $\overline{\delta n_{\text{eff}}}$ is varied from 0.5×10^{-4} to 5×10^{-4} .

Finally, the grating period is mainly responsible for determining the cen-

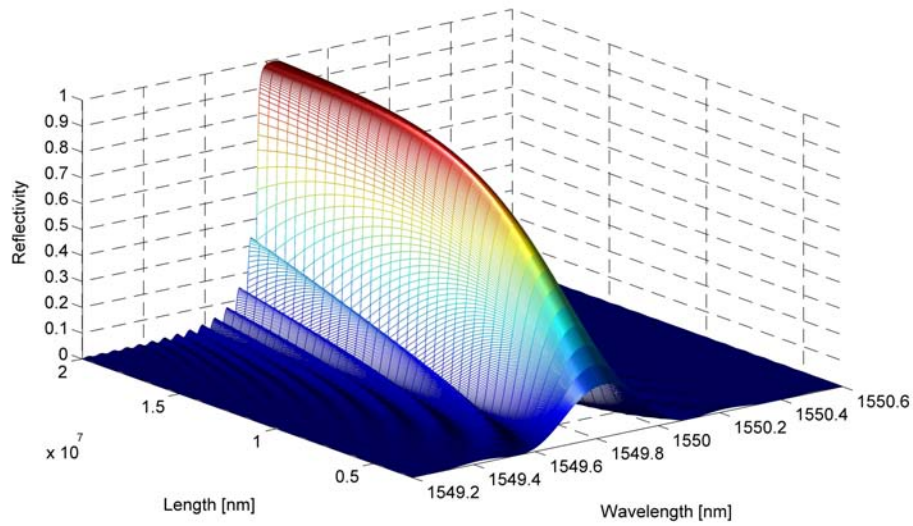


Figure 4.4: FBG reflection where the grating length is varied from 3 to 20 mm. The grating parameters are $\Lambda = 535.5$ nm, $\delta n_{\text{eff}} = 0.8 \times 10^{-4}$ and $n_{\text{eff}} = 1.447$.

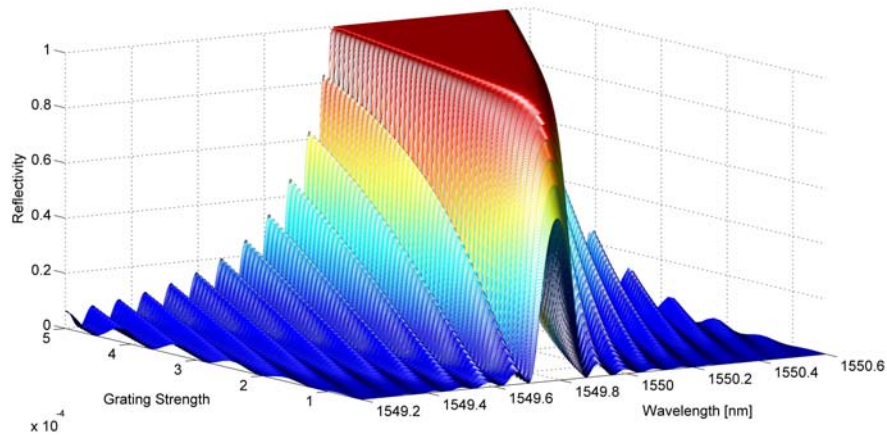


Figure 4.5: FBG reflection where the grating strength is varied from $\overline{\delta n_{\text{eff}}} = 0.5 \times 10^{-4}$ to 5×10^{-4} . The grating parameters are $\Lambda = 535.5$ nm, the length is equal to 10 mm and $n_{\text{eff}} = 1.447$.

the wavelength of the FBG. This is also seen in Equation 4.1.18 where the design wavelength λ_d is directly proportional to the centre wavelength of the FBG. Figure 4.6 illustrates the effect on an FBG when the grating period is varied from 535 to 536 nm.

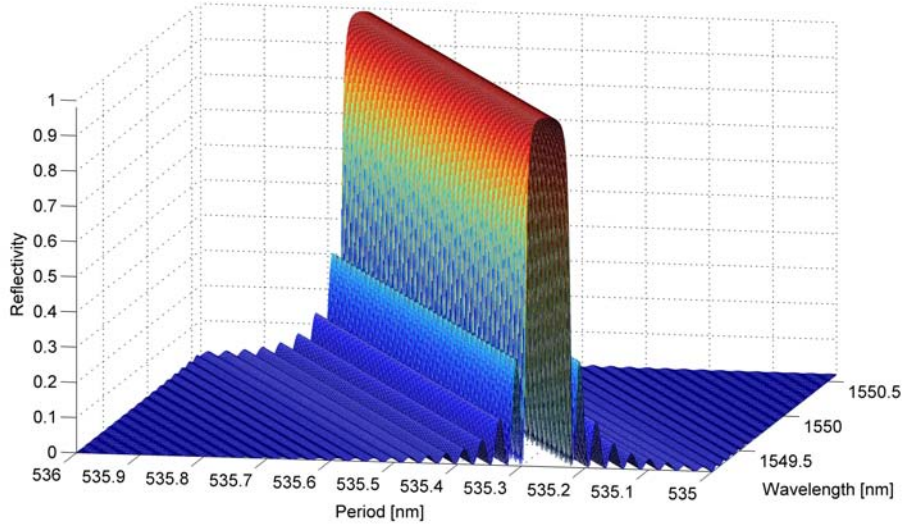


Figure 4.6: FBG reflection where the grating period Λ is varied from 535 to 536 nm. The grating parameters are $\overline{\delta n_{\text{eff}}} = 1.5 \times 10^{-4}$, the length is equal to 10 mm and $n_{\text{eff}} = 1.447$.

The figures were created in Matlab where the closed form solution in Equation 4.1.17 was solved for the stated values of n_{eff} , Λ , $\overline{\delta n_{\text{eff}}}$ and L .

4.1.2 The Transfer Matrix Method

A closed form solution for the coupled mode equations is only possible when the FBG is uniform. Solving an apodized, chirped or any other non-uniform grating requires a different approach. Several numerical methods can be used to solve the coupled mode equations, such as using a fourth-order adaptive or step Runge-Kutta direct numerical integration method or the transfer matrix method. It is also possible to combine the two coupled mode equations into one Riccati equation thus reducing the computation time since only one differential equation needs to be solved. It was, however, decided to use the transfer matrix method to solve the two differential equations since

this method has the added advantage of easily handling both apodized and chirped gratings as well as multiple gratings on a single fibre.

The transfer matrix method works on the principle of dividing the complex grating structure into several uniform gratings and then combining the results of each of the individual gratings to obtain the reflection spectrum of the grating as a whole [2]. This piecewise-uniform method that models non-uniform gratings is based on a 2-by-2 matrix model used to describe each uniform section of the grating and is provided in Equation 4.1.20:

$$T_z = \begin{bmatrix} \cosh(\Omega dz) - i\frac{\zeta^+}{\Omega} \sinh(\Omega dz) & -i\frac{\kappa}{\Omega} \sinh(\Omega dz) \\ i\frac{\kappa}{\Omega} \sinh(\Omega dz) & \cosh(\Omega dz) + i\frac{\zeta^+}{\Omega} \sinh(\Omega dz) \end{bmatrix} \quad (4.1.20)$$

where the variable Ω is as defined in Equation 4.1.21.

$$\Omega = \sqrt{\kappa^2 - \zeta^{+2}} \quad (4.1.21)$$

The grating as a whole can then be expressed as:

$$\begin{bmatrix} A_M^+ \\ B_M^+ \end{bmatrix} = T_0 \cdot T_z \cdot T_{2z} \cdot \dots \cdot T_{\frac{L}{z}} \begin{bmatrix} A_0^+ \\ B_0^+ \end{bmatrix} \quad (4.1.22)$$

Any non-uniform grating can be modelled using the transfer matrix method as long as the piecewise-uniform section chosen, dz , is much larger than the grating period, in other words $dz \gg \Lambda$.

4.1.3 Apodized FBGs

A uniform FBG is accompanied by a series of side-lobes adjacent to the Bragg wavelength. When performing temperature sensing with an FBG, it becomes very important to minimize and possibly eliminate the reflectivity of these side-lobes for two main reasons:

1. If distributed sensing is performed, it is preferable to closely space the Bragg wavelengths of the different FBGs. With a uniform FBG, quite some separation in the frequency domain is required between adjacent FBGs because of the adverse influence that the sidelobes might have in determining the centre frequency of the FBGs.

- As we have seen in Chapter 3, optical fibres exposed to radiation experience RIA as well as RL. Overall these effects lowers the SNR of the system. Eliminating the side-lobes will result in a higher SNR and avoid the possible confusion of a side-lobe with a gratings' Bragg wavelength in a distributed sensing system.

A very effective method for eliminating the side lobes of an FBG is apodization. Apodization is achieved by a contoured inscription of the grating in order to reduce the refractive index change towards the ends of the grating. Figure 4.7 illustrates a Gaussian apodization of an FBG.

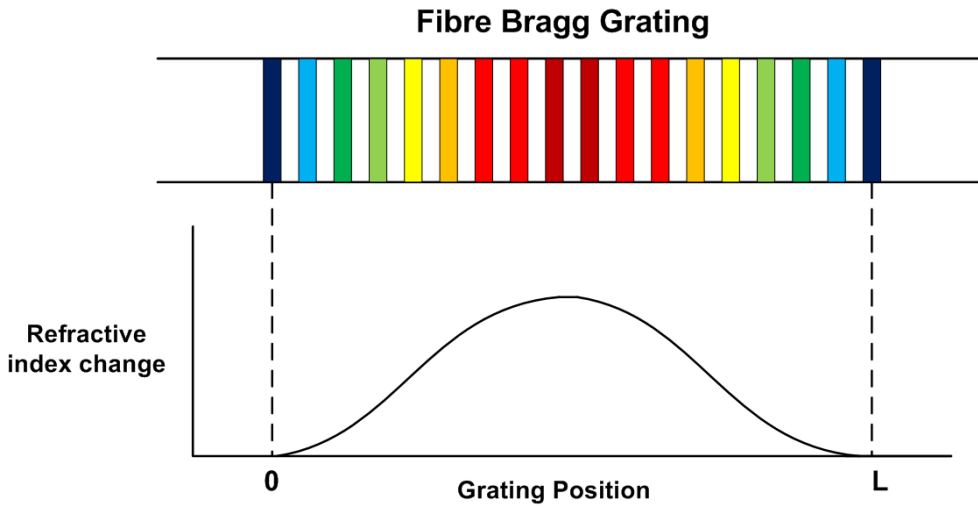


Figure 4.7: Gaussian apodization of an FBG. Note that the warmer colours indicate a larger change, whereas the cooler colours indicate a smaller change in the refractive index change.

The transfer matrix method can be adjusted to accommodate for the apodization of an FBG by replacing $g(z)$ in Equation 4.1.15 with, for example, the following Gaussian apodization function:

$$g(z) = \exp \left[-a \left(\frac{z - \frac{L}{2}}{L} \right)^2 \right] \quad (4.1.23)$$

$z \in [0, L]$

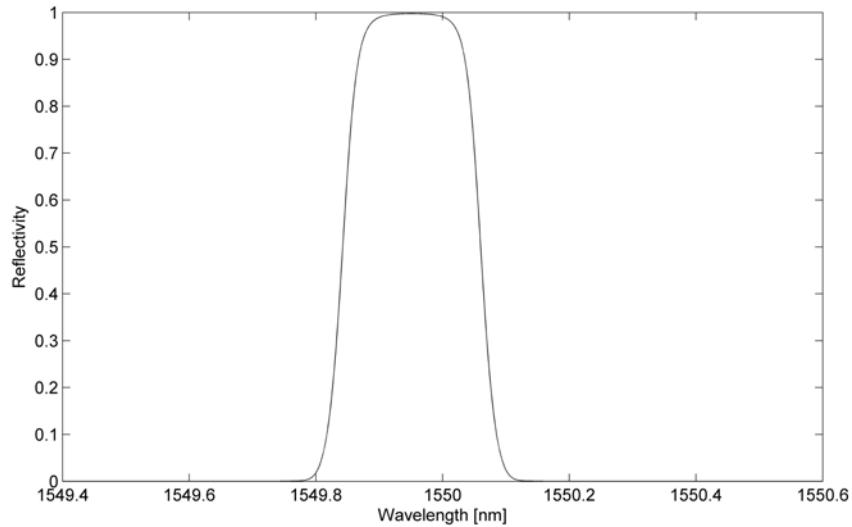


Figure 4.8: FBG with Gaussian apodization in order to eliminate the reflective side lobes. The parameters of the grating are: $n_{\text{eff}} = 1.447$, $\Lambda = 535.5$, $\overline{\delta n_{\text{eff}}} = 0.002$ and $L = 20$ mm. With a Gaussian parameter $a = 15$.

The constant, a , is the Gauss width parameter and typically varies from 5 to 30 depending on the type of frequency response desired. A larger Gauss width parameter will result in smaller side lobes and vice versa. Figure 4.8 illustrates the frequency response of an apodized FBG with a Gauss width parameter of 15. Note that all of the side-lobes have been completely eliminated.

Other apodization functions that are used in the communications industry include pure cosine, raised-cosine, sinc and Kaiser profiles. Each profile has its own characteristics but for the purpose of merely eliminating the side lobes, the Gaussian apodization profile is more than adequate.

4.1.4 Temperature Measurement

The Bragg wavelength of an FBG is determined by the grating period and the effective refractive index. Both strain and temperature affects the grating period and effective refractive index in the grating, thereby changing the Bragg wavelength [2]. With a temperature increase, the thermal expansion of the fibre causes the refractive index and period to change, whereas strain changes the period and results in a strain-optic induced change in the refrac-

tive index. The wavelength shift induced due to strain Δl and temperature ΔT is provided in Equation 4.1.24.

$$\Delta\lambda_B = 2 \left(\Lambda \frac{\partial n_{\text{eff}}}{\partial l} + n_{\text{eff}} \frac{\partial \Lambda}{\partial l} \right) \Delta l + 2 \left(\Lambda \frac{\partial n_{\text{eff}}}{\partial T} + n_{\text{eff}} \frac{\partial \Lambda}{\partial T} \right) \Delta T \quad (4.1.24)$$

The first term in Equation 4.1.24 is as a result of applied strain to the grating whereas the second term represents the change in Bragg wavelength due to a temperature change. Since there is no way to determine from the interrogated FBG alone whether the induced change is as a result of temperature or strain, strain needs to be eliminated. This can easily be done by ensuring that the optical fibre is enclosed in a sheathing that provides the necessary mechanical support.

The temperature change has a different effect on the grating length and effective refractive index for different fibres, and calibration is usually performed before installing these sensors. The following equation can then be used to determine the temperature [2]:

$$\lambda_B(T) = \lambda_B(T_0) + \lambda_B(T_0) (\alpha_\Lambda + \alpha_n) \Delta T_{\text{FBG}} \quad (4.1.25)$$

where α_Λ is the thermal expansion coefficient for the fibre, approximately 0.55×10^{-6} for silica and it varies from $4 \times 10^{-6}/^\circ\text{C}$ at room temperature up to $9 \times 10^{-6}/^\circ\text{C}$ at 900°C for sapphire fibres. The thermal expansion coefficient for sapphire over the temperature range of -100°C to 2000°C is provided in Figure 4.9. A cubic fit was made for the thermal expansion coefficient versus temperature from the data in Figure 4.9 and is provided in Equation 4.1.26; from this equation the thermal expansion coefficient for a specific temperature can be determined.

$$\begin{aligned} \alpha_\Lambda = & 1.3069 \times 10^{-15} (T + 273.15)^3 - 5.5714 \times 10^{-12} (T + 273.15)^2 \\ & + 8.3515 \times 10^{-9} (T + 273.15) + 5.0196 \times 10^{-6} \end{aligned} \quad (4.1.26)$$

The variable α_n represents the thermo-optic constant and is $8.6 \times 10^{-6}/^\circ\text{C}$ for germania-doped silica fibres. For sapphire fibre, the thermo-optic constant is frequency-, temperature- and fibre-type-dependent but can be approximated to $1.1 \times 10^{-5}/^\circ\text{C}$. This parameter is usually determined through experimen-

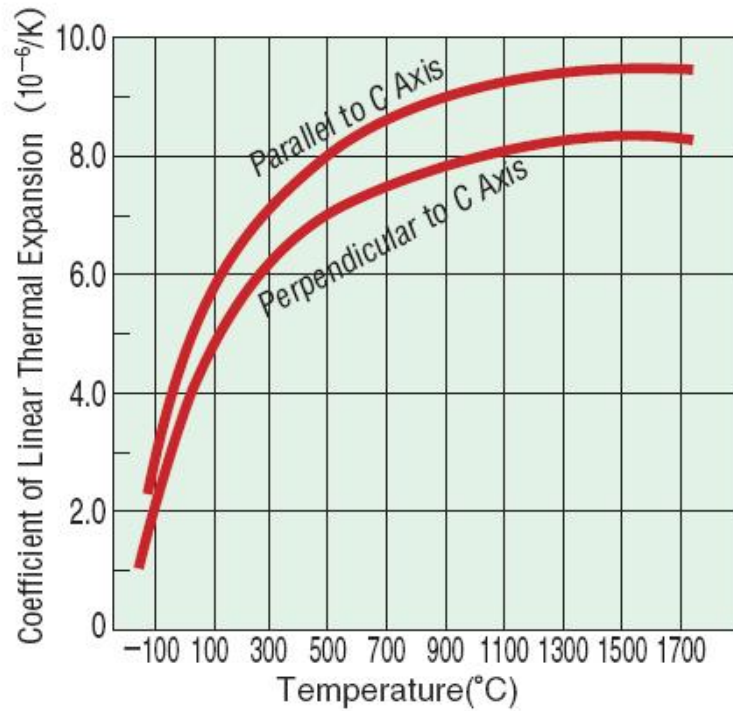


Figure 4.9: A typical curve illustrating the thermal expansion coefficient change for sapphire fibre versus temperature. This curve is representative of Kyocera sapphire fibres.

tation and Figure 4.10 illustrates the variation of effective refractive index, n_{eff} , for a typical sapphire fibre [24].

When performing temperature measurements with sapphire, it becomes essential to include the elongation of the fibre in the measured position calculation. For every metre of the sapphire fibre it was practically determined that the fibre becomes 7040 ± 20 μm longer if the temperature is varied from 22°C to 1530°C [24]. This change in length of the fibre is not linear and Equation 4.1.26 must be used to determine the elongation of the fibre at a specific temperature.

When these constants for the thermal expansion and fibre elongation are combined, a general equation can be deduced to determine the expected Bragg wavelength shift versus temperature for silica and sapphire FBGs, respectively:

$$\lambda_B(T)_{\text{Silica}} = \lambda_B(T_0) + \lambda_B(T_0) (0.55 \times 10^{-6} + 8.6 \times 10^{-6}) \Delta T_{\text{FBG}} \quad (4.1.27)$$

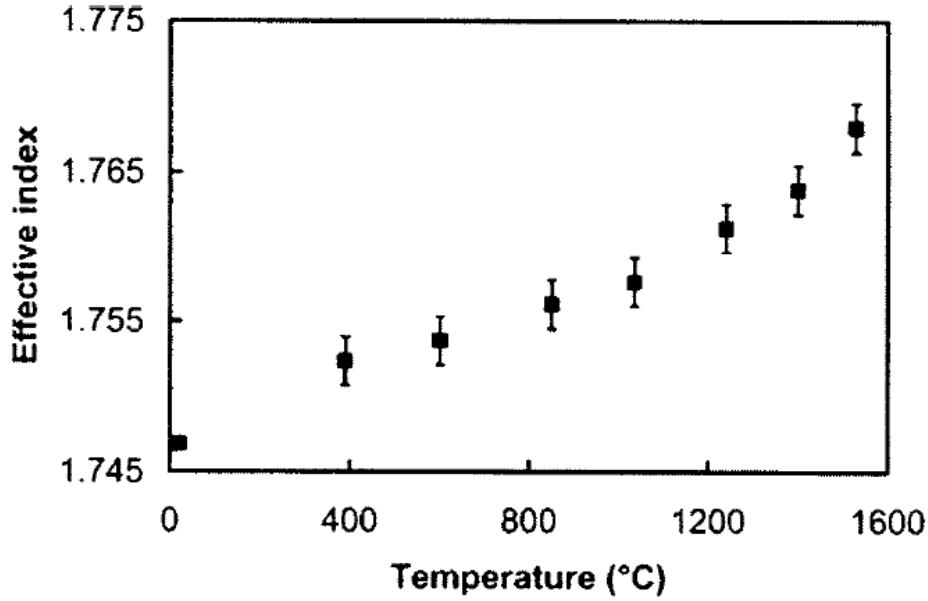


Figure 4.10: The variation of the refractive index for sapphire fibre with temperature. Error bars reflect propagation of measurement errors of the elongation length [24].

$$\begin{aligned} \lambda_B(T)_{\text{Sapphire}} = & \lambda_B(T_0) + \lambda_B(T_0)[1.3069 \times 10^{-15}(T + 273.15)^3 \\ & - 5.5714 \times 10^{-12}(T + 273.15)^2 + 8.3515 \times 10^{-9} \\ & (T + 273.15) + 5.0196 \times 10^{-6} + 1.1 \times 10^{-5}]\Delta T_{\text{FBG}} \quad (4.1.28) \end{aligned}$$

Figure 4.11 illustrates the shift in Bragg wavelength of a silica FBG. The reflection profile on the left of Figure 4.11 is that of an FBG at room temperature, where the FBG on the right is at 300°C. The 300°C change in temperature results in a linear change of the Bragg wavelength of 3 nm on average for silica. The same procedure is followed for determining the temperature with a sapphire FBG.

Performing temperature measurements with the use of an FBG temperature sensor involves the mathematical characterization of the FBG, calibration and determination of the Bragg wavelength from the reflection profile using an appropriate algorithm.

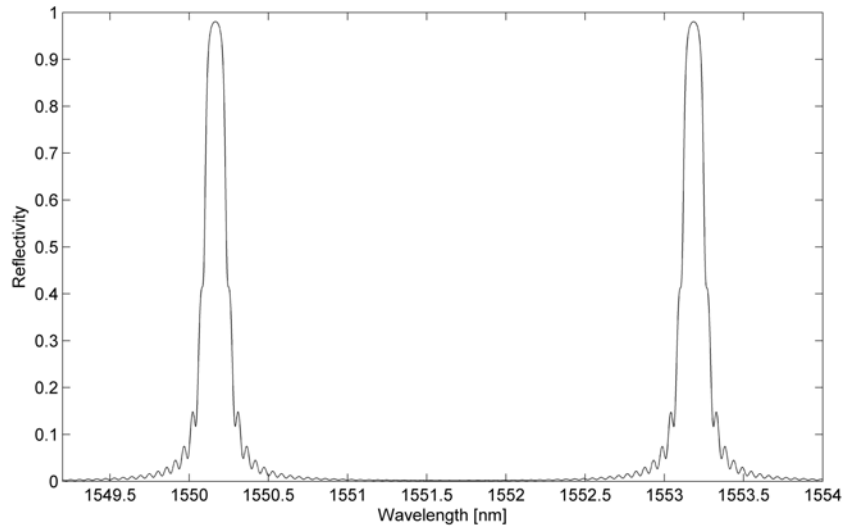


Figure 4.11: The change in centre reflection wavelength of an apodized FBG in a silica fibre with parameters $\Lambda = 535.5$ nm, $\overline{\delta n_{\text{eff}}} = 4 \times 10^{-4}$, $L = 15$ mm and $n_{\text{eff}} = 1.447$. The FBG on the left is at room temperature where the same FBG at 300°C is depicted on the right.

4.2 Radiation Effects on FBG Sensing Systems

Changes to the refractive index of the fibre, RL and RIA due to radiation present the main stumbling blocks in producing a reliable and accurate temperature sensing system in the PBMR. In the following paragraphs the impact of these phenomena on FBG temperature measurement is further discussed.

RIA and RL strongly influences the SNR of the FBG measurement system. Although the information obtained by the receiver is wavelength encoded, prolonged exposure to the high temperatures and radiation levels present in the PBMR will result in a lower SNR. The centre reflected Bragg wavelength of the FBG can become unrecognizable at all/specific frequencies since the RIA is wavelength-dependent. RL, on the other hand, will raise the noise floor by adding random noise to the system and is noted to be the dominant noise source in FBG systems operating in nuclear environments.

The effects of RIA and RL on FBGs in silica fibres have been investigated by several authors and are summarized in Sections 3.3.4 and 3.4.1. Unfortunately the RIA and RL effects have not been quantitatively investigated in sapphire fibres for extended periods of time as far as the author is aware.

Proper long-term testing regarding the RIA and RL versus radiation dose is not available in the literature but can be simulated by adding random noise and attenuating the received data. The combination of RIA and RL for a certain temperature error can then be calculated and incorporated into the measurement system. This data can then effectively determine the 'health' of the sensor system once installed as well as provide quantitative information regarding the best demodulation algorithm. The best demodulation algorithm can then be defined as the signal processing method that is able to extract the reflected Bragg wavelength the most accurately with the worst combination of RIA and RL. An example of a received FBG reflection with RIA and RL incorporated is illustrated in Figure 4.12.

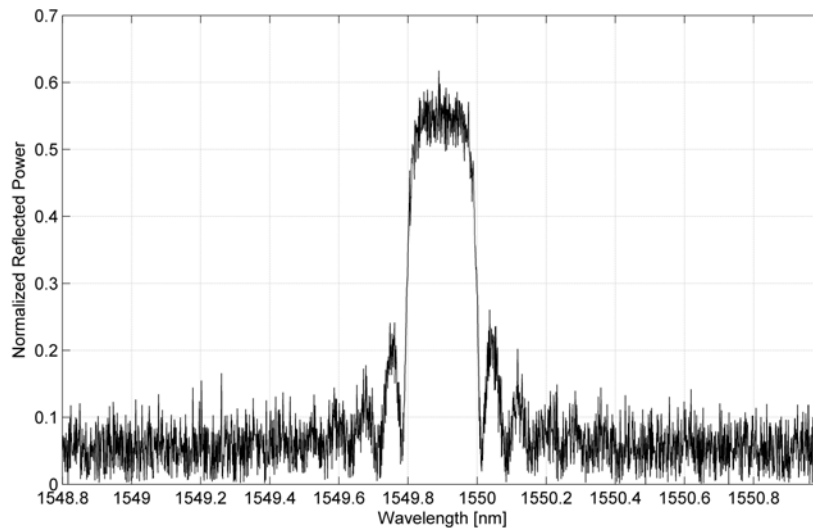


Figure 4.12: Illustrating the possible effects of RIA and RL on the measured reflection profile of an FBG. The reflection profile of the FBG is attenuated by 50% while the noise added was Gaussian in nature with a mean $\mu = 0.05$ and a standard deviation $\sigma = 0.03$.

Ionizing radiation produces defects in silica optical fibres that change the characteristics of the fibre and thereby influence the FBG's centre reflection wavelength [19]. The sensitivity to radiation of the thermo-optic coefficient, α_n , is the main cause of this radiation-induced 'drift'. Strictly speaking, the wavelength-dependent attenuation experience by an irradiated fibre should

also alter the temperature measured but this effect can be ignored since the FBG operates at a very narrow bandwidth [25].

The radiation sensitivity of FBGs strongly depends on the chemical composition of the fibre as well as the pre- and post-writing treatment. Hydrogen-loaded and non-hydrogen-loaded silica fibres undergo a Bragg wavelength shift due to gamma radiation. This shift does, however, saturate after a gamma dose of 100 kGy but does not saturate if the FBG is written in N_2 -doped fibre. The fact that the radiation-induced Bragg wavelength shift saturates indicates that the fibre can be radiation-hardened and the errors caused eliminated.

A maximum error of 5°C was observed with an experiment done at the SCK-CEN at Belgium [19] where a fibre was irradiated with a cobalt source. The lowest radiation sensitivity in silica is experienced with highly Ge doped photosensitive fibre. An example of the radiation-induced Bragg wavelength shift is provided in Figure 4.13.

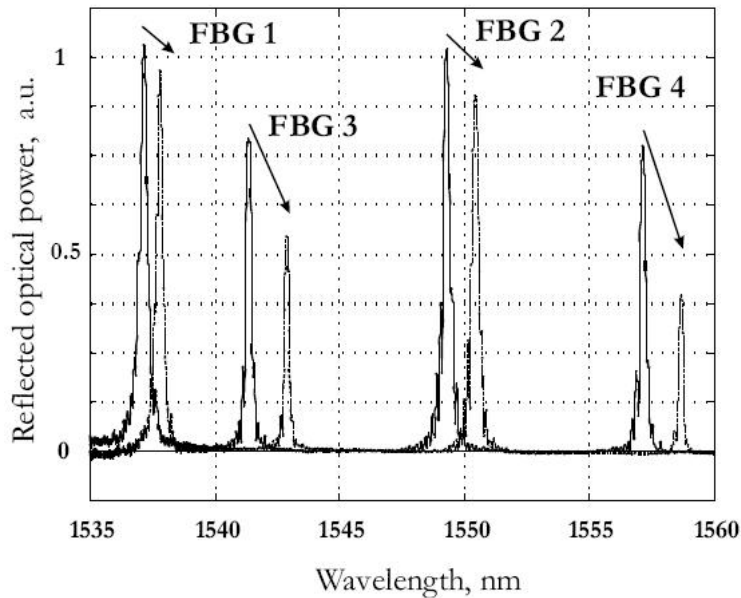


Figure 4.13: Illustrating the effect of radiation on four WDM FBGs. Note the lower reflectivity due to RIA and the change in Bragg wavelength although the temperature is kept constant [18].

The underlying physics that result in the Bragg wavelength shift in silica

due to gamma radiation is unknown. The optical fibre does, however, partially recover after irradiation has been discontinued as illustrated in Figure 4.14.

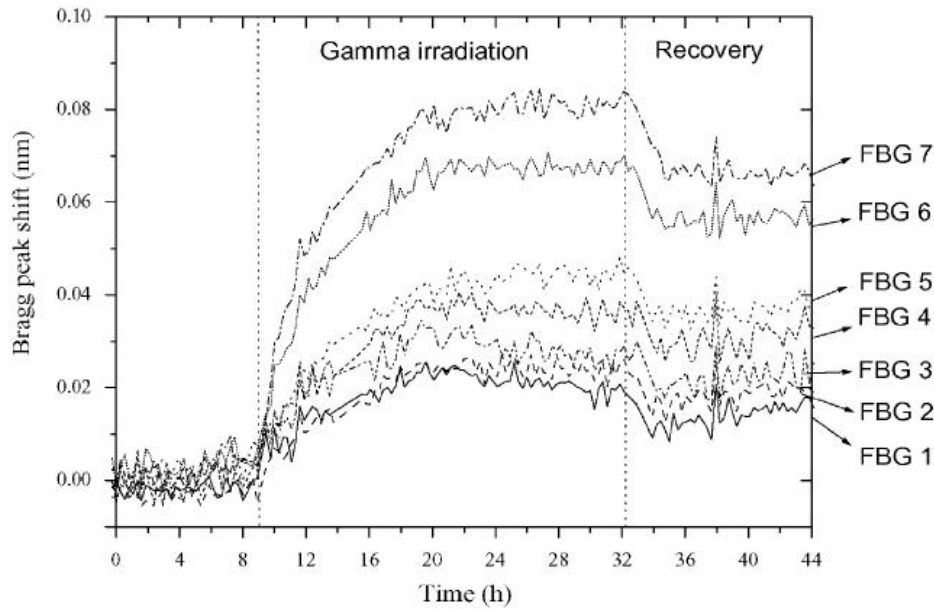


Figure 4.14: Illustrating the saturation of the FBG centre frequency shift when irradiated. Also note the how the fibre partially recovers when irradiation is discontinued [17].

Proper radiation testing on FBGs written in sapphire fibres is not available. The amount of Bragg wavelength shift for sapphire FBGs is unknown but sapphire fibre is considered as radiation-resistant when used as an optical waveguide [63]. Lessons learned from the behavior of silica fibres in radiation can in many cases be translated to sapphire FBGs and are summarized as follows:

- To minimize the formation of colour centres and other defects under irradiation, the sapphire fibre used should be as pure and defect-free as possible.
- Careful selection of a suitable cladding material is essential in order to ensure that it can withstand temperature cycles without cracking. Diffusion of foreign elements into the core needs to be minimized by the cladding material.

- Radiation-hardening should be considered before calibrations are made in order to minimize measurement errors.
- Pre- and post-writing treatment must be avoided. Femto-second laser radiation has shown promising results that do not introduce foreign elements into the fibre during the writing process.

FBGs written in sapphire optical fibre show sufficient potential to encourage further research. Radiation testing of FBGs in sapphire fibres at high temperatures, around 900°C, is especially needed.

4.3 Distributed Sensing

One of the most attractive features of FBGs used as temperature sensors is their multiplexing capabilities. FBG multiplexing techniques can be divided into 4 types, namely: time, spatial, wavelength and coherence domain multiplexing. Each of these methods has its own advantages and disadvantages and can be used together to form even more powerful measurement structures.

For the purposes of this project and the PBMR measurement problem, Wavelength Division Multiplexing (WDM) is the preferred method. This is due to the fact that, if designed correctly, WDM provides excellent performance in the presence of noise, signal attenuations and, when combined with an optical switch, can theoretically handle any number of sensing elements. In conjunction with the proper measurement and laser equipment, WDM is relatively simple to set up and provides the perfect basis for researching distributed FBG sensing systems under various environmental conditions. The reflection profile itself is also easily obtainable when an optical spectrometer is used as receiver.

4.3.1 Modelling of Distributed FBG Systems

In WDM systems, several FBGs are written into one optical fibre. The amount of FBGs that can be written into one optical fibre depends on the available bandwidth and the utilization thereof. When the fibre is excited with a broadband light source, each FBG reflects its own designed Bragg wavelength and the reflected signal can then be measured using an optical spectrometer. Figure 4.15 illustrates the FBGs written in the fibre.

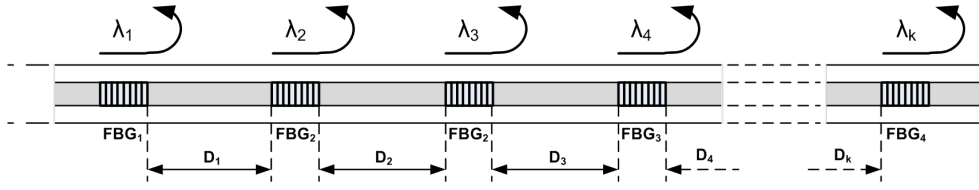


Figure 4.15: Illustrating WDM with FBGs. D_1 to D_k denotes the distance between successive gratings and λ_1 to λ_k denotes the centre reflected wavelength of the individual FBGs.

Modelling a fibre with multiple gratings is also done using the transfer matrix approach with the exception that a phase shift matrix, P_l , must be inserted between the successive grating structures. The phase shift matrix has the following form:

$$P_l = \begin{bmatrix} \exp\left(-\frac{i2\pi n_{\text{eff}} D_l}{\lambda}\right) & 0 \\ 0 & \exp\left(\frac{i2\pi n_{\text{eff}} D_l}{\lambda}\right) \end{bmatrix} \quad (4.3.1)$$

In Equation 4.3.1, the distance between successive grating elements is denoted by D_l . The total grating structure, with reference to Figure 4.15, can therefore be expressed as:

$$\begin{bmatrix} A_M^+ \\ B_M^+ \end{bmatrix} = T_0 \cdot P_0 \cdot T_1 \cdot P_1 \cdot T_2 \cdot P_2 \cdot \dots \cdot P_k \cdot T_k \begin{bmatrix} A_0^+ \\ B_0^+ \end{bmatrix} \quad (4.3.2)$$

where T_l is the transfer matrix representation of the l th grating and can be divided into fewer sections to model even more complex grating structures. The reflected spectrum of a fibre with five FBGs, 10 cm apart, is illustrated in Figure 4.16.

The temperature at each of the FBGs on the fibre is easily calculated by carefully measuring the centre reflection Bragg wavelength and substituting this frequency shift into Equation 4.1.27 for silica fibres and Equation 4.1.28 for sapphire fibres. Radiation effects for distributed FBG sensors are the same as for single FBGs, with the exception that the FBGs might experience different amounts of attenuation since RIA is frequency-dependent.

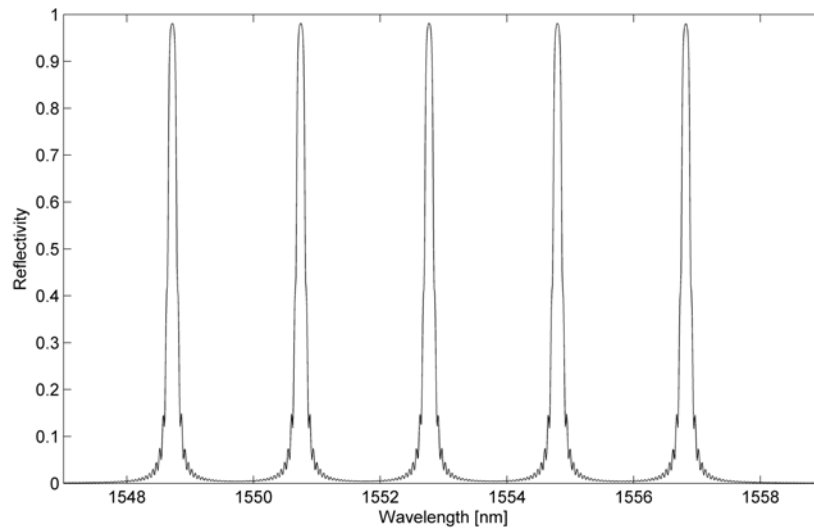


Figure 4.16: A simulation illustrating the reflection spectrum of five FBGs on a single fibre. All fibres are Gaussian apodized and have the same parameters, except for the grating period which is from left to right $\Lambda = 535$ nm, 535.7 nm, 536.4 nm, 537.1 nm and 537.8 nm, respectively.

4.4 FBG System Design Considerations

When designing distributed FBG sensors, the following considerations are crucial regarding the selection of the FBG parameters:

- The centre reflection frequencies of the respective FBGs must be chosen in such a way that they are uniquely distinguishable from the other reflection peaks with minimal interference. Factors that will influence this minimum separation parameter, $\Delta\lambda_{\min}$, include the maximum predicted temperature difference between adjacent FBGs in the wavelength domain, system noise and the effect of radiation on the refractive index.
- Side Lobe Suppression (SLS) or apodization will improve the minimum separation parameter. It is recommended that all FBGs used be apodized in order to eliminate the situation where a side lobe corrupts the adjacent FBG reflection peak.
- A trade-off exists between the length of the fibre and the bandwidth of the reflection profile. Longer FBGs have a narrow spectral width and vice versa. It is clearly advantageous that the smallest amount of

bandwidth be allocated per FBG in the fibre, but this requires a longer FBG. If a discrete point on the length of the fibre needs to be measured, then a long FBG becomes less ideal.

- Finally, the FBGs must be designed to remain within the available bandwidth of the measurement system over the entire measured temperature span.

The FBGs can be designed in such a way that they move into the allotted bandwidth of the adjacent FBG when experiencing large temperature changes. This will allow more efficient use of the available bandwidth. Equation 4.4.1 can be used as a rule of thumb to ensure that all of the FBGs remain distinguishable over the operating temperature.

$$\Delta\lambda_{\min} = FWHM + \lambda_B (\alpha_{\Lambda} + \alpha_n) \Delta T_{\max+} \quad (4.4.1)$$

The parameter, $\Delta T_{\max+}$, is defined as the maximum *positive* temperature difference expected between two discrete points on the fibre where two FBGs are located next to each other in the wavelength domain. The FWHM is used here as a modest safety parameter in the wavelength separation between two FBGs.

It is clearly beneficial to design the FBGs in such a way that those FBGs expected to have the smallest differences in temperature are located next to each other in the wavelength domain. Figure 4.17 illustrates the wavelength spacing between two FBGs on a single fibre.

4.5 Conclusion

In this Chapter it was demonstrated that uniform and apodized FBGs with a given set of parameters can be modelled. The effect on the reflection spectrum of varying the FBG inscription parameters was also demonstrated. This data can then be used to design FBG sensors for a specific application. Several guidelines were also provided in order to ensure the optimum performance of FBG temperature sensors in noisy and lossy environments.

Multiplexed apodized FBGs were modeled and simulated in Matlab; various distributed FBG sensor configurations can now be modelled. Apodized FBGs are proposed as the preferred type to be used in the PBMR.

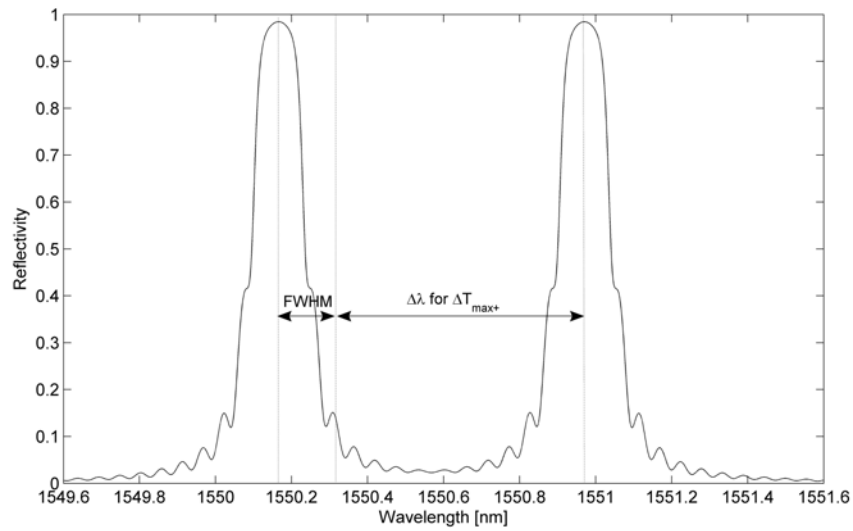


Figure 4.17: Illustrating the required wavelength separation between FBGs on a single fibre. The FWHM parameter is used as a safety factor.

A good understanding of the measured environment and its effect on the optical fibre is essential for designing robust and accurate FBG temperature sensors. Proper radiation testing of FBG sensor systems is required but thus far FBGs in sapphire fibres do show promising results.

Chapter 5

Test Platform

In this Chapter the generic FBG test setup configuration is discussed in detail. In particular, the requirements of the HRS, laser and circulator are discussed and the appropriate hardware selected. The selection of an optical fibre heating element and the temperature control thereof are also presented. This test setup will serve as the foundation upon which various FBG tests can be conducted, some of which was done in this project.

5.1 FBG Test Setup Overview

The FBG test setup was constructed to serve as a generic foundation for further research and investigation into the practical application of such a sensing technology for the PBMR. The test setup was created with the following goals in mind:

- To serve as a flexible, basic test setup where FBGs with a centre frequency ranging from 1440 nm to 1640 nm can be analyzed and characterized.
- To have the capability to control the FBG temperature from 100°C to 1600°C within $\pm 5^\circ\text{C}$. In this project, however, the heating element was characterized for temperatures below 400°C since only silica fibres were tested.
- Create an environment where stable, repeatable tests can be conducted. Environmental parameters are logged with each test using a BAR816HG weather station. This ensures that the environmental parameters such

as ambient-pressure and -temperature can be taken into account when differences in measurements are encountered.

The main constituents of the test setup include the optical spectrum analyzer from Agilent (83453B High-resolution Spectrometer), a tunable laser source also from Agilent (81600B option 200 tunable Laser), an optical circulator and a heating element with its controller. A detailed diagram illustrating the physical setup is provided in Figure 5.1.

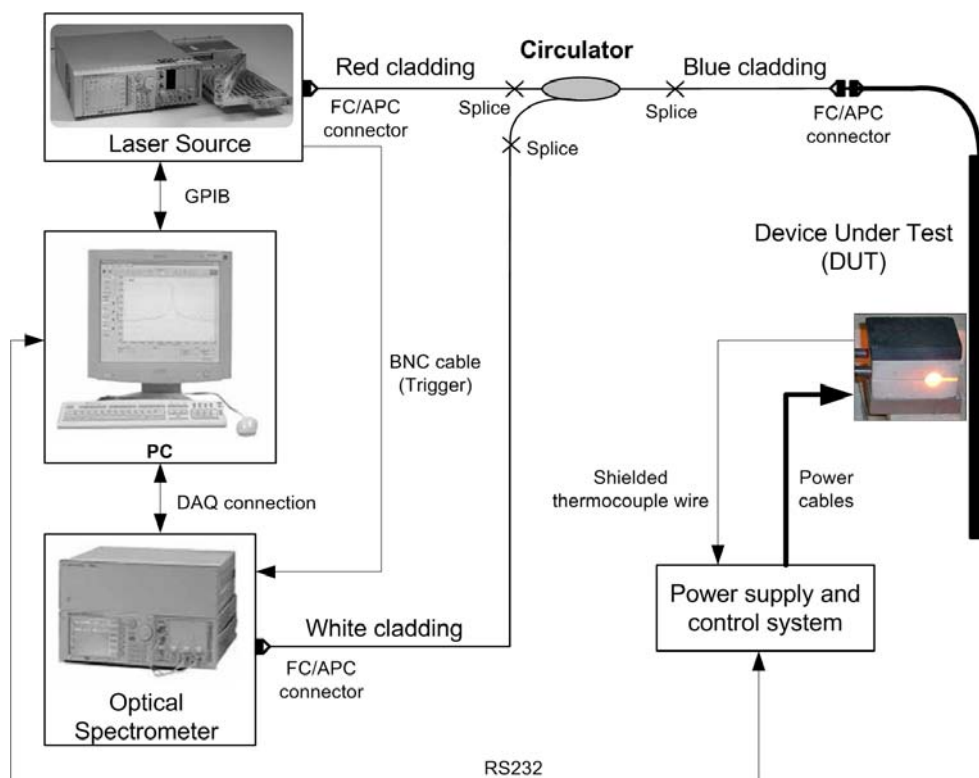


Figure 5.1: Test setup configuration.

Single-mode fibres with FC/APC connectors are used throughout the test setup to reduce loss and minimize reflections. A splice can be made after the circulator when multimode fibres need to be connected. A splice will add a considerable amount of attenuation since the multimode fibre can support the single-mode light, whereas only one propagating mode can be supported when the reflected light returns to the single-mode fibre from the FBG.

The circulator serves as an optical router for the configuration and operates as follows: Light energy radiated from the laser source is passed through to the FBG with little attenuation, whereas the reflected light from the FBG is routed to the optical spectrometer and not back to the laser source as this would cause laser power instability.

A high-current controller was built for a specialized heating element obtained from MHI heating in order to heat and control the temperature of individual FBGs. Temperature control of the Fibheat 200 heating element is dependent upon temperature readings from a B-type thermocouple when operating above 400°C, which is only accurate to $\pm 4^\circ\text{C}$, and a J-type thermocouple when operating below 400°C, which is accurate to $\pm 1^\circ\text{C}$. When performing temperature calibrations and correlations with theoretical data, this fact should be kept in mind. The reader is referred to Section 5.4 for a detailed discussion regarding the heater controller design.

5.2 Optical Instrumentation Selection

The proper characterization of FBGs requires very specialized optical equipment. Several methods exist to interrogate FBGs and all of these methods does pose their unique advantages and disadvantages. Table 5.1 discusses the possible equipment setups that can be used as well as their respective pros and cons.

The tunable laser source and optical spectrometer were chosen as a foundation for the test setup. This option does have the disadvantage of being the most expensive, but provides functionality not attainable with other interrogation techniques.

The selection process for the optical spectrometer itself was based on the requirements as outlined below. A description of why the specification is necessary is also provided.

1. Operation over the wavelength band of 1440 nm up to 1640 nm is required. Various experiments with FBGs in radiation environments have shown that the RIA and radio luminescence within this wavelength band is a minimum. Please refer to Sections 3.4 and 3.5.
2. Power accuracy over the full wavelength band of at least 3 dB. When radiation tests are conducted, it is essential to measure the RIA accu-

Type of Setup Used	Advantages	Disadvantages
Tunable narrow spectral width laser source and basic light sensitive diode as receiver.	Low-cost and simplistic operation.	Poor spectral resolution and laser source deviations cannot be corrected for. Also dependent on spectral response of receiver.
Wideband LED source and optical spectrometer.	Multiple FBGs can be interrogated at the same time.	Very expensive. Interrogation frequency cannot be selected. Low power output.
Tunable laser source and optical spectrometer.	Extremely versatile. Suitable for virtually any optical sensor system.	Most expensive setup.

Table 5.1: Comparing the most popular FBG interrogation techniques.

rately in order to perform predictions regarding the survivability of the fibre in the nuclear core.

3. Absolute frequency accuracy of ± 2 GHz. The centre frequency of the FBG will determine the measured temperature and an absolute frequency accuracy of ± 2 GHz will result in a temperature measurement error of far less than 1°C , depending on the type of grating inscribed.
4. Optical wavelength resolution of at least 0.05 nm over the full measured wavelength range. FBGs in single-mode fibres can easily be manufactured with bandwidths of less than 1 nm. A fine resolution is therefore a key specification.
5. Maximum input power of at least 20 dB. When having long fibres with multiple gratings, it is necessary to inject more light power into the fibre in order to obtain a reasonable reflection pattern from the farthest FBG while the closest might reflect all of the incident light power. An optical attenuator can alternatively be placed before the light enters the optical spectrometer.
6. Dynamic range greater than 40 dB. Detection and characterization of weak gratings as well as side lobes of gratings is required.

7. Must be remotely controllable and the measured data accessible via a Universal Serial Bus (USB) or Local Area Network (LAN) interface. Accessibility of the measured data is required.

The following requirements were set for the laser:

1. Wavelength resolution of at least 20 Mhz over the frequency range of 1440 nm to 1640 nm. When performing distributed temperature sensing the frequency spacing of the FBGs will become less and discrimination between two successive gratings will become even more critical.
2. Absolute wavelength accuracy of at least 7 pm over the entire operating wavelength when performing a wavelength sweep. Most of the measurements that will be made are frequency-dependent.
3. Wavelength repeatability and stability smaller than ± 1 pm over 24 hours. A stable injected light frequency will ensure that the reflections measured are stable.
4. A power flatness and stability versus wavelength of ± 0.3 dB. Power flatness and stability versus wavelength is required when characterizing FBGs. Power variations will cause erroneous reflected power measurements.
5. Maximum output power when performing a full wavelength sweep is required to be at least +2 dBm. This specification was set as an absolute minimum to ensure that a sufficient SNR can be maintained for as long as possible time under radiation.
6. Signal to source spontaneous emission ratio greater than 40 dB/nm.
7. Maximum sweep speed of at least 20 nm/s. The maximum sweep speed will determine the time interval between successive temperature measurements.
8. Wavelength jumps when the laser is swept over a wavelength interval is unacceptable. Wavelength jumps may result in the misinterpretation of FBG reflections.

A wideband optical circulator is required to direct the reflected light from the FBG to the optical spectrometer. The requirements for the optical circulator are listed below.

1. Operation over the wavelength range of 1400 nm to 1600 nm is essential.
2. Channel crosstalk must be suppressed by at least 30 dB. Interference between the sweeping laser source and the reflected FBG signal is not acceptable.
3. Return loss must be kept above 30 dB. Reflected light from the FBGs will cause laser source instability with some laser sources. Some laser modules have built-in protection against reflected light but since this setup is built with modularity and versatility in mind, the circulator was chosen to accommodate a source without this protection.

All of the specifications listed for the optical spectrometer, circulator as well as the laser source were chosen in such a way that every possible FBG suitable for temperature measurement in the PBMR core can be evaluated. The products that fit the application best was the 83453B high-resolution optical spectrometer (Agilent), 8600B tunable laser module (Agilent) and the PIOC3CLP2211 optical circulator (Fiberer).

5.3 Heating Element Selection

FBGs are axially inscribed into optical fibres and vary between a fraction of a millimetre to approximately 15 mm. Optical fibres themselves are hair thin without extensive jacketing and the FBGs that need heating are consequently very small. Temperatures in the core can potentially reach 1600°C if a total loss of coolant scenario occurs. A heating element is therefore required that can heat the localized area surrounding the grating. The following requirements were specified:

1. The heater must be able to heat one grating at a time if a grating frequency of 30 mm is assumed. The heating width must preferably be 15 mm.
2. The temperature close to the fibre inside the heater must be readily measurable in order to perform calibrations on the optical fibre temperature sensor.

3. Temperatures in the range of 1600°C must be attainable by the heater to test the functionality/survivability of the gratings at these elevated temperatures.

A small fibre heating element, the Fibheat 200 from MHI, met all of the above-stated requirements and was therefore used in the experiments conducted. The heater consists of a heating element (resistive wire) encapsulated in a ceramic enclosure. The Fibheat 200 is capable of reaching temperatures in excess of 1800°C which is far more than the required 1600°C. An embedded B-type thermocouple is located at the rear of the heater, reaching all the way to the core, resulting in easy and accurate core temperature measurements. For accurate lower-temperature measurements, a K-type thermocouple is placed at the front of the heating element.

According to the datasheet of the Fibheat 200, it requires 75 A maximum at 2.6 V to operate at maximum temperature which relates to approximately 200 W power consumption. A power controller was designed to regulate the heater temperature and current. A computer program written in C++ is used to control the heater temperature and provide a user-friendly Graphic User Interface (GUI).

The temperatures attainable by the heater are exceptionally high and pose a potential safety hazard if not shielded properly. A steel container was designed and built from 3 mm thick sheet metal to protect the user from possible burns if the heater should malfunction or any other accidental contact. Once the heater is inserted into the containment box, the optical fibres are supported by two protruding beams on either side extending outwards as illustrated by Figure 5.2. Spherical holes on either side allow the optical fibre to enter and exit the containment box. A ceramic fixture at the back of the heater containment box ensures that the thick power cable of the power delivery unit does not pull or distort the heating element in any way and keeps the heating element securely in its position.

Heat radiated from the heater can be compared to two average-sized light bulbs which does not pose a notable heat dissipation problem. Ventilation holes have nonetheless been drilled in the top of the container to prevent the surrounding metal and fibre from becoming too hot due to convection. As a secondary precaution, fire bricks are placed beneath the heater containment box to prevent the heated metal from damaging the operating surface.

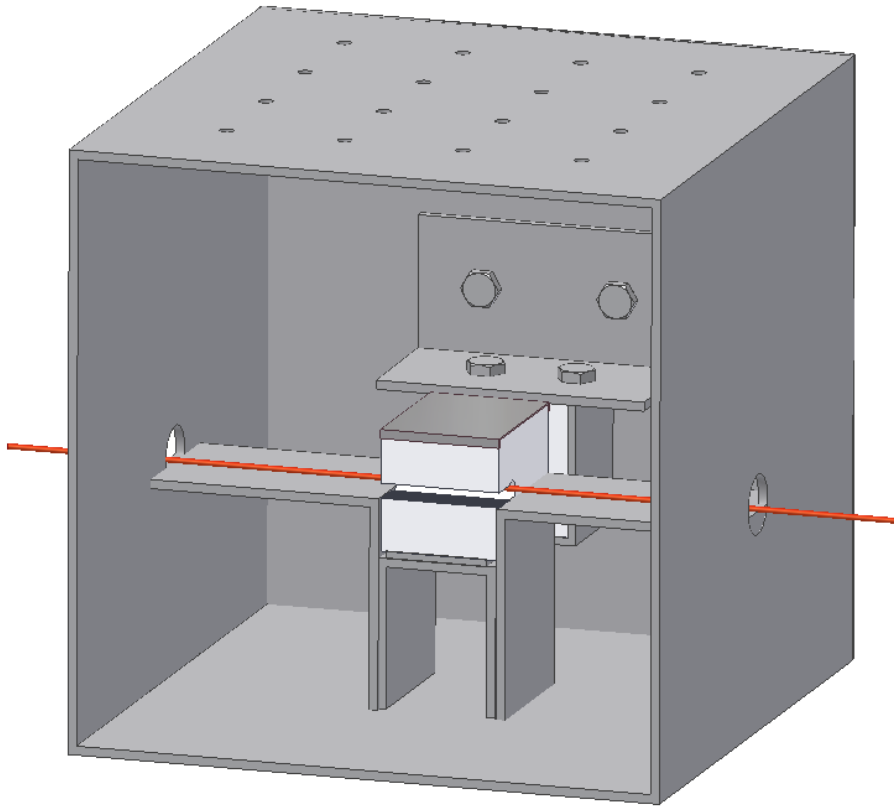


Figure 5.2: A CAD drawing of the Fibheat 200 with an optical fibre in red and the steel enclosure.

After the Fibheat 200 heating element is placed inside the containment box and connected to the power controller, the optical fibre is run through and the lid is secured to the box as illustrated in Figure 5.2.

5.4 Heater Controller Design

As previously mentioned, the Fibheat 200 heating element requires a 200 W power source capable of delivering 75 A at 2.6 V. Low-voltage high-current DC-DC converters require special design techniques in order to ensure a reasonable level of efficiency and controller stability. Since the heater controller will be used in a lab environment and portability was not a factor, it was decided to convert the utility power to a 12 V DC source and then control the power delivered to the heater using a step-down (buck) DC-DC converter. A buck converter topology is simple and effective at controlling the output

power but at these high power levels it becomes impractical. A paralleled synchronous DC-DC buck converter topology was therefore decided on. At 75 A one would require immense filters to eliminate ripple in the power supply output; fortunately a heater in itself is a filter due to the inherent thermal capacitance and high frequency ripple in the output will not influence the temperature. Taking all of the above in to consideration, a rough block diagram of the heater is provided in Figure 5.3.

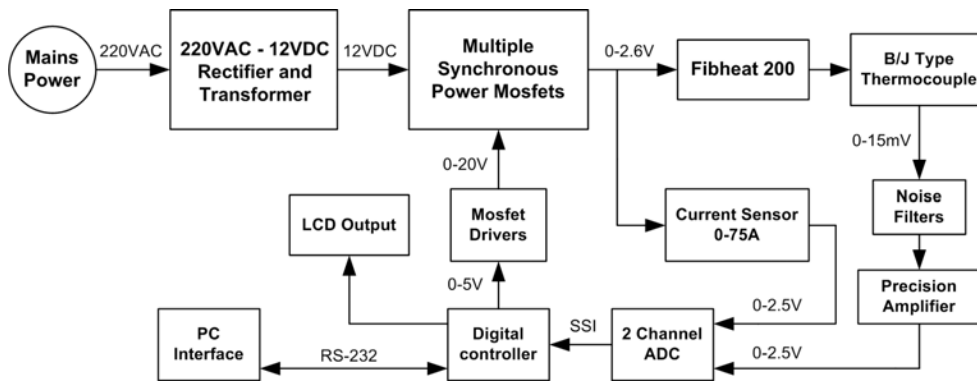


Figure 5.3: Heater controller block diagram.

In Figure 5.4 the heater controller and heating element in its containment box is illustrated. Note the thick power cable running from the controller; these wires should be mechanically supported to ensure that they do not strain the heating element. A detail design of all of the different constituents in the heater controller follow in the next paragraphs.

5.4.1 Paralleled Synchronous Buck Converter Design

The conventional buck converter where a diode and a switch (Mosfet) is used to regulate the power output to the load is far too lossy due to the power dissipated in the freewheeling diode during the off-state. A synchronous buck converter, on the other hand, allows the current to flow through the low resistance path (a secondary conducting Mosfet that replaces the freewheeling diode) during the off-state which results in a far more efficient DC-DC converter. As the name implies, a synchronous DC-DC buck converter consists of two series connected Mosfets where one Mosfet is switched on when the other is off and vice versa. When such an arrangement is used and more



Figure 5.4: The heater controller and the Fibheat 200 in the containment box. The two red buttons control the duty cycle when in standalone mode. The serial connection, which is not visible, is connected to the PC. The two thick power cables are connected to the heater element and the thin BNC cable is connected to the thermocouple. The green power button is visible in the lower left corner.

synchronous Mosfets are added in parallel, it results in quite a powerful converter capable of handling large current if the Mosfets are selected correctly. The concept is illustrated in Figure 5.5.

When selecting the Mosfets to use in the converter, several considerations must be kept in mind. One of the most important Mosfet characteristics to be considered when operating at high current levels is the on-state resistance $R_{\text{DS(on)}}$. This parameter will to a great extent determine the efficiency of the converter. The maximum junction voltage of the Mosfet is not critical but should nevertheless be more than 30 V to ensure protection against transient voltage spikes. Switching losses increase with an increase in switching frequency but at the same time relaxes the requirements on the output filters. A ripple-free output current is not required and the switching frequency is therefore kept at a minimum to minimize switching losses but above audible frequencies (> 20 kHz). Taking all of the above into consideration the IRF1607 HEXFET power Mosfet was chosen as it is an ultra-low on-resistance Mosfet, can supply a continuous drain current of 142 A (being only limited by the package) and has the capability of operating at 175°C.

The input DC voltage was chosen considerably larger than the output voltage to accommodate the potential losses at high currents. Mosfet con-

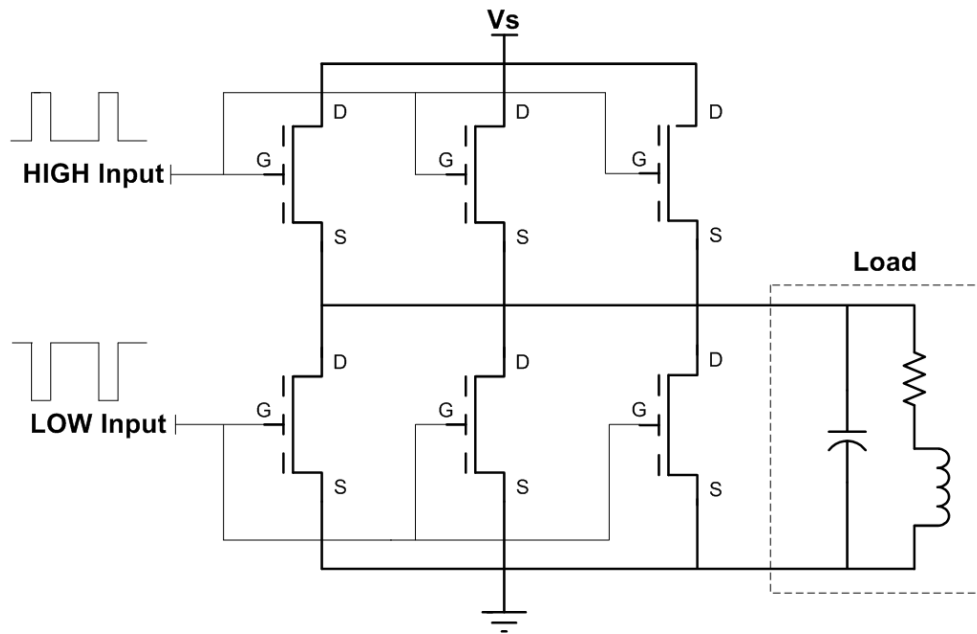


Figure 5.5: An example of the Mosfet configuration in a synchronous buck converter with three Mosfets in parallel.

duction loss contributes roughly 60% to the total power loss experienced by DC-DC converters and is calculated using Equation 5.4.1.

$$\begin{aligned}
 P_{\text{DCOND}} &= \frac{V_{\text{OUT(max)}}}{V_{\text{IN}}} I_{\text{OUT(max)}} R_{\text{DS(hot)}} & (5.4.1) \\
 &= \frac{2.6}{12} \times 75 \times 0.006 \times 2.5 \\
 &= 0.2438 \text{ W}
 \end{aligned}$$

According to the datasheet, the on-resistance is 0.006Ω , but as a worst-case scenario the resistance at the maximum junction temperature of 175°C is used; a multiplier of 2.5 corrects the on-resistance at the specified temperature. Three Mosfets are connected in parallel at the high and low side, which results in a total power dissipation in the Mosfets of 0.0813 W .

Driving the power Mosfets require Mosfet drivers and the one chosen for this application is specifically made to accommodate synchronous Mosfets. The IRS2183 is a half-bridge synchronous Mosfet driver with built-in protection to prevent shoot-through and can source a maximum drain current

of 1.8 A. Switching loss also contributes to the total power dissipated in the Mosfets and can be roughly calculated by Equation 5.4.2 now that the gate drive current from the Mosfet driver is known.

$$\begin{aligned}
 P_{\text{Dsw}} &= \frac{C_{\text{RSS}} \times V_{\text{IN(max)}} \times f_{\text{sw}} \times I_{\text{OUT(max)}}}{I_{\text{gate}}} & (5.4.2) \\
 &= \frac{1000 \text{ pf} \times 12 \text{ V} \times 30 \text{ kHz} \times 30 \text{ A}}{1 \text{ A} \times 3} \\
 &= 0.0324 \text{ W}
 \end{aligned}$$

In Equation 5.4.2, the maximum current through one Mosfet will be no larger than 30 A if three synchronous Mosfets are placed in parallel. According to the datasheet of the IRF1607, the Mosfet has a gate capacitance of 1000 pF which directly influences the estimated switching loss. The total power loss in the DC-DC converter will theoretically equal less than 1 W. These figures imply that the heatsink must be able to dissipate 1 W and that the voltage drop across the Mosfets will be negligible. This is, however, not the case practically and losses within the wiring, stray inductances and capacitances are significant when operating at 75 A.

Resistor, Capacitor and Diode (RCD) snubber circuits were also incorporated into the synchronous Mosfet design in order to reduce the generated EMI and limit the rate of change of current through the Mosfet switch. It is not practical to model the impedance of the heater and wiring at different temperatures and currents; the RCD snubbers were consequently designed through experimentation. The drive signal from the IRS2183 was also filtered by an RC network in order to minimize the Mosfet overshoot and ringing.

When filtered, the average output at a duty cycle of 50% with no load attached will be 12 V times the duty cycle D which equals 6 V. This is far above the maximum allowable voltage of 2.6 V the heater requires, but when the heater is connected with a resistance of $R = V/I = 2.6/75 = 0.0346 \Omega$, a significant amount of the power will be lost in the wiring, filters and Mosfets. The input DC voltage was therefore chosen as 12 V to ensure that the necessary power could be delivered to the heater.

In order to test the performance of the power stage, a thick copper wire was shorted over the output terminals after which the duty cycle was slowly increased until the current output reached 80 A. After operating for 30 min-

utes at 80 A the controller was deemed a success.

5.4.2 Control System Design

A PIC18F4320 microcontroller from Microchip was selected to provide the following functionality in the heater controller:

1. Control the PWM output to the Mosfet drivers-
2. Regulate the power output to the heater based on the user input from the pushbuttons-
3. Display essential information such as actual heater temperature, power usage and current temperature setpoint to the user on a LCD screen-
4. Provide the necessary current and voltage limiting for safety-
5. Interface with a C++ program that will be used to log, display and control all of the functionality of the heater.

The PIC18F4320 has a built-in PWM generator that is set up within the microcontroller by selecting a PWM frequency and then adjusting the duty cycle as required. An operating frequency of 30 kHz was selected to ensure switching losses are kept to a minimum and to prevent the noise from entering the audible frequency range. The duty cycle of the PWM output is then used to control the power delivered to the heater.

For the controller to operate as desired, several parameters need monitoring. The heater resistance changes linearly with respect to the temperature and so the temperature versus heater resistance was recorded in order to calculate the power delivered to the load. Two variables, namely the heater current and temperature are therefore required. The heater temperature and current are critical measurements and consequently a 16-bit ADC, the MX7705, from MAXIM, is used to sample these variables via a Synchronous Serial Interface (SSI) connection. The MX7705 has two channels and operates at a frequency of 60 Hz, the channel data is requested via SSI by sending a read request to the data register of the MX7705 and then storing the received data 16-bit value after 1 clock cycle. The MX7705 is referenced from a precision 2.5 V voltage reference, the MX785, and is programmed to have an internal gain setting of 1 V/V. The thermocouple voltage is connected to a precision

instrumentation amplifier that multiplies the thermocouple voltage by 91.09 in order to obtain the accuracy required. Figure 5.6 together with Figure 5.7 illustrates the control system circuit diagrams that was designed for the heating element.

5.4.2.1 Temperature Measurement Using Thermocouples

A B-type thermocouple is connected to the heating element providing an accurate temperature reading of the fibre inserted over the range of 250°C to 1800°C. Over the mentioned temperature range the thermocouple creates a thermoelectric voltage of 0.291 mV to 13.82 mV at the cold junction. Room temperature must be taken into account and the final temperature reading adjusted. This is done by manually entering the room temperature at startup of the heater controller. Once the compensated thermoelectric voltage created by the thermocouple is obtained, the temperature is calculated using two equations accurate over two separate sub-ranges; these two equations as well as the range is provided in Equations 5.4.3 and 5.4.4. All temperatures are in °C and the EMF is measured in mV and denoted with E .

For voltages between 0.291 mV and 2.431 mV:

$$\begin{aligned} T_1 = & 98.423321 + 699.71500 \times E - 847.65304 \times E^2 + 1005.2644 \times \\ & E^3 - 833.45952 \times E^4 + 455.08542 \times E^5 - 155.23037 \times \\ & E^6 + 29.88675 \times E^7 - 2.4742860 \times E^8 \end{aligned} \quad (5.4.3)$$

For voltages between 2.431 mV and 13.820 mV:

$$\begin{aligned} T_2 = & 213.15071 + 285.10504 \times E - 52.742887 \times E^2 + 9.9160804 \times \\ & E^3 - 1.2965303 \times E^4 + 0.1119587 \times E^5 - 0.0060625199 \times \\ & E^6 + 0.00018661696 \times E^7 - 0.0000024878585 \times E^8 \end{aligned} \quad (5.4.4)$$

Below 250°C, Equation T_1 becomes inaccurate and the B-type thermocouple performs less than adequately. It was therefore decided to extend the capabilities of the heater controller by allowing the user to choose between connecting either a J-type thermocouple for lower temperatures or a B-type thermocouple when high-temperature tests are performed. The transfer function used to convert the thermoelectric voltage from the J-type thermocouple to

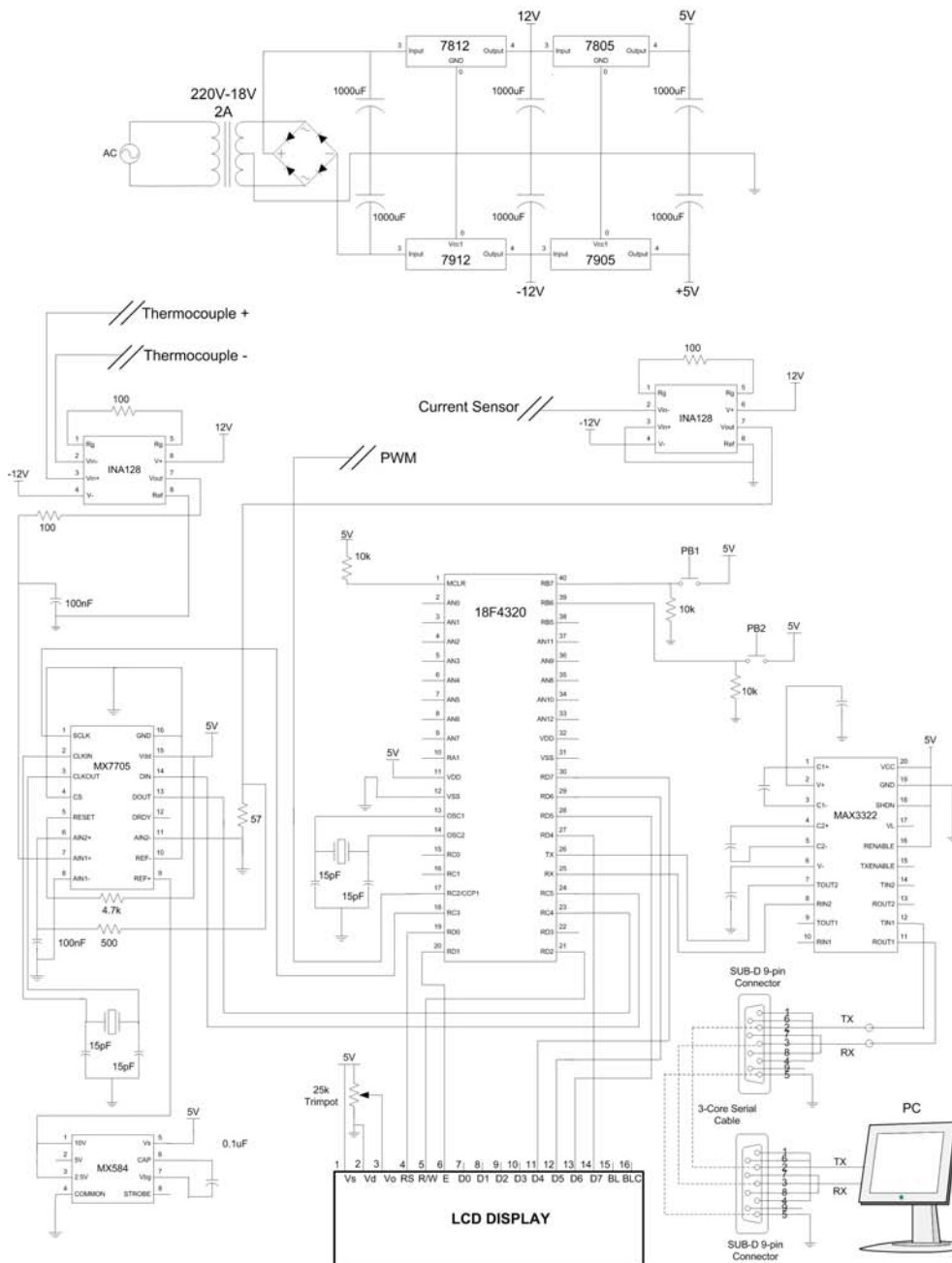


Figure 5.6: Circuit diagram of the control system for the heating element.

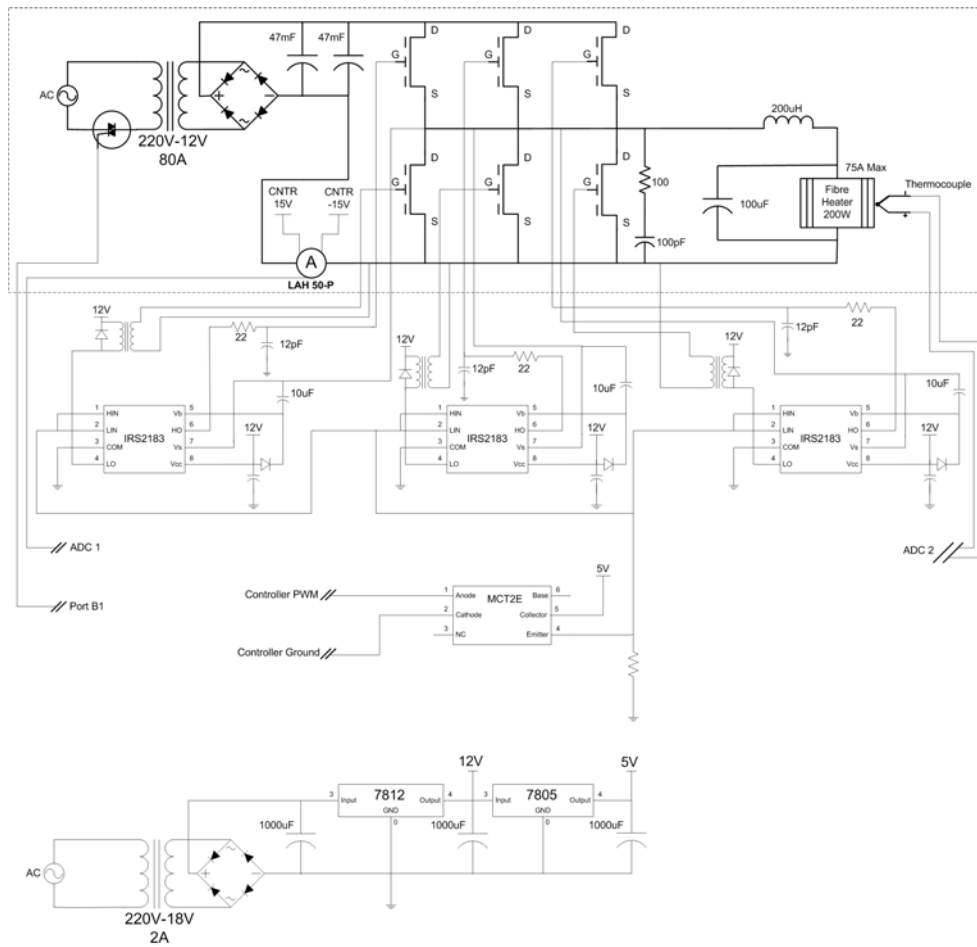


Figure 5.7: Circuit diagram of the power electronics section of the heater controller.

temperature in degrees Celcius is provided in Equation 5.4.5:

$$\begin{aligned}
 T = & 19.78425 \times E - 0.2001204 \times E^2 + 0.01036969 \times E^3 \\
 & - 0.0002549687 \times E^4 + 0.000003585153 \times E^5 \\
 & - 0.00000005344285 \times E^6 + 0.000000005099890 \times E^7 \quad (5.4.5)
 \end{aligned}$$

The selection between whether a B- or J-type thermocouple is connected can be made in the GUI and the program will then calculate the temperature using the appropriate transfer function.

5.4.2.2 Heater Current Measurement

The resistance of the heating element increases nonlinearly with an increase in temperature. This effect is corrected for by measuring the heater current and adjusting the duty cycle accordingly in order to provide a constant current to the heating element.

The LAH 50-P current sensor used from LEM measures current based on the Hall effect and can sense currents up to 110 A with an accuracy of $\pm 0.25\%$ at 25°C . The LAH 50-P current sensor is placed in series with the heater and requires a $\pm 12\text{ V}$ power supply. The output in is then connected to the second ADC input in parallel with a $56\ \Omega$ resistance. The voltage across the resistance is measured and used to calculate the current through the heater with the conversion factor $K_N = 1 : 2000$.

The current measured by the LAH 50-P current sensor is filtered in order to provide an average current output.

5.4.2.3 Computer Interface and GUI

Interfacing the PC with the microcontroller was done via a serial RS232 connection. A MAX3322 converts the CMOS logic signals to the RS232 protocol and vice versa. Communication between the microcontroller and the Borland C++ program is established by connecting the RS232 output port to the PC and running the HeaterController.exe program while the heater controller is switched on. The heater controller can be run as a standalone system and when connected to the PC has the added functionality of logging the heater temperature and current versus time. A screenshot of the control program GUI on the PC is provided in Figure 5.8.

The heater control program can be used to change the temperature control setpoint as well as log and display information such as the measured temperature, heater current output and the measured voltages of the thermocouple and LAH 50-P. The system reset button resets the connection with the heater controller and clears stored data as well as the graphs. If the log button is pressed, the data from the moment the button is pressed is saved in a text file that can be accessed at a later stage. When the log button is pressed again, the text file is closed and the logging is aborted. Care should be taken as to not press the log button a third time, as this will erase the previously saved text file and start the logging procedure from scratch.

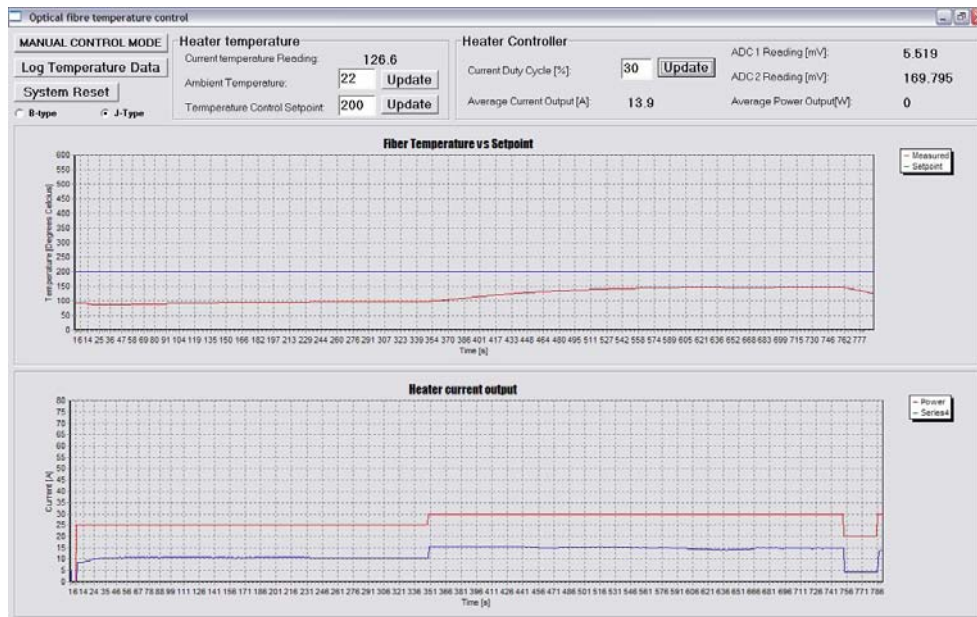


Figure 5.8: A screenshot of the Borland C++ control program on the PC.

Once the manual control mode button is pressed, the automatic control mode is engaged and the heater controller will start heating the element to the entered temperature control setpoint. If the same button is pressed again, the program returns to the manual control mode and the current output returns to zero.

The temperature is calculated using either the J-type or B-type equations depending on which thermocouple setting is selected in the main program. Program flow diagrams of the microcontroller and PC software are provided in Appendix B.

5.4.2.4 Heating Element SID

A model for the temperature response to a change in current as well as the current given a change in duty cycle is required. Initial tests will be conducted on silica fibres where the temperature will not exceed 400°C ; the models developed in this Section will therefore apply only for operating conditions below 400°C . This data can then be used to design control algorithms for both the current and the temperature. Figure 5.9 illustrates the change in heater current versus changes made in the duty cycle.

A minimum current of 10A is required for the heating element to operate

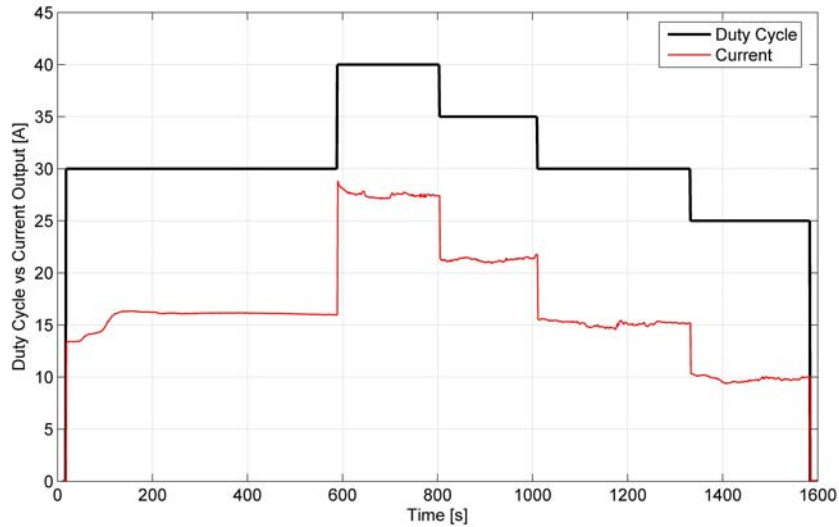


Figure 5.9: Current output to the heating element versus duty cycle which will be used as the model derivation data.

which relates to a duty cycle of 25/255. The duty cycle required to reach 400°C temperature is 40/255. A model for the current versus duty cycle, based on the model derivation data, is provided in Equation 5.4.6. Note that this model is only valid for duty cycles between 25/255 and 40/255.

$$\text{Current} = 5 \times 10^{-5} \times \text{DutyCycle}^3 + \text{DutyCycle} - 16 \quad (5.4.6)$$

Figure 5.10 presents the output of the model when a pure simulation is performed on the model validation data. Comparing the model output to the model validation data confirmed the accuracy of the model.

Once a model for the current was available, a controller could be designed and implemented in order to control the current output as discussed in Section 5.4.2.5. The current controller had to be implemented before System Identification (SID) could be performed on the temperature response of the heating element to ensure a stable output current when determining the heater's thermal response. The temperature response to several current set-points is illustrated in Figure 5.11. Note that the K-type thermocouple was used for the temperature measurement.

The temperature response of the heating element is best described by

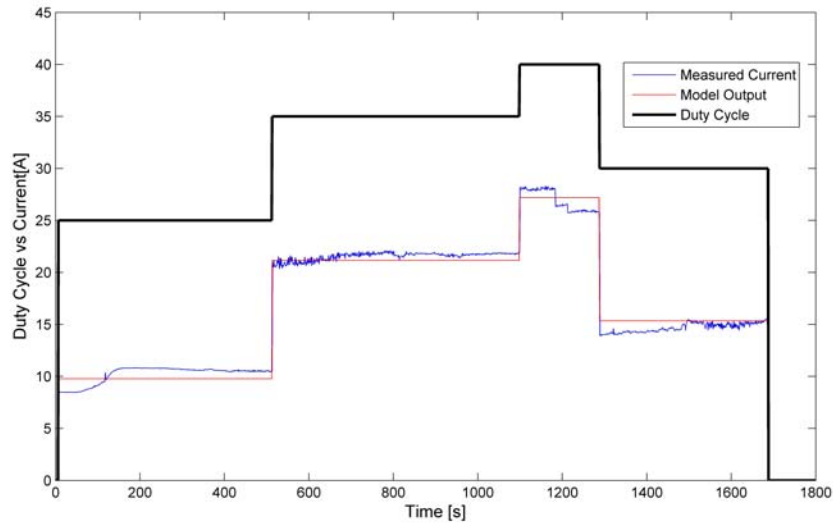


Figure 5.10: Model output compared to the measured output current for the given duty cycle. A second set of data, called the model validation data, was used to verify the model accuracy.

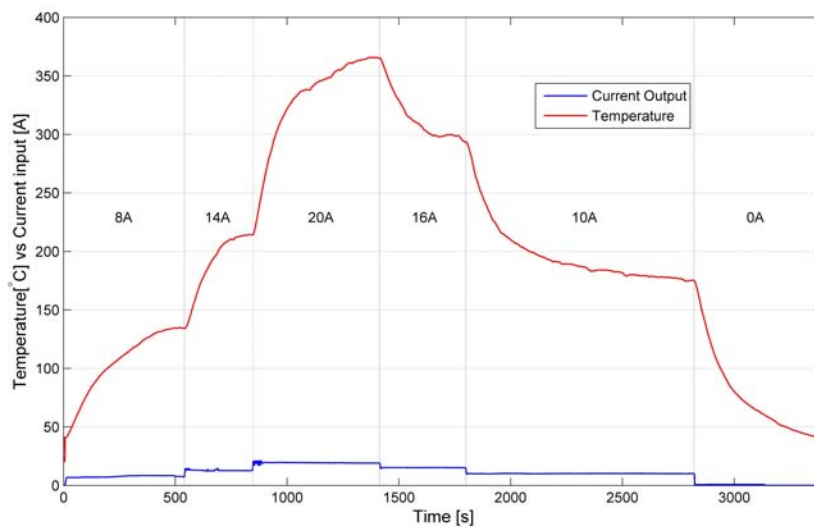


Figure 5.11: The temperature changes measured in the heating element due to several changes in the current control setpoint. This data will be used as the model derivation data.

a first-order model; the detailed model is provided in Equation 5.4.7. The model was developed using Matlab's system identification toolbox. A pure simulation was performed on the model derivation data as illustrated in Figure 5.12. Note that the heating element has a somewhat non-linear response.

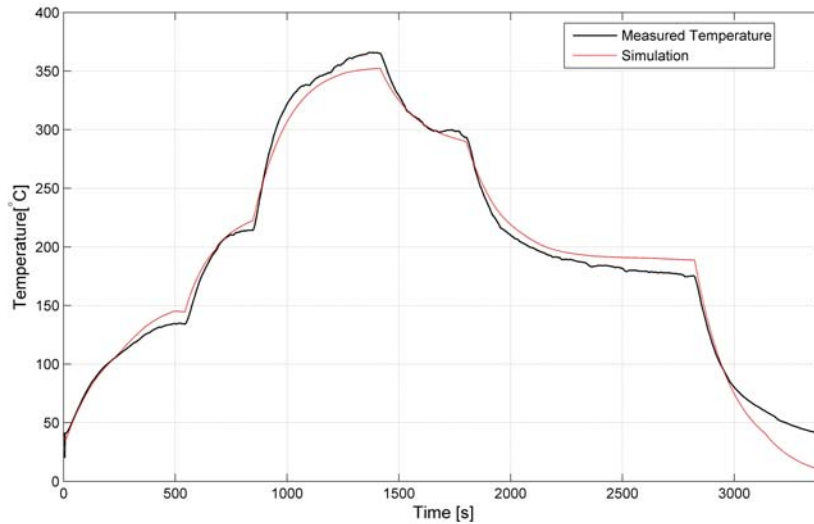


Figure 5.12: The temperature model for the heater versus measured temperature values. With the model provided in Equation 5.4.7, an 88.2% least squares fit was obtained with a pure simulation on the model derivation data.

$$G(s) = \frac{18.609}{1 + 159.46s} \quad (5.4.7)$$

In order to further verify the model's validity, a pure simulation was performed on a new set of data, called the model verification data. The Final Prediction Error (FPE) and loss function of the process model when a pure simulation is performed on the model validation data are as follows: FPE is equal to 160.6 when the loss function V is 161.3. These values are acceptable and the model can be deemed accurate for controller design purposes.

5.4.2.5 Current and Temperature Control

In the heating system there is one controlled variable, namely the output PWM, and two manipulated variables, namely the temperature and current.

Accurate temperature control is the ultimate goal of the controller design. Critical design parameters include no allowable overshoot and no steady state error. There is, however, no need to minimize the settling time for the temperature output.

Due to electrical resistance changes brought on by changes in temperature, the current does not remain constant for a given duty cycle but instead drifts as illustrated by Figure 5.9. A PID controller was designed using the root locus method and implemented in Simulink. Figure 5.13 illustrates the measured results once the current controller has been implemented and edited in Simulink to produce the desired results. The current is accurately controlled but will always have a small offset due to the coarse change in current brought on by a unit change in the duty cycle. During start-up the measured current fluctuates noticeably, but once the current has settled, the measured current remains fairly noise free.

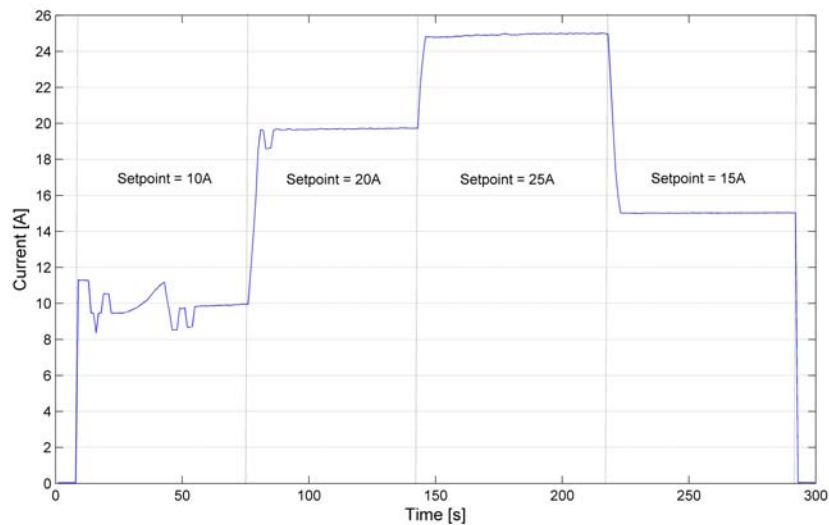


Figure 5.13: Current control in the heating element. Note the noise in the current during start-up. The current measurement settles after a while and remains fairly constant.

An outer control loop is used to control the heater temperature and consists of a PID controller with dynamic upper and lower limits. The control system as a whole was designed using the root locus method and tested and adjusted in Simulink; Figure 5.14 illustrates the functional block diagram of

the controller. The simulated closed-loop step response is illustrated in Figure 5.15 where the temperature setpoint is stepped from 200°C to 300°C.

Both the current and temperature controllers were implemented on the heater system using the velocity form. The PID control equations for the current and temperature have the form:

$$P_n = P_{n-1} + K \left[(err_n - err_{n-1}) + \frac{\Delta t}{\tau_I} err_n + \frac{\tau_D}{\Delta t} (err_n - 2err_{n-1} + err_{n-2}) \right] \quad (5.4.8)$$

Figure 5.16 illustrates the closed-loop response when the controller is implemented on the heater system. The setpoint is stepped from 100°C to 200°C to 300°C and back to room temperature. Note that the steady state fluctuations in output temperature noted in the simulations and measured results differ with $\pm 3^\circ\text{C}$. This difference is due to system characteristics not accurately modelled as well as the course change in the current with a unit change in the duty cycle.

As a final demonstration of the capabilities of the heater controller, the heating element was heated up to 1600°C for a short period of time. Due to the fragile nature of the heating element the unnecessary risk of performing prolonged tests at this temperature was avoided. The lifespan of the heating element at this temperature is unknown and temperature control above 400°C was abandoned for this project. Figure 5.17 illustrates the heating element at 1600°C.

5.5 Operating Conditions

To ensure that the specifications of the optical spectrometer and tunable laser source are within the range specified by the manufacturer, the following environmental conditions need to be met for the laser source as well as the optical spectrometer:

- The optical spectrometer must operate and be stored at temperatures between 20°C and 30°C. Sudden temperature changes and drafts should be avoided.
- Humidity should be between 15 and 80% (non-condensing).

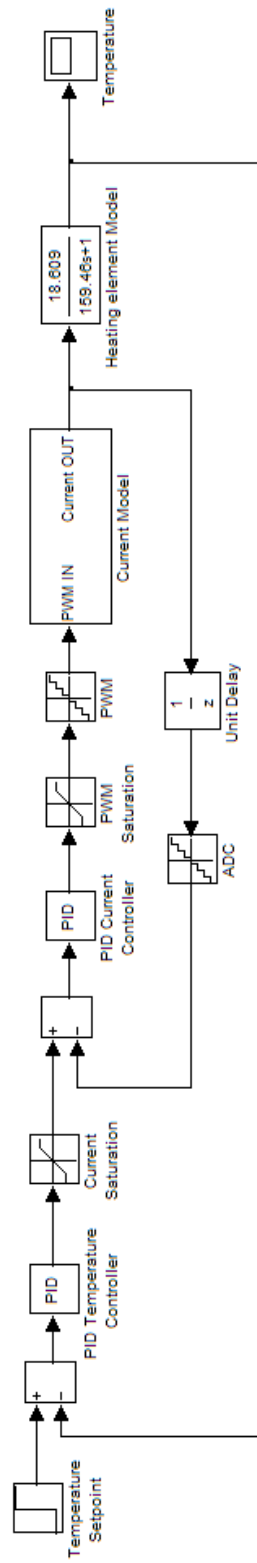


Figure 5.14: Functional block diagram in Simulink of the temperature controller for the heating element.

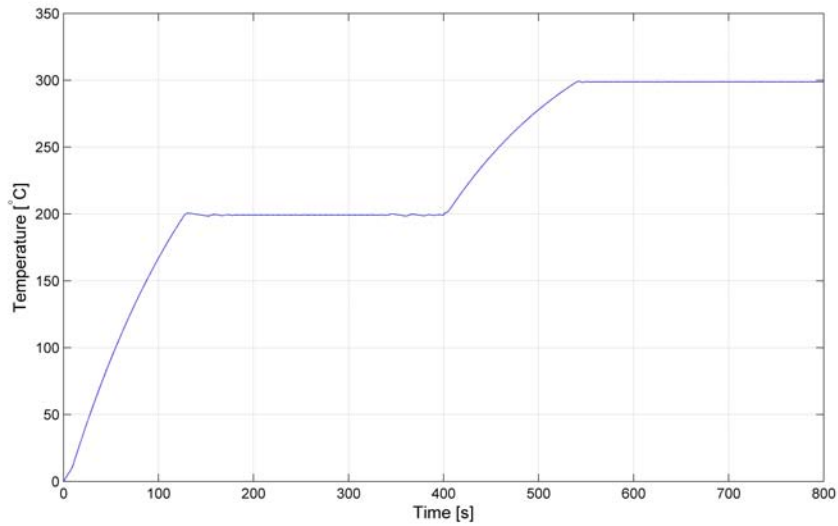


Figure 5.15: A Simulink simulation illustrating the closed-loop temperature response of the heating element. Due to the coarse control over the duty cycle, the output temperature fluctuates $\pm 1^\circ\text{C}$ around the setpoint.

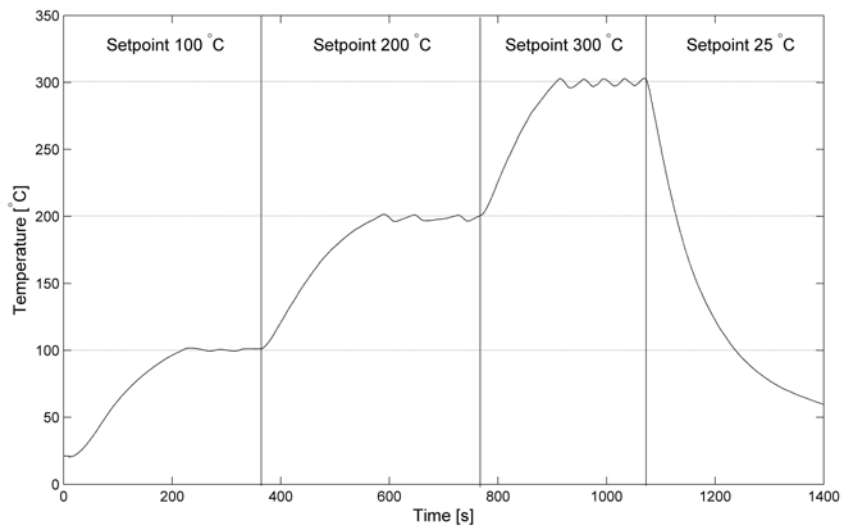


Figure 5.16: Temperature control of the heating element. The temperature setpoint is changed from 100°C to 200°C to 300°C and back to room temperature.

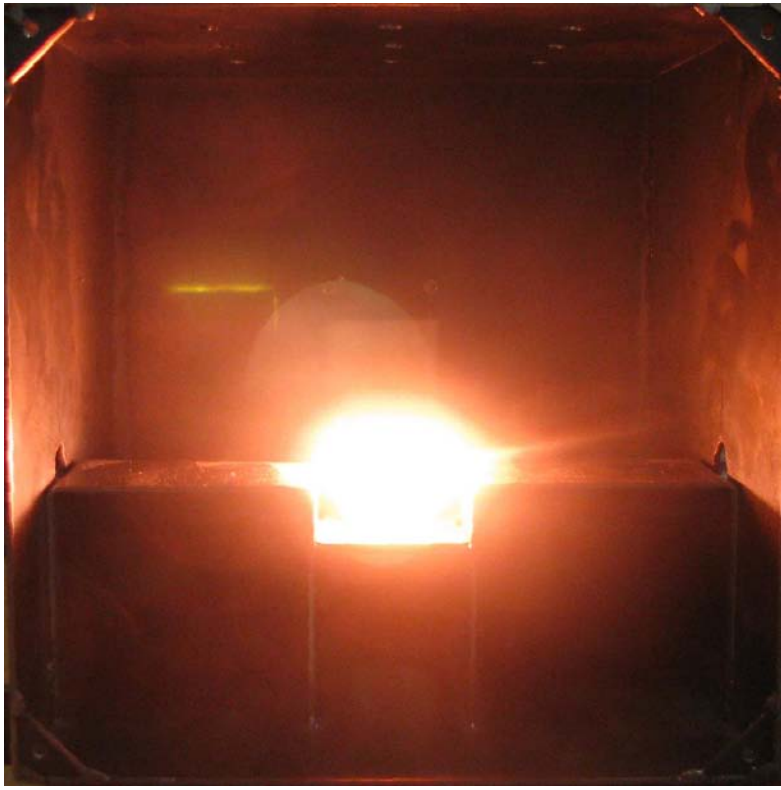


Figure 5.17: The Fibheat 200 at 1600°C.

- A standard utility power connection with 110 to 240 VAC at 50 – 60 Hz is required. The average power consumption of the spectrometer is 400 W.

The Fibheat 200 has a brittle heating element that will shatter when exposed to any type of shock or vibration. When operating at high temperatures, ensure that the power cables do not put unnecessary strain on the connections of the heater. Strain applied to the connections will cause the heater to fail when the element cools down. The heater controller requires a standard utility power connection with 240 VAC at 50 – 60 Hz. The maximum power consumption of the heater controller is 2 kW.

If a fusion splice is made after the circulator to accommodate multimode sapphire fibres, it must be made according to the following guidelines:

1. The coatings of both the fibres must be removed near the position where the splice is made. Sapphire usually does not have a cladding or coating and this step is only necessary with silica fibres.

2. Both of the fibre tips must be cleaned and cleaved to ensure a perfectly flat endface that is perpendicular to the fibre axis.
3. The two endfaces of the fibres can then be aligned and fused using an electrical arc.
4. Finally, the bare fibre area must be covered with a splice protector.

The silica and sapphire fibres are unfortunately very fragile and becomes even more so at elevated temperatures; handling any of the fibres should therefore be done with the utmost care.

5.6 Safety

The user is referred to the operating manual for general safety precautions when using the tunable laser source and optical spectrometer. The invisible laser radiation can cause serious damage to your eyesight and safety goggles with a high Optical Density (OD) over the 1400 nm to 1600 nm wavelengths must be worn at all times when operating the laser. All of the optical fibre connectors must be cleaned regularly to ensure proper operation.

The heater controller can reach 1600°C which presents a potential fire hazard when not handled with care. The immediate environment should be clear of flammable materials and the steel enclosure should preferably be placed on fire bricks to prevent damage to the working surface.

Chapter 6

FBG Measured Results

The strategy followed in this Chapter was to first calibrate the FBGs in a known environment where the temperature can be accurately controlled. This goal was achieved using an oil bath with a precision platinum RTD. An accurate and repeatable method for determining the Bragg wavelength was investigated to ensure consistency in the measured data. The mathematical equations describing the Bragg wavelength shift versus temperature as well as the reflection profile of the FBG was then compared to the measured results. Finally, the Fibheat 200 was used to perform higher temperature tests since the oil bath could only reach temperatures up to $\pm 100^{\circ}\text{C}$.

6.1 FBG Test Setup

The test setup illustrated in Figure 6.1 was used to interrogate two optical fibres with inscribed FBGs. One fibre contains a single FBG at a design wavelength of 1550 nm, the second fibre contains three FBGs at design wavelengths of 1480 nm, 1520 nm and 1550 nm, respectively. The position as well as the design wavelengths of the fibres are indicated in Figure 6.2. The two fibres are connected to the optical interrogation system with an FC/APC optical connection.

The Fibheat 200 heating element illustrated in Figure 6.1 is used where fibre temperatures higher than 100°C is desired. Initial calibration and characterization of the FBGs were performed in an oil bath due to the high degree of temperature control attainable. A picture of the test setup during calibration and testing of the optical fibres is illustrated in Figure 6.3.

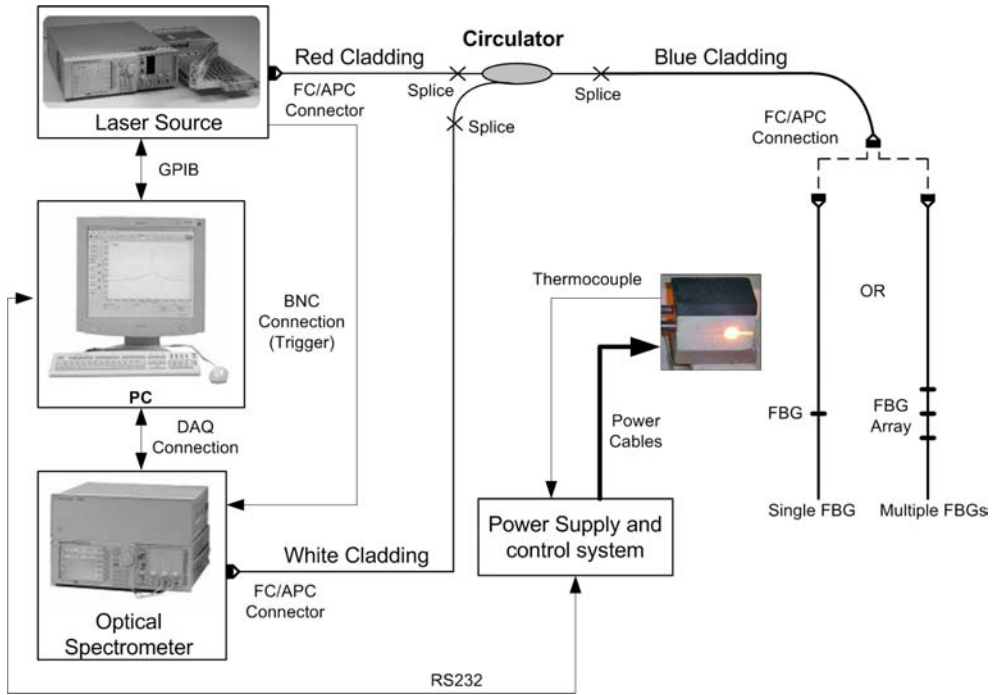


Figure 6.1: Functional diagram illustrating the test setup.

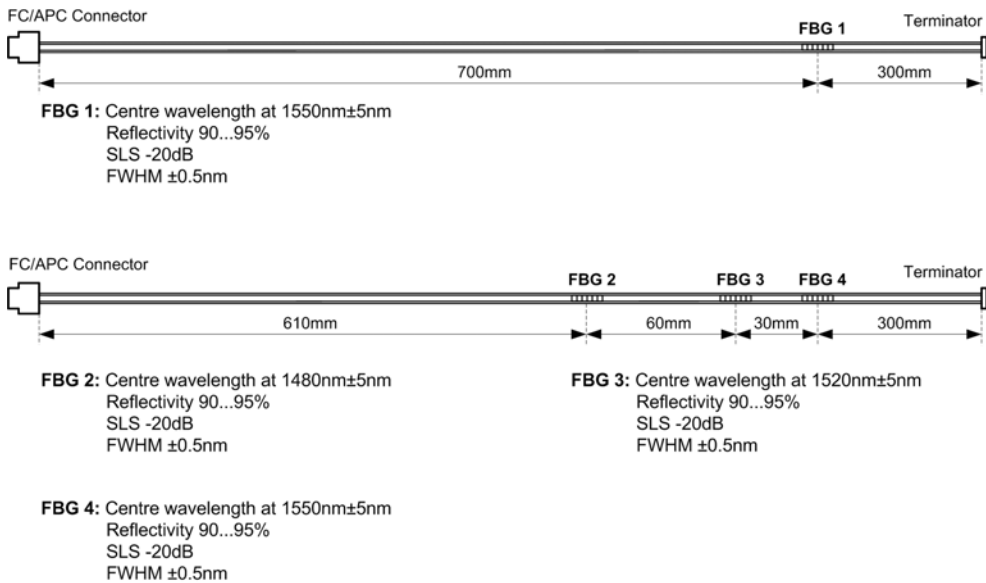


Figure 6.2: Illustrating the placement as well as the requested design parameters of the FBGs in the two optical fibres. Note the optical terminators at the fibre ends to minimize back reflections and contain the laser light. The FBGs were manufactured by a company called AOS GmbH situated in Germany.



Figure 6.3: The test setup during calibration and temperature measurements. In the background we have from left to right the HRS, laser module, control PC for the HRS, Agilent RTD measurement unit, heater controller and the PC from where the heater is controlled. In the foreground is the oil bath in which the the RTD and optical fibres are immersed for calibration. The weather station is not visible.

The correct configuration of the tunable laser source and HRS is critical to maintain consistent, accurate measurements. Please note that the wiring instructions for the HRS in the manual is incorrect; the reader is referred to Appendix A for the proper wiring schematic. The FC/APC connectors are the main source of attenuation; proper insertion is critical and they should not be overtightened. All connectors are cleaned every time a new connection is made in order to minimize attenuation loss. Even when the fibres are handled with extreme care, optical losses within the fibre varies with different orientations and each time the fibre is reconnected. All reflection profiles provided in this Section, unless otherwise stated, will therefore be normalized since the absolute values may vary dramatically.

6.2 Performing Measurements with the Agilent HRS

Accurate and repeatable results are desired and therefore strict procedures are followed before each measurement. The measurements conducted with

the Agilent HRS were performed after the initialization procedure outlined below:

1. The HRS, TLS and PC were switched on and initialized after which the TLS was left to settle for at least 2 hours.
2. A Lambda zero procedure was performed.
3. Measurements were conducted using the normal resolution mode and RMS detection method; attenuation was set at 0 dBm, and averaging was set to zero.
4. The optical fibres connecting the laser, HRS and circulator are straightened to minimize bending loss. All connectors are checked and cleaned before a new connection is made.
5. In order to ensure measurement repeatability, the environmental conditions are recorded with every measurement using a weather station. Ambient temperature, atmospheric pressure and humidity are measured and recorded with every test. Differences in measurements can then be accounted for if such a situation does occur.

Even with the above precautions the predominant source of error in detecting the Bragg wavelength remains the Agilent HRS measurement system. In this Section the internal noise of the HRS measurement system is quantified. How the measurement settings of the HRS influences the noise was also investigated.

6.2.1 HRS Characterization

The dynamic range, noise floor, laser sweeping accuracy and wavelength accuracy are among the most important parameters that has to be taken into account when performing measurements with the HRS.

The noise floor, together with the laser noise of the HRS, plays an important role in determining the maximum allowable extraneous noise. The most conservative measurement setting is when the laser sweeping speed is at 1 nm/s with 1 mW output power; this setting will be used for the FBG measurements. When the laser output is connected to the spectrometer input the system noise as a whole (laser noise and HRS measurement noise)

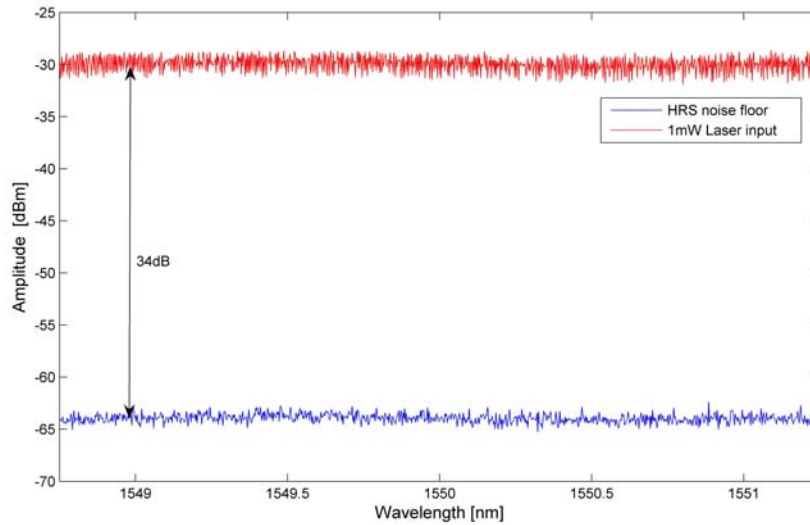


Figure 6.4: Illustrating the noise floor as well as the measured spectrum when the laser output is connected to the HRS input. laser sweeping speed was set to 1 nm/s and the laser power was set at 1 mW.

can be measured. Figure 6.4 illustrates the noise floor at -64 dBm as well as the measured spectrum when the laser is set at 1 mW and connected to the HRS input. A 34 dB dynamic range is available for FBG measurement which is more than adequate and will ensure a minimum SNR of 10 dB.

Measurements with the HRS will mostly be made in the Normal resolution mode with a laser sweeping speed of 1 nm/s. Increasing the laser sweeping speed will lead to an increase in system noise. The total inherent noise of the HRS and laser can be mathematically represented by a normal distribution with a mean $\mu = -64$ dBm and standard deviation $\sigma = 0.273$ dB. Figure 6.5 illustrates this normal distribution fitted to the inherent system noise when the laser sweeping speed is 1 nm/s and the Normal resolution mode is used.

The Agilent 81600B series tunable laser source can provide a maximum of 7.514 mW per channel when in high power mode. Increasing the laser power output beyond 3 mW is not recommended due to the substantial increase in system noise as illustrated by Figure 6.6. The cyclic change in laser power output has such a small period that it will result in unacceptable errors in the peak detection of the FBG.

It is important to note that relative power measurements rather than the

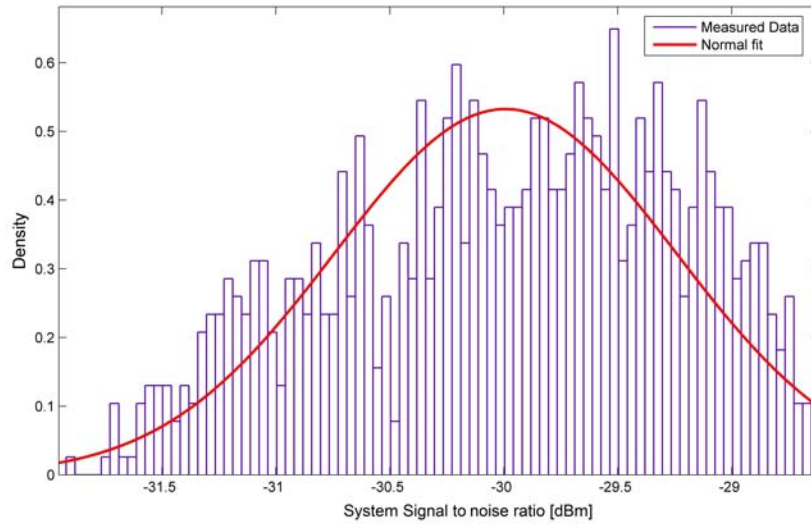


Figure 6.5: A histogram illustrating the signal to noise ratio of the laser and optical spectrometer. The noise can mathematically be represented by the normal distribution in red with a standard deviation of $\sigma = 0.273$ dB.

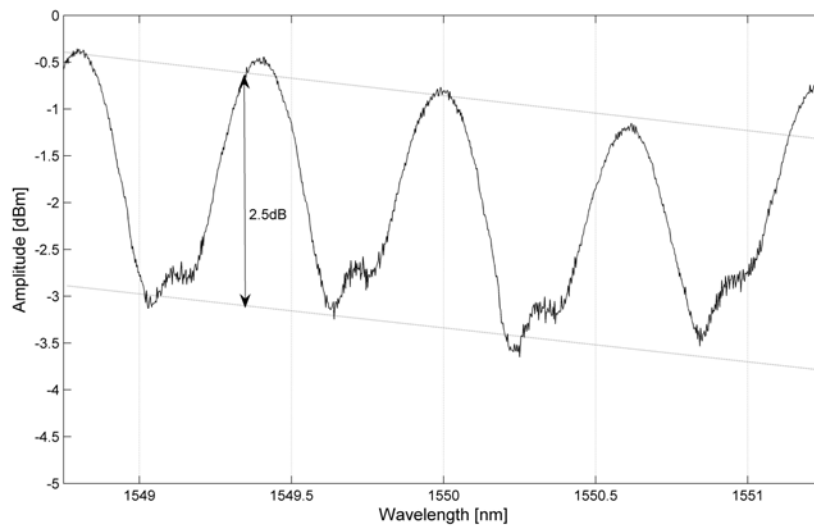


Figure 6.6: Cyclic power variations observed when the laser output is 7.5 mW. The cyclic power variations are minimized by keeping the laser output power below 1 mW.

exact values are useful because of the varying attenuation from the FC/APC connectors. The HRS itself has a power accuracy of ± 2.75 dB. The dynamic range of the HRS is, according to the user's guide, ≥ 50 dB which is far more than required and will not negatively influence the measurements.

Wavelength accuracy on the other hand is critical for accurate temperature measurement; according to the data sheet the HRS has an absolute wavelength accuracy of ± 15 pm which relates to a theoretical temperature measurement error of approximately $\pm 1.5^\circ\text{C}$ [2].

6.2.2 Interface

A software package written by Agilent is used to control the HRS and perform measurements. Figure 6.7 provides a screenshot of the software GUI on the controller PC. Once a measurement is performed, the data is saved as a Comma Separated Values (CSV) file with two columns; one column containing the wavelength and the other the corresponding power measured at that wavelength in dBm. A Matlab script was written to read the CSV file and store the data in Matlab for further processing.

6.3 Optical Fibre Calibration and Characterization

The optical fibres as well as the J-type thermocouple was calibrated in an oil bath before temperature measurements were conducted with the Fibheat 200. In an oil bath the environment surrounding the FBG can be controlled more accurately than in the Fibheat 200 heating element due to the unknown heater characteristics and thermocouple inaccuracy.

A platinum 4 W RTD calibrated by the CSIR and accurate to 0.0015°C was used as a precision temperature reference in the oil bath. The optical fibres were first covered in aluminum foil to protect them from the oil and inserted into the oil bath together with the thermocouple of the Fibheat 200. In Figure 6.8 a diagram of the calibration process is presented.

The oil bath is rated for temperatures up to 130°C and the temperature is manually controlled with a variac. The optical fibres were interrogated at three different temperatures in the oil bath namely 25.64°C , 62.36°C and 103.08°C . These are the temperatures at which the oil bath settled after several hours of operation.

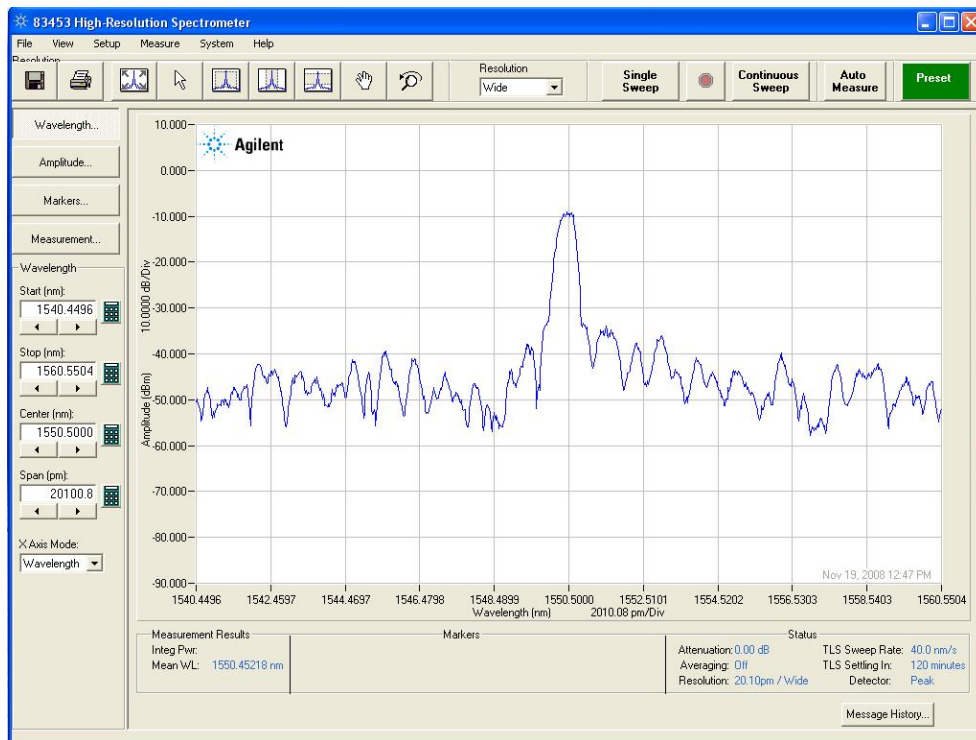


Figure 6.7: A screenshot of the Agilent software used to control the laser and HRS. Visible in the screenshot is the typical spectral response of a FBG.

A model, based on the data from the oil bath, was developed for each of the FBGs that describes the Bragg wavelength shift versus temperature. Higher temperature tests were performed in the Fibheat 200 and compared to the models obtained from the oil bath later in this Chapter.

6.3.1 The Single FBG Fibre Characterization

The optical fibre with a single FBG and a design Bragg wavelength at 1550 nm (refer to Figure 6.2) is connected to the circulator. From this point forward the single FBG in the optical fibre will be referred to as FBG1. The Bragg wavelength shift of a FBG with temperature will practically be demonstrated and measured in this Section. The environmental conditions recorded when the measurements were performed are summarized in table 6.1.

The measured reflection profile of FBG1 at room temperature is illustrated in Figure 6.9. The exact manufacturing parameters of FBG1 could not be provided by the manufacturer, AOS GmbH. It was therefore decided to es-

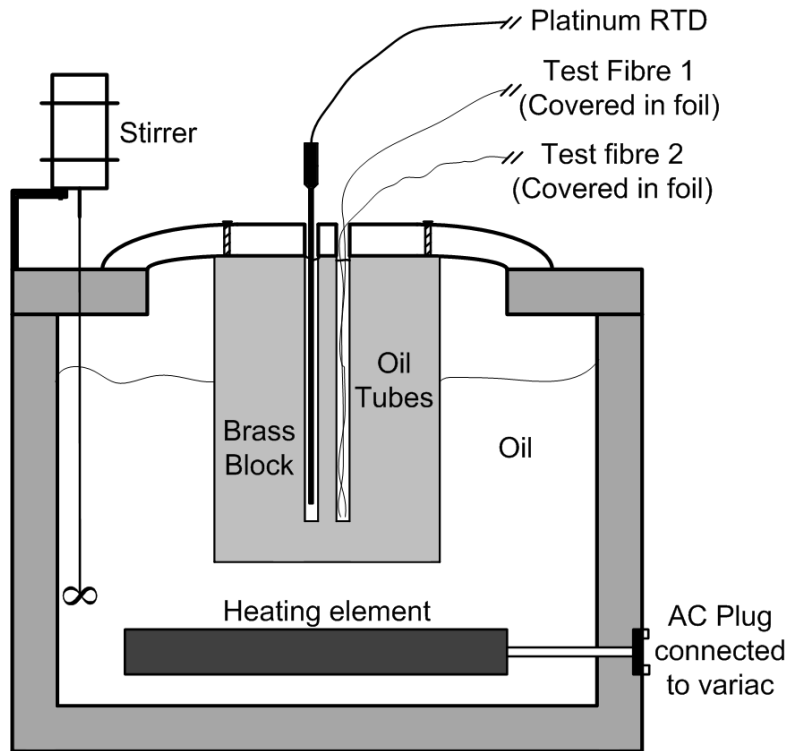


Figure 6.8: A diagram illustrating the positioning of the platinum RTD and optical fibres within the oil bath. The brass block and oil surrounding it ensures that the RTD and optical fibres are at the same temperature.

Environmental Parameter	Value
Temperature	23.57°C
Atmospheric Pressure	1008 hPa
Humidity	49%

Table 6.1: Environmental conditions recorded when FBG1 was interrogated on the 9th of November 2008.

estimate the manufacturing parameters by trial and error. The parameters were verified by comparing the simulated reflection spectrum to the measured reflection spectrum. In Table 6.2 the manufacturing parameters is provided of a simulated FBG that matches the measured reflection spectrum of FBG1 the closest; the reflection spectrum of the simulated FBG is illustrated in Figure 6.9.

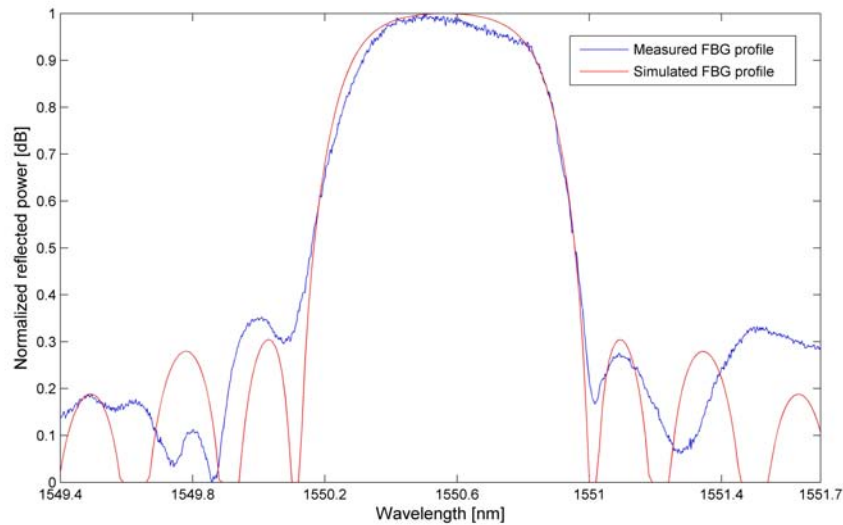


Figure 6.9: Illustrating the measured reflection spectrum of FBG1 at 25.64°C. The simulated reflection profile of a FBG whose parameters were adjusted to best fit the measured FBG is illustrated in red.

Design Parameter	Value
Length	2.75 mm
Λ	529.415 nm
δn_{eff}	4.1×10^{-4}
n_{eff}	1.464
Gaussian Apodization Constant	5

Table 6.2: The manufacturing values that was found through simulation to best represent the reflection profile of FBG1.

It becomes a difficult task to accurately and consistently determine the Bragg wavelength of each FBG reflection profile. It was found that correlating the simulated FBG that best represents the FBG (of which the Bragg

wavelength is known) to the measured data provides a consistent and accurate method to determine the Bragg wavelength. The correlation method was implemented in Matlab. Equation 6.3.1 is then used to relate the correlation peak back to the position of the Bragg wavelength of the measured data.

$$\text{FBG}_{\text{Centre}} = \text{Corr}_{\text{Peak}} - (N - 1) + \text{Reference}_{\text{Max}} \quad (6.3.1)$$

The variable $\text{Corr}_{\text{Peak}}$ is defined as the sample number where the maximum value of the correlation data occurs, N is the length of the measured data matrix or the simulated FBG matrix (whichever one is the largest) and $\text{Reference}_{\text{Max}}$ is the sample number at which the Bragg wavelength occurs of the simulated FBG. When the simulated FBG illustrated in Figure 6.9 is correlated with the measured data in the same figure the curve in Figure 6.10 is obtained. It becomes a simple task of relating the sample number where the maximum value of the correlated data occurs back to the measured data through Equation 6.3.1 to determine the Bragg wavelength.

Figure 6.11 illustrates the measured reflection profiles for the FBG at temperatures 25.64°C, 62.36°C and 103.08°C which will be correlated with their models to determine the exact centre reflection wavelengths.

Using the data in Figure 6.11 a model that provides the wavelength shift versus temperature for the FBG can be deduced. The Bragg wavelengths of FBG1 at the different temperatures were determined with the correlation technique and plotted in Figure 6.3.2. According to Andreas and Kyriacos [2] the temperature sensitivity of a typical FBG in silica fibre is approximately 10 pm/°C. This corresponds very well to the 10.6 pm/°C obtained in this experiment. The Bragg wavelengths at the three temperatures can be represented by a linear equation with the form:

$$\Delta\lambda(T)_{\text{FBG1}} = 1550.28133 + 0.0108748 \times T \quad (6.3.2)$$

Temperature measurement with a single FBG was successful. Over the $\pm 100^\circ\text{C}$ temperature change, the corresponding Bragg wavelength shift was extremely linear in accordance with the literature [2].

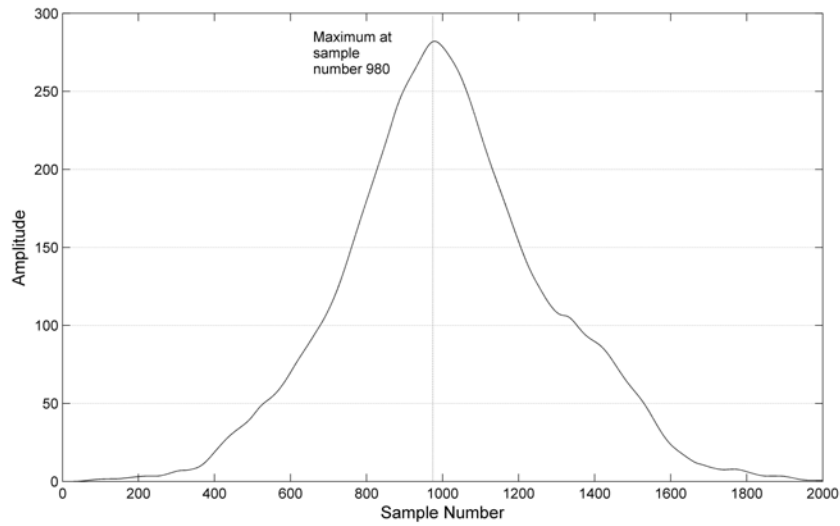


Figure 6.10: The result obtained when the simulated FBG and the measured reflection spectrum is correlated. From this figure it is possible to accurately calculate the Bragg wavelength of the FBG.

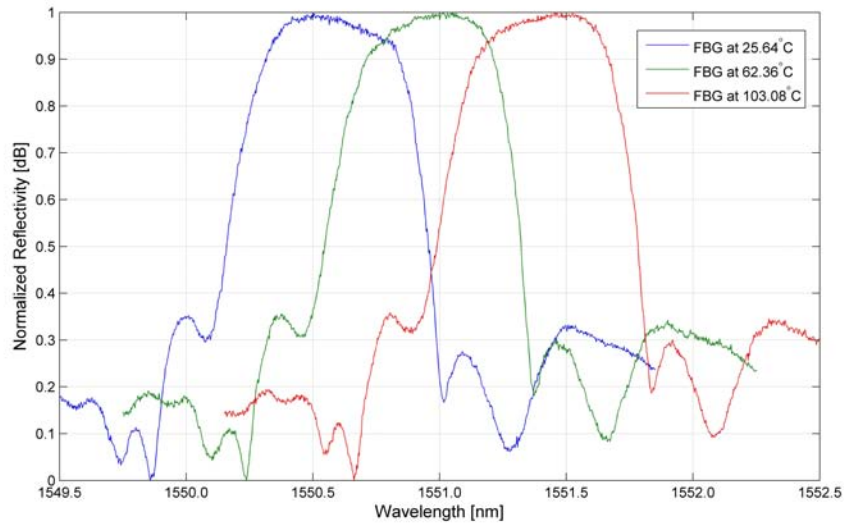


Figure 6.11: The reflection profiles of FBG1 at 25.64°C, 62.36°C and 103.08°C.

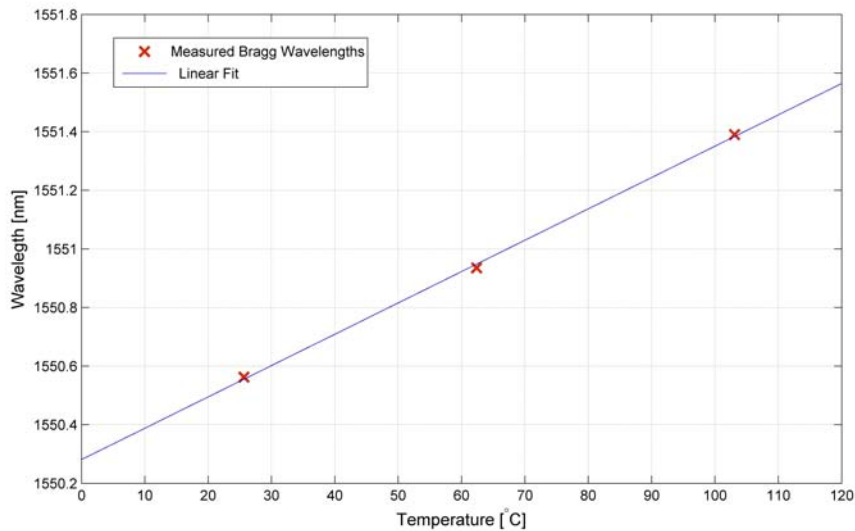


Figure 6.12: Illustrating the measured change in wavelength versus temperature for FBG1 together with Equation 6.3.2.

Environmental Parameter	Value
Temperature	25.8°C
Atmospheric Pressure	1010 hPa
Humidity	53%

Table 6.3: Environmental conditions recorded when the optical fibre with multiple FBGs were analyzed on the 11th of November 2008.

6.3.2 The Multiple FBG Fibre Characterization

The second fibre is now connected to the circulator which has three FBGs inscribed with design Bragg wavelengths at 1480 nm, 1530 nm and 1550 nm respectively. Temperature measurement using WDM of FBGs will be demonstrated in this Section. Henceforth the FBGs in the second fibre will be referred to as FBG2, FBG3 and FBG4 respectively; please refer to Figures 6.2 and 6.13 for the physical and wavelength placement of these FBGs. The environmental conditions recorded when the measurements were performed are summarized in Table 6.3.

The reflection profiles measured with the HRS of FBG2, 3 and 4 at room temperature is illustrated in Figure 6.13. Note that the structure of each individual FBG differ significantly. The difference in the amount of energy reflected by each FBG can be attributed to the differences in manufacturing

parameters as well as the variation in the attenuation of the circulator for a given wavelength.

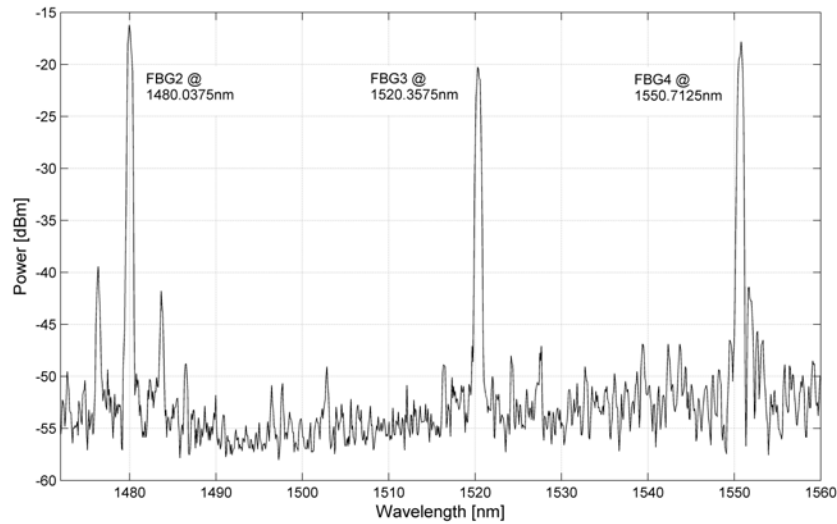


Figure 6.13: Illustrating the reflection spectrum of the multiple FBG fibre. The three FBGs are clearly visible and marked accordingly.

Mathematical models that best represent FBG2, 3 and 4 were estimated through simulation as with FBG1. The parameters of the models are listed in Table 6.4 and the results are illustrated in Figure 6.14. In Figure 6.14 (d) the correlation of the simulated and measured data is illustrated, a clear peak is easily distinguishable and can again be used with Equation 6.3.1 to determine the Bragg frequencies of the FBGs.

The multiple FBG fibre was then, like the single FBG fibre, placed in the oil bath and the reflection profiles recorded at 25.64°C, 62.36°C and 103.08°C.

Design Parameter	FBG2	FBG3	FBG4
Length	3.1 mm	3.15 mm	2.75 mm
Λ	505.34 nm	519.07 nm	529.46 nm
δn_{eff}	4	4.7	4.1
n_{eff}	1.464	1.464	1.464
Gaussian Apodization Constant	7	8	7

Table 6.4: The estimated manufacturing parameters of FBG2, 3 and 4.

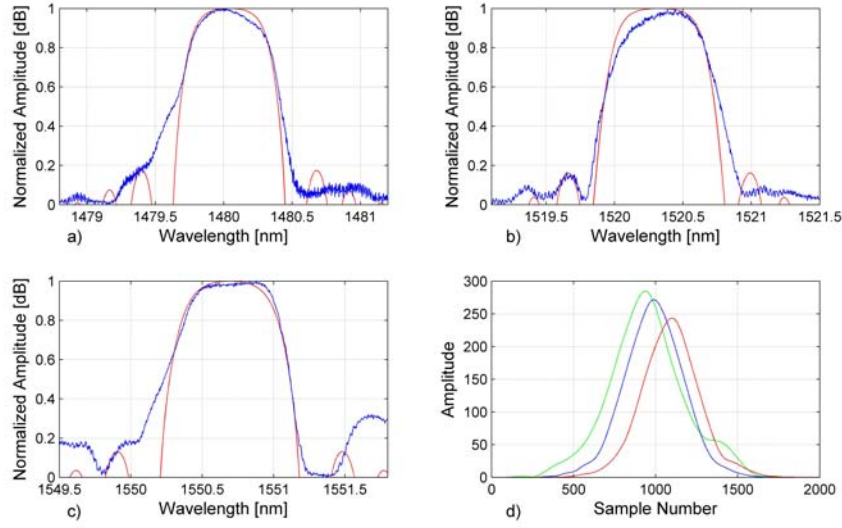


Figure 6.14: The simulation results for each of the FBGs in the multiple FBG fibre is compared to the measured data. In subfigures (a) to (c) the simulation results as well as the measured data is presented in red and blue respectively. Subfigure (d) illustrates the correlation result of FBG2 (red), FBG3 (blue) and FBG4 (green) with their simulation result.

The correlation technique was used to determine the Bragg frequencies at the mentioned temperatures and linear equations was fit tot the data as illustrated in Figure 6.15. The equations that describe the respective wavelength shifts versus temperature for the FBGs is given in Equation 6.3.3 to 6.3.5.

$$\Delta\lambda(T)_{\text{FBG2}} = 1479.7887 + 0.0096885 \times T \quad (6.3.3)$$

$$\Delta\lambda(T)_{\text{FBG3}} = 1520.0769 + 0.0103063 \times T \quad (6.3.4)$$

$$\Delta\lambda(T)_{\text{FBG4}} = 1550.4144 + 0.0107282 \times T \quad (6.3.5)$$

The Bragg wavelengths' sensitivity to temperature seems to change with an increase in temperature as seen in Equations 6.3.3 to 6.3.5. This observation is confirmed with Equation 6.3.6 [44].

$$\Delta\lambda(T)_B = \lambda_B(\alpha_\Lambda + \alpha_n)\Delta T \quad (6.3.6)$$

In Equation 6.3.6 α_Λ and α_n is the thermal expansion coefficient and thermo-

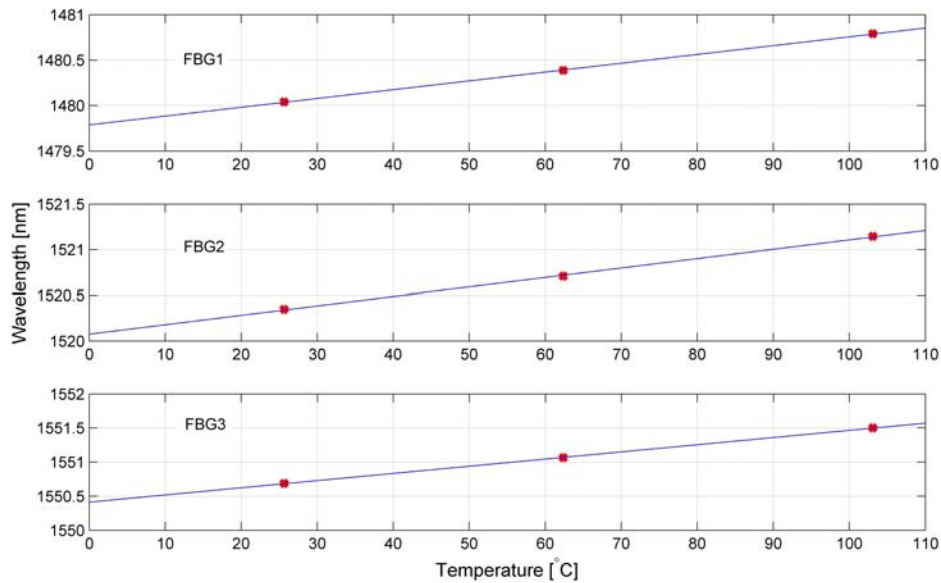


Figure 6.15: Illustrating the Bragg frequency shift of the FBGs with temperature. The measured Bragg frequencies are in red whereas the blue lines represent the linear Equations 6.3.3 to 6.3.5.

optic coefficient, respectively. The temperature sensitivity of a FBG is according to Equation 6.3.6 dependent on the Bragg wavelength of the FBG. With large differences in inscription wavelength this dependency becomes evident as seen in Equations 6.3.3 to 6.3.5. The Bragg wavelength change versus temperature however, is over such a small wavelength range that the corresponding relationship remains linear. Using Equation 6.3.6 together with Equations 6.3.3 to 6.3.5 the sum of α_{Λ} and α_n is calculated as $\pm 6.7 \times 10^{-6}$ for the fibres used in this project.

Temperature measurement with WDM of FBGs were successfully performed. When the FBGs are uniquely distinguishable within the wavelength domain it becomes just as simple to perform temperature measurements with multiple FBGs as it is with only a single FBG.

6.4 Measurements in the Fibheat 200

The operation of FBGs at higher temperatures will now be demonstrated in the Fibheat 200 fibre heating element. A J-type thermocouple (accuracy $\pm 1^\circ\text{C}$) is inserted along with the optical fibre in order to validate the mea-

sured temperature by the FBG. The environmental parameters when the tests in this Section was performed is presented in Table 6.5. Figure 6.16 illustrates the optical fibre and thermocouple in the Fibheat 200. An effort was made to ensure that the FBG is centered in the heating element.

Environmental Parameter	Value
Temperature	24.3°C
Atmospheric Pressure	1011 hPa
Humidity	54%

Table 6.5: Environmental conditions recorded when FBG1 was inserted in the Fibheat 200 heating element on the 14th of November 2008.

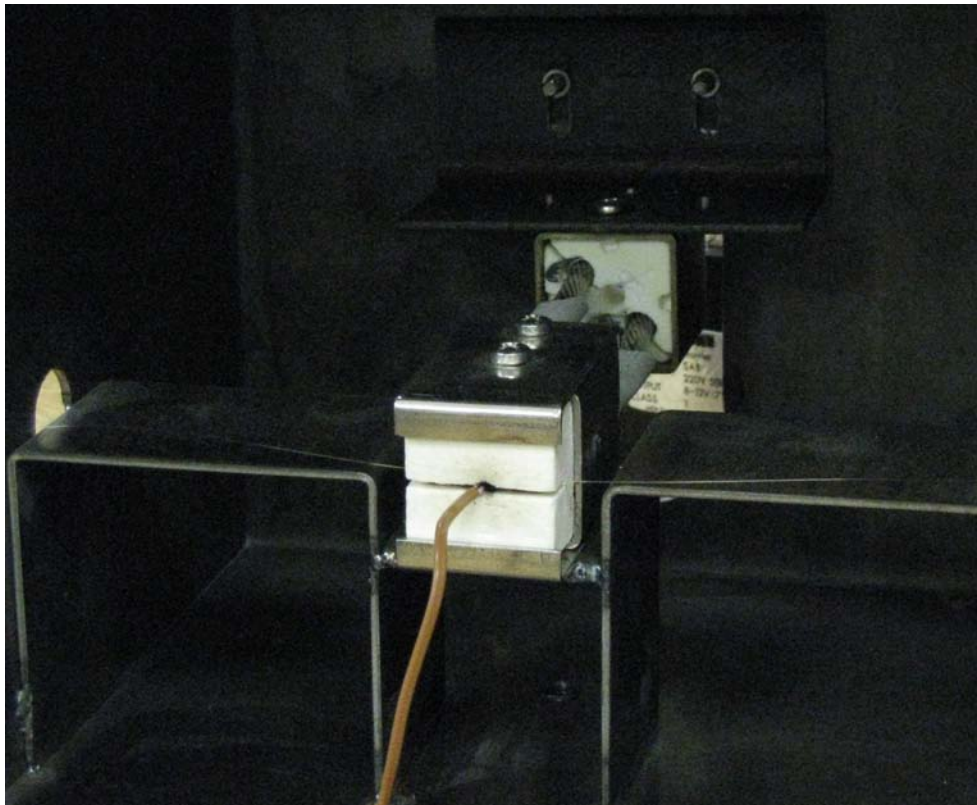


Figure 6.16: An illustration of the optical fibre inserted in the Fibheat 200. Note the J-type thermocouple in the front that is used to measure the heater temperature.

An interesting change in the reflection profile of FBG1 was noticed when the temperature in the Fibheat 200 reached 160°C. The reflection profile of

FBG1 seemed to widen with an increase in temperature as illustrated in Figure 6.17. Spectral widening of an FBG is not normally associated with an increase in temperature. It was then suspected that a strong temperature gradient across the FBG might be the cause of the spectral widening.

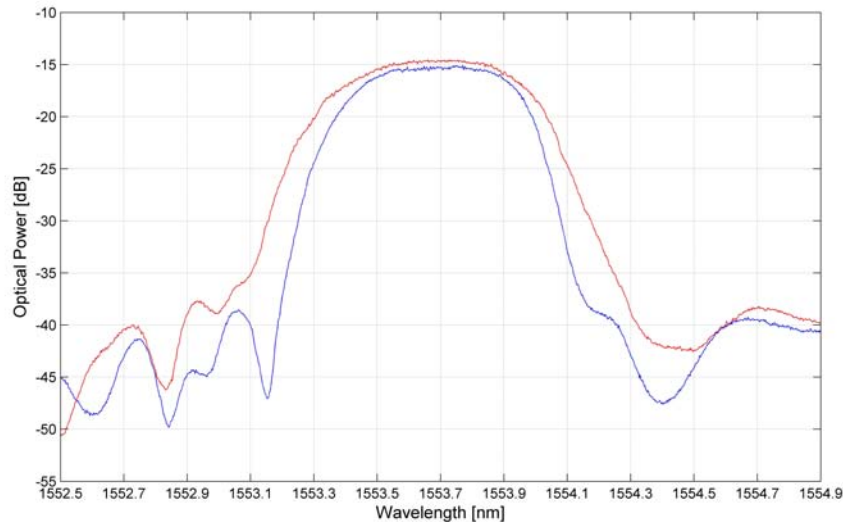


Figure 6.17: Illustrating the spectral widening of the FBG reflection profile when the temperature reached 160°C in the Fibheat 200. Please note that the curve in red is FBG1 at 160°C whereas the blue curve was superimposed on the image to provide a visual illustration of the spectral widening.

A blackbody sensor system developed by Darren Crosse was used to obtain a thermal image of the Fibheat 200 and verify the suspected temperature gradient across the FBG. A thermal image of the Fibheat 200 at roughly 160°C is provided in Figure 6.18; the outlines of the heating element is superimposed on the image. From the thermal image, differences of up to 80°C is observed between the centre of the heater and the sides. This is an unacceptable temperature gradient that has to be minimized as far as possible.

Another difficulty that was ran into is that the temperature measured by the thermocouple depends heavily on the position thereof in the Fibheat 200. This is also due to the temperature gradient in the heater which resulted in large differences between the temperature measured by the FBG and the thermocouple.

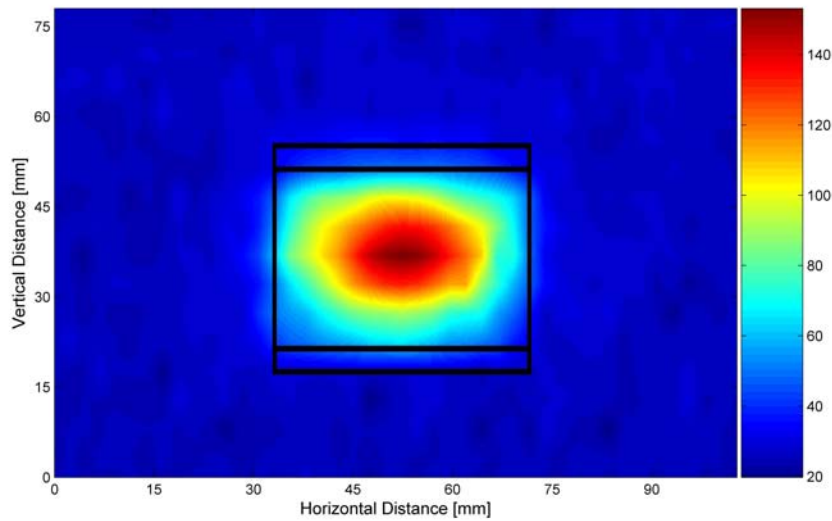


Figure 6.18: The blackbody radiation emitted from the Fibheat 200 produced the image and illustrates the temperature gradient present across the length of the inserted fibre.

It was then decided to cover the thermocouple and FBG with foil in an attempt to evenly distribute the heat across the FBG. The thermocouple would also be in direct contact with the FBG and the foil, which means a more stable and accurate temperature reference. An illustration of how the FBG and thermocouple is covered in foil is presented in Figure 6.19.

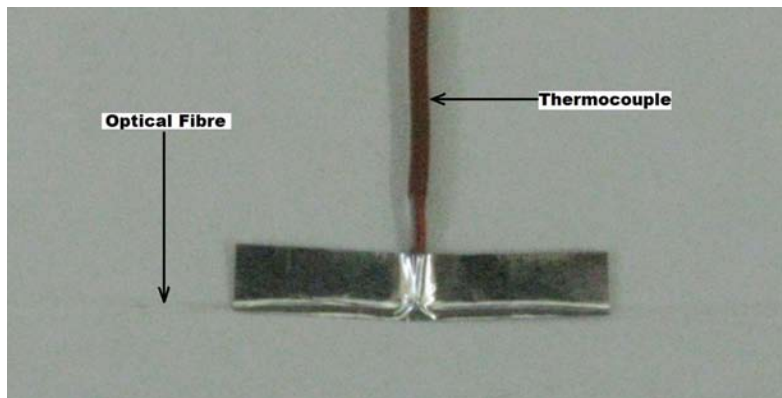


Figure 6.19: The FBG and thermocouple is covered in foil to prevent a large temperature gradient across the optical fibre and to ensure that the correct temperature is measured by the thermocouple.

The foil cover performed excellent in its task to evenly distribute the temperature across the FBG and thermocouple. Even at heater temperatures above 250°C the spectral response of FBG1 remained the same (except for the Bragg wavelength shift), no spectral widening of the FBG reflection profile was observed. Up to the 100°C thermocouple and FBG measured the same temperature, beyond 100°C small differences became evident.

A transfer curve that represents the temperature measured in the Fibheat 200 heating element versus the measured Bragg wavelength of FBG1 is presented in Figure 6.20. Once again the Bragg wavelength shift versus temperature is linear even over this large temperature span. A linear equation was fit to the measured data and the result is presented in Equation 6.4.1.

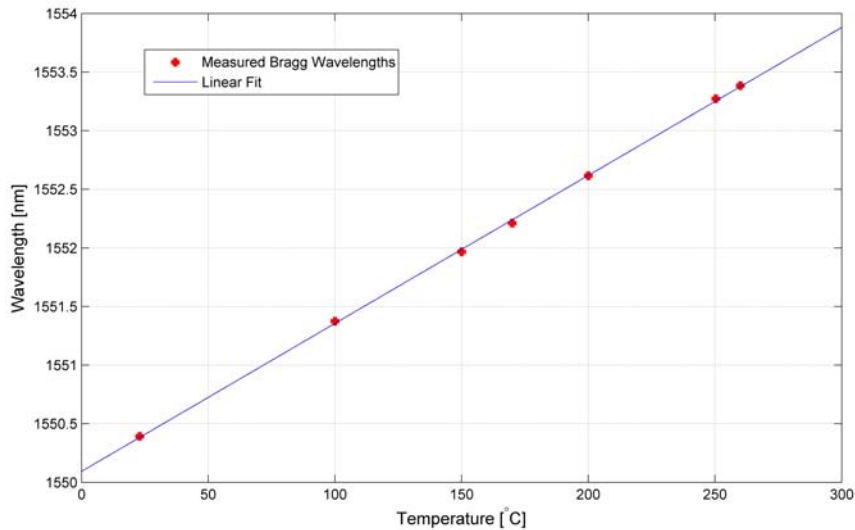


Figure 6.20: The Bragg wavelength shift of FBG1 versus temperature in the Fibheat 200 heating element.

$$\Delta\lambda(T)_{\text{FBG1}} = 1550.27422 + 0.0110733 \times T \quad (6.4.1)$$

There are slight differences between the transfer curve obtained for FBG1 in the oil bath and in the Fibheat 200. The environmental conditions recorded when these separate tests were conducted are almost identical and cannot be the cause. A maximum difference of 4.5°C is observed between the model in

Equation 6.4.1 and 6.3.2 when the heater is operating at 260°C. This difference can be attributed to thermocouple inaccuracies as well as small temperature differences still present between the FBG and thermocouple despite the foil cover. This error seems to increase with temperature due to an increasing temperature gradient in the heater.

FBGs written in silica fibres are perfectly suited to temperature measurement up to 260°C as demonstrated in this Section. The FBG was not tested beyond 260°C in fear of damaging/erasing the FBG.

6.4.1 Temperature Measurement Repeatability

The repeatability of the measurements with the HRS is unknown. In an attempt to determine the variability in the FBG peak detection method, 60 measured reflection spectrums at a constant temperature were collected from FBG1 and correlated with its simulated FBG. A sample number of 60 will ensure an error of less than 20% in estimating the standard deviation. The measured data were collected over a 6 hour period of time and FBG1 was held at a constant temperature of $25.64 \pm 0.015^\circ\text{C}$. This is hardly enough data for a proper statistical analysis but will suffice as an indication of the temperature measurement repeatability over a short period of time.

The uncertainty in the FBG peak can mathematically be expressed as a normal distribution with a standard deviation $\sigma = 6.54$ pm. Note that it is assumed that the mean wavelength error have been mitigated through calibration. The data gathered in the test is illustrated in Figure 6.21 together with the normal distribution that was fit to the measured data.

A standard deviation of 6.45 pm relates to a temperature measurement uncertainty of $\pm 0.6^\circ\text{C}$; which is true when the temperature sensitivity of the FBG is ± 10 pm/ $^\circ\text{C}$. The reason for this measurement error is mainly due to the shortcomings in power and wavelength accuracy of the HRS. According to the HRS specifications sheet the power and wavelength accuracy is ± 2.75 dB and ± 15 pm respectively. A large part of this error have been mitigated through calibration, if the FBG is not calibrated temperature measurement errors as large as $\pm 1.5^\circ\text{C}$ can be expected. This does not include the added peak detection error caused by the power measurement inaccuracies of the HRS.

To summarize, without calibration a temperature measurement error of $\pm 1.5^\circ\text{C}$ or larger is expected. Calibration on the other hand can reduce this

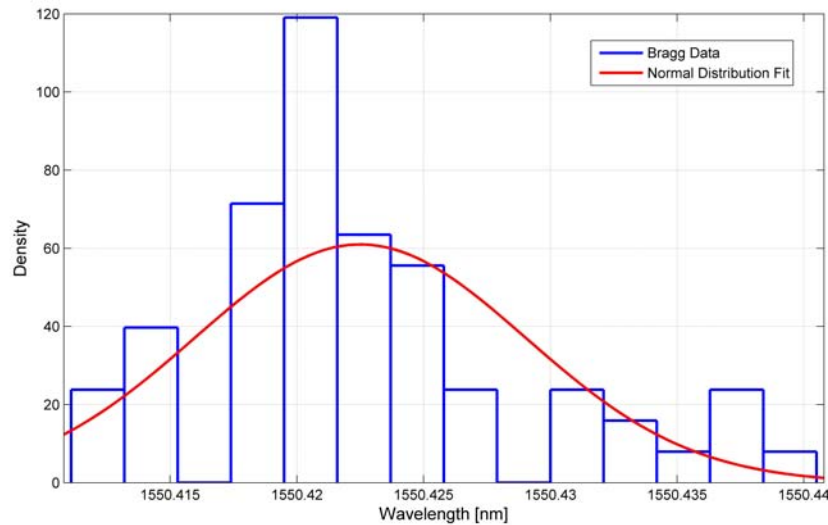


Figure 6.21: Illustrating the distribution of the detected Bragg frequency even though the temperature of the FBG is held constant.

temperature measurement error significantly; the repeatability of the measurement can then be represented by a normal distribution with a standard deviation of $\pm 0.6^{\circ}\text{C}$.

6.4.2 Reflection Profile Stability

Changes in the shape of the reflection profile of the FBG will result in peak detection errors since the correlation technique used relies on the fact that the relative shape of the reflection profile remains the same as the model with which it is correlated.

Figure 6.22 is a comparison between the average reflection profile before and after the temperature tests were performed in this project. The blue curve represents the average of 10 measurements at the start of the project whereas the red curve represents the average of 10 measurements at the end of the project.

The reflection profile of FBG1 were also compared to the original reflection spectrum when heated to 103.08°C in the oil bath. Although the Bragg wavelength changed, the reflection profile remained the same with no evident change. During the course of this project no noticeable degradation of the reflection profile was observed. No hysteresis were detected either.

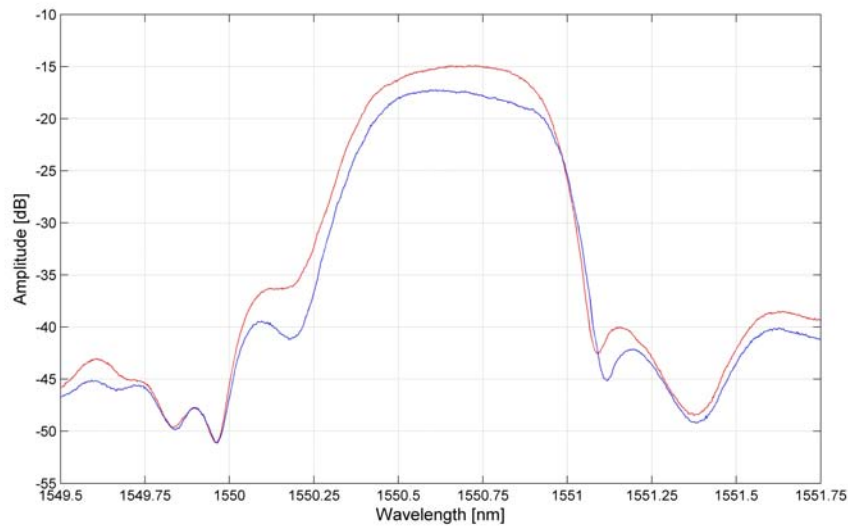


Figure 6.22: The average reflection profile of the FBG1 before any temperature tests were performed is illustrated in blue. An average reflection profile of the same FBG after several temperature cycles were performed is provided in red.

6.5 Interpretation of Results

Temperature sensing using silica FBGs were demonstrated in this Chapter. Two silica optical fibres were interrogated; one with a single FBG and the other with three FBGs inscribed. In both cases models for the FBGs were developed based on practical temperature measurements within an oil bath. The Bragg wavelength shift versus temperature relationship obtained for the FBGs corresponds very well with the literature [2]. An increase in temperature sensitivity was noted with an increase in wavelength, which is also consistent with the literature.

It was illustrated that a temperature increase produces a remarkably linear increase in the Bragg wavelength of the FBG without affecting the shape of the reflection profile. This holds true as long as a temperature gradient is not present over the FBG. A strong temperature gradient was created over the FBG when initially inserted into the Fibheat 200 heating element. The result was an increase in the spectral width of the FBG, which is undesirable with WDM FBG temperature sensor systems. Covering the optical fibre in foil decreased the temperature gradient across the FBG that a measurable increase in spectral width was no longer apparent. The Fibheat 200 was thereafter

successfully used to heat the FBG, resulting in a Bragg wavelength versus temperature curve corresponding to that obtained in the oil bath.

A very consistent and accurate method was developed to determine the Bragg frequency of the FBG. The only assumption being that the reflection profile does not change form. First a model that represents the reflection profile of the FBG is obtained. This model is then correlated with the measured reflection spectrum which has been normalized to eliminate the effects of attenuation. The correlated result is then used to determine the Bragg wavelength of the FBG as discussed in this Chapter.

Without calibration, temperature measurement errors with the Agilent HRS when interrogating FBGs can be as large as $\pm 1.5^{\circ}\text{C}$. With calibration it was found that this error can be reduced significantly; a normal distribution with a standard deviation of $\pm 0.6^{\circ}\text{C}$ is used to represent the measurement error. No hysteresis or degradation of the reflection profile was noted through the course of this project.

Chapter 7

Temperature Sensing in the PBMR Using FBGs

Several key challenges in implementing an FBG temperature sensing system in the PBMR core are theoretically investigated in this Chapter. This Chapter builds on the theoretical and practical knowledge gained in the previous Chapters, with the goal of applying this knowledge specifically to the PBMR.

Radiation and the high operating temperature present in the PBMR core demands drastic changes in conventional FBG sensing systems. Some of the changes include the fibre type, interrogation methods and the way in which the temperature data is extracted, which is discussed in this Chapter.

7.1 Equipment Selection and Design

Radiation environments call for specialized fibre and different, more robust ways of interrogation. In this Section, the required fibre and equipment for successful temperature measurement is theoretically investigated.

7.1.1 Sapphire FBGs

The only waveguide currently available that can possibly survive the harsh environment within the PBMR is sapphire optical fibre. A summary of why sapphire fibre is considered as a viable solution is presented by discussing its performance in the environmental challenges that the PBMR presents.

7.1.1.1 Temperature

The melting point of pure sapphire is 2050°C, which is well beyond the temperature that the PBMR core will reach in the event of a total loss of coolant.

Ultra-high temperature sensing sapphire FBGs operating at up to 1530°C have been demonstrated by Grobnic et al. [24]. In the tests conducted by Grobnic et al. [24], no obvious reduction in the reflected spectrum was observed, nor was any spectral distortion or variation measured. No hysteresis were detected when the temperature was repeatedly cycled between room temperature and 1530°C. Overall, sapphire FBGs seems more than capable of accurate high temperature measurement.

An undesirable effect that an increase in temperature has on the fibre is the fact that the fibre becomes longer at high temperatures. If the fibre is not fixed at the points where the measurements are to be made, these measuring positions will change with temperature. The coefficient of linear expansion for the optical fibre can be calculated and compensated for using Figure 4.9 to determine α_n and integrating over the temperature span to determine the change in length as illustrated in Equation 7.1.1:

$$\frac{\Delta L}{L} = \int_{T_0}^T \alpha_{n(T)} \Delta T dT \quad (7.1.1)$$

7.1.1.2 Radiation

The information available in the literature regarding radiation testing on sapphire fibres have been discussed in detail in Section 3.5. Research conducted on sapphire fibre has shown that sapphire fibres are suitable for data transmission over the wavelength band of 1400 to 1600 nm where the effects of RIA, RL, natural attenuation and dispersion are at a minimum. Information regarding the performance of sapphire fibre under high-radiation, -pressure and -temperature levels combined is not available in the literature to the best knowledge of the author.

It is predicted that FBGs written into sapphire fibre will not be severely affected by radiation based on the fact that sapphire fibres have been found to be relatively radiation-resistant [63]. A critical parameter yet to be determined is the influence of intense ionizing radiation on the effective index change of sapphire under high temperature. It is critical that the long-term

effects of radiation on FBGs in sapphire fibre at high temperatures and pressures are investigated.

7.1.1.3 Pressure

Pressure within the PBMR containment vessel will reach a maximum of 9 MPa during operation. The compression strength of sapphire is 2 GPa which means that the sapphire optical fibre will have no problem surviving the pressurized core. Sapphire will, however, elongate due to the increase in pressure which will in turn affect the Bragg wavelength of the FBG as well as the position where the temperature is monitored.

Sapphire has a Young's Modulus of around $E = 345$ GPa (Roditi sapphire fibre) depending on the manufacturer, and the change in length of the sapphire fibre at a uniform pressure is calculated as follows:

$$\frac{\Delta L}{L} = -\frac{(1 - 2\nu) P}{E} \quad (7.1.2)$$

where the variable ν is the Poisson's ratio, L is the fibre length and P is the applied pressure. The Poisson's ratio for sapphire is anisotropic and varies between $\nu = 1.8$ to $\nu = 0.29$. We will assume that for the purposes of this project $\nu = 1$. This means that for every metre of sapphire fibre, the fibre will elongate 5.8 μm when a pressure of 9 MPa is applied. Due to the small diameter of the sapphire fibre, the change in diameter is negligible.

An increase in pressure decreases the effective refractive index of the fibre, thereby changing the Bragg wavelength of the FBG. This can, however, be compensated for using Equation 7.1.3 when the pressure is known [2].

$$\frac{\Delta n}{n} = \frac{n^2 P}{2E} (1 - 2\nu) (2p_{12} + p_{11}) \quad (7.1.3)$$

The constants p_{12} and p_{11} are strain-optic constants that have to be calibrated with every specific fibre used. The change in length of the fibre can be calculated by Equation 7.1.2 and the Bragg wavelength sensitivity of a sapphire FBG is calculated by combining Equations 7.1.2 and 7.1.3, resulting in the following wavelength-pressure relation:

$$\frac{\Delta\lambda_P}{\Delta P} = \lambda_B \left[\frac{(1-2\nu)}{E} + \frac{n^2}{2E} (1-2\nu) (2p_{12} + p_{11}) \right] \quad (7.1.4)$$

Calibration of a type of sapphire fibre is a necessity due to the variations in manufacturing techniques and quality of sapphire produced. Once the strain-optic constants of a sapphire fibre have been determined, it becomes a matter of adjusting the measured Bragg wavelength to produce accurate temperature measurements even in high-pressure environments such as the PBMR.

7.1.1.4 Combined Effects of Temperature, Pressure and Radiation

In the PBMR, an FBG sensor will be subjected to an extreme combination of pressure, temperature and radiation. Whether the interaction of these environmental conditions with the sapphire FBG will result in a severely shortened life span or even rapid sensor failure is unknown.

A systematic approach is required to determine the temperature using FBGs in the PBMR. The interaction between temperature, pressure and radiation has to be known before the Bragg wavelength, λ_B , can be correctly interpreted, as illustrated by Figure 7.1. The variables, C_{x-y} , model the interaction between the environmental effects on the change in Bragg wavelength where the x and y can be either pressure (P), temperature (T), or radiation (R). Once the effect of radiation and the interaction variables are known, a correction algorithm can be written in order to determine the temperature of the FBG.

7.1.1.5 FBG Design

Each of the FBGs in the distributed temperature sensing system has to be designed using a holistic approach. The reason is that the length of the FBG has to be chosen while considering the thermodynamics of the core as well as the bandwidth and constraints imposed due to RL.

The main FBG parameters that can be chosen and manipulated within boundaries during the manufacturing process is the length, change in refractive index and the period of the FBG. First of all, the length of the grating has

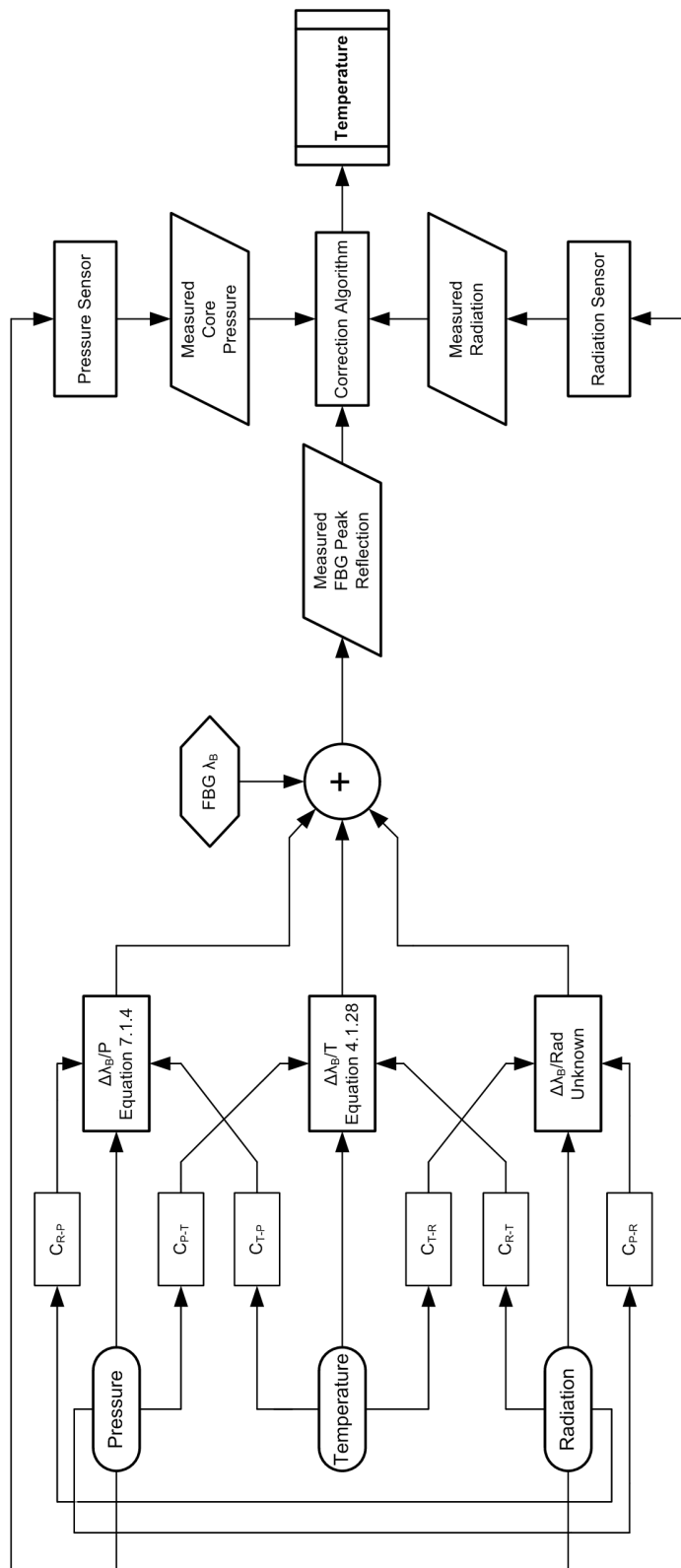


Figure 7.1: Illustrating the interaction between and effect of temperature, pressure and radiation on the Bragg wavelength of the FBG and how a correction algorithm would be implemented.

System Variable	Effect
Thermodynamics	A long FBG will result in poor thermal resolution. The length over which the temperature measurement is made will become longer and averaged over the FBG length. The longer the FBG the larger the chance of a strong temperature gradient forming across the FBG which will influence the reflection spectrum.
Bandwidth	The longer the FBG the more profound the side lobes become. This will result in an increased wavelength separation parameter required and ultimately more bandwidth required to make the same amount of temperature measurements. A shorter FBG on the other hand will broaden its spectral response again resulting in more bandwidth occupied per FBG.
SNR	If the FBG is too short, the reflectivity of the FBG will decrease, resulting in a poor SNR.

Table 7.1: The effects that the length of an FBG has on the temperature sensing system as a whole.

a profound effect on several parameters. Table 7.1 discusses how the length of the FBG influences the SNR and available bandwidth.

The FBG length clearly needs to be as short as possible to ensure excellent measurement resolution which is critical if fuel sphere movement is to be detected. The FBG length can, however, not be shortened indefinitely since the FBG reflectivity is directly dependent upon the grating length. The induced refractive index change, on the other hand, can be increased to compensate for this decrease in reflectivity up to a point. The maximum induced refractive index change is set by manufacturing limitations which are unknown at this stage. The FBG should therefore be designed with the maximum possible change in refractive index (without resulting in unwanted effects) as well as the shortest possible FBG while ensuring that the reflected power remains in the order of 99%. The effect of various FBG lengths can be determined once a complete thermodynamic model is available. Figure 7.2 graphically illustrates the influence of the FBG length on the temperature measurement.

The period of the grating is selected depending on its desired location on the wavelength band and must be apodized to ensure that the minimum amount of bandwidth is occupied.

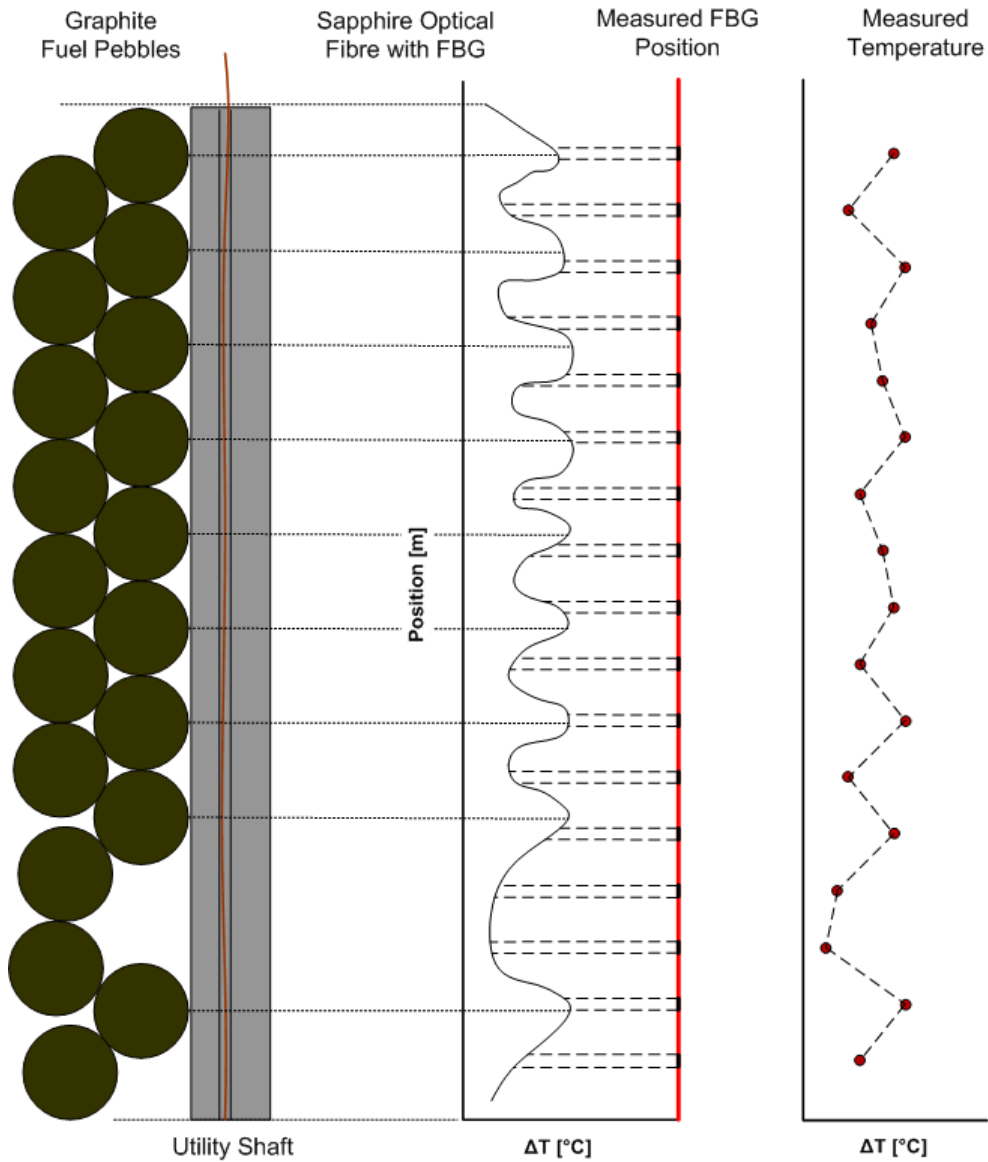


Figure 7.2: Illustrating temperature measurement in the PBMR core and the effect of long FBGs on the measured temperature.

7.1.2 Interrogation Hardware

There exists a myriad of ways to interrogate and demodulate FBG temperature sensors. Rather than listing the most competitive solutions, the author will provide several reasons why the tunable laser source and optical spectrometer combination used as in the research platform is ideal for use in the PBMR. In the PBMR, the challenges a temperature sensor technology faces include the massive amount of temperature sensors required, RL, and RIA. Considering the environmental conditions within the core, Table 7.2 provides a description of why the test equipment specified is well suited as a viable solution.

In Section 4.3, it was highlighted that WDM FBGs are superior in their simplicity, noise performance and accuracy of measurements in the presence of RL and RIA over other multiplexing techniques and will therefore be recommended in this project. The wavelength band available for FBG operation in radiation is from 1400 nm up to 1600 nm (refer to Section 3.5). The limited amount of bandwidth and the immense centre Bragg wavelength shift that FBGs will experience over the temperature range of 25°C to 1600°C necessitates the use of switches in WDM systems. Switches will allow a theoretically infinite number of WDM FBG clusters to be measured, as illustrated by Figure 7.3.

Unfortunately there is a practical limitation to the switching tree described in Figure 7.3. Say, for example, a straight-forward algorithm, one where the whole 200 nm spectrum is swept by the laser, is employed, it would take the 81600B tunable laser source 2.5 s to sweep each fibre segment. Depending on the plant model, it would become rather impractical to measure more than 30 FBG clusters with the same set laser source and OSA as sampling times would exceed one minute. It is therefore critical that intelligent laser sweeping methods and effective use of bandwidth is employed to minimize equipment requirements. Incorporating knowledge regarding the maximum predicted rate of temperature change in the core will assist in the optimum usage of the measurement system.

7.1.3 Multiplexing

Individual FBGs are optimized for operation in a multiplexed system by minimizing their bandwidth requirements through apodization and careful

Challenge	Tunable laser and Optical Spectrometer Combination
<p>RIA results in wavelength-dependent attenuation (colour centres).</p>	<p>The laser power can be adjusted over the sweeping range to account for wavelength-dependent attenuation. Far more power can be injected per wavelength than a broadband source before photobleaching occurs, therefore increasing the SNR and countering RIA. The accuracy and spectral resolution of the 83453B OSA is superb. Together with the input power accuracy, the operator is ensured that all of the information is available and accurate to perform the temperature measurement with any demodulation algorithm.</p>
<p>RL and other noise corrupt the FBG reflection and decrease the SNR.</p>	<p>The per wavelength power injected by the tunable laser is far more than what is possible with a broadband source, without causing photobleaching. This will inevitably result in an increase of the SNR. The noise over the spectrum range can be measured by the OSA and the system 'health' monitored.</p>
<p>The operating bandwidth is immense due to the extravagant temperature range measured.</p>	<p>The Agilent 81600B tunable laser can sweep over the massive 200 nm band with power stability and speed (under 3 s). The Agilent 83453B OSA is capable of measuring the 200 nm bandwidth as the laser sweeps and will provide the information as fast as the laser sweeps.</p>

Table 7.2: How the optical spectrometer and tunable laser source combination are perfectly suited to and will deal with some of the main temperature measurement challenges in the PBMR.

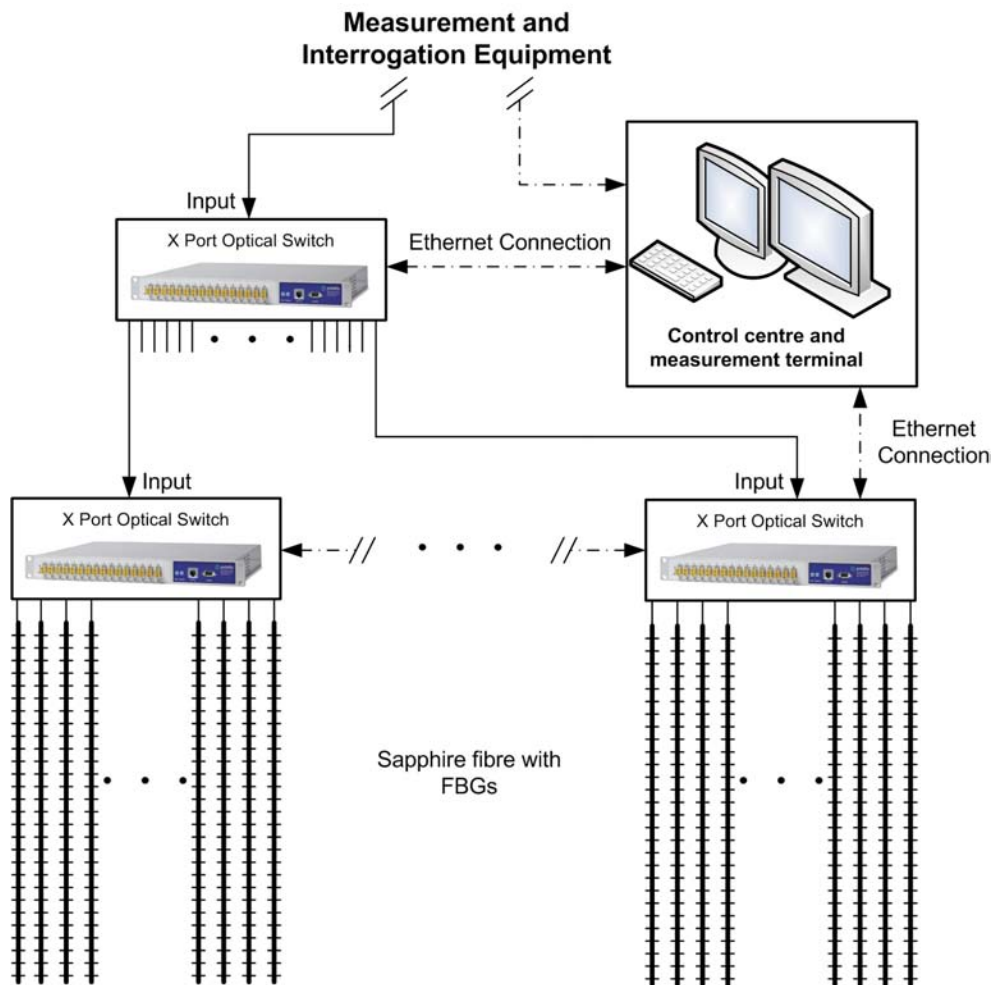


Figure 7.3: Optical switches can be used to extend the measurement capabilities of the optical spectrometer and laser.

selection of the FBG length. On a larger scale, the FBGs on a single sapphire fibre must be chosen such that over the measured temperature range the change in FBG Bragg wavelength does not break the 1400 nm to 1600 nm boundary. At the same time, the wavelength separation between the adjacent FBGs are required to be large enough so that temperature extremes do not cause the FBG reflections to overlap and become indistinguishable.

Dynamic boundaries exist between FBGs to prevent spectral overlapping as discussed in Section 4.5. The safety factor used in the calculation of $\Delta\lambda_{\min}$ can be increased depending on the severity of RL present.

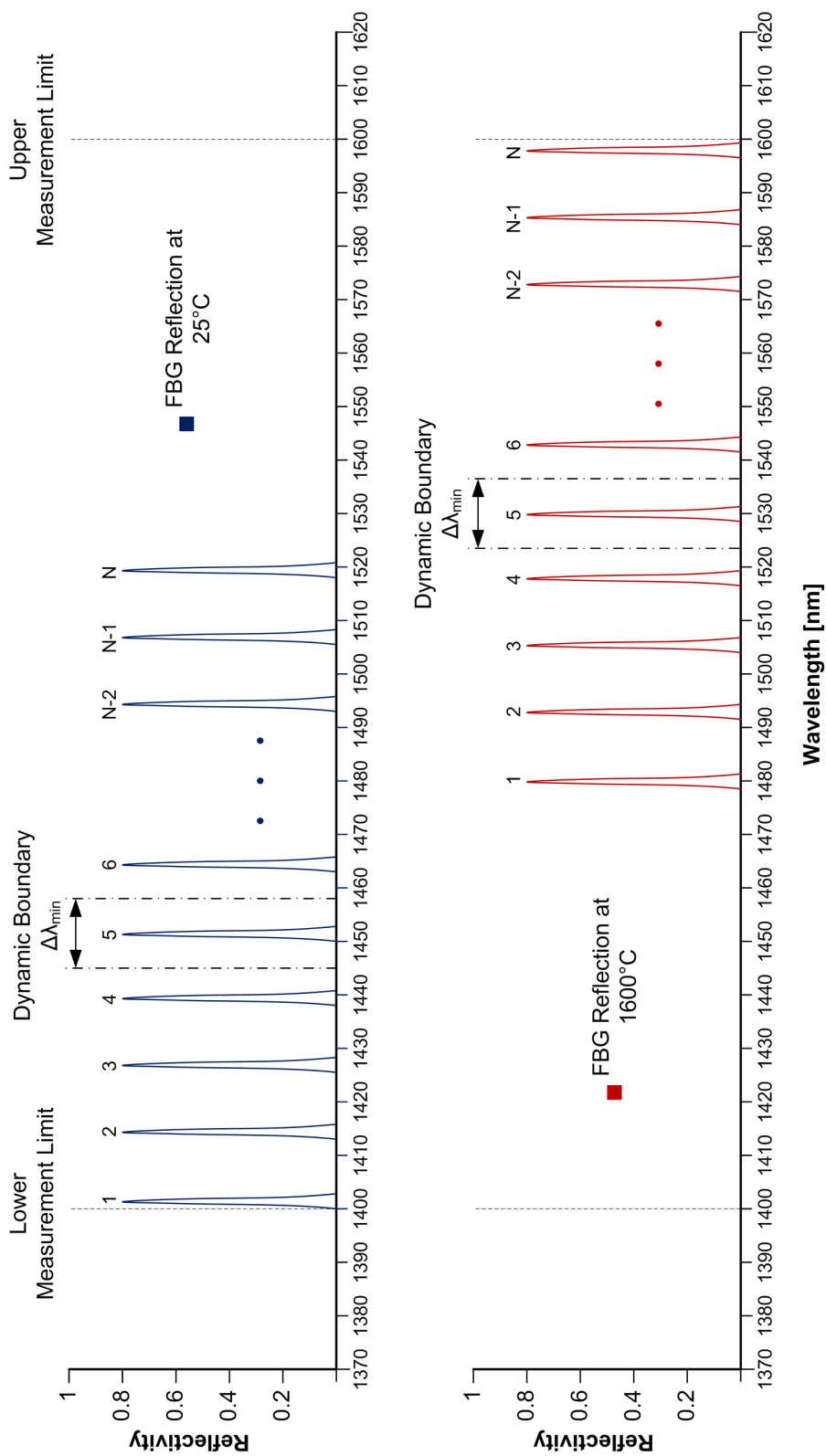


Figure 7.4: The reflection profile of a distributed FBG cluster on a sapphire fibre when at room temperature and at 1600°C.

7.2 FBG Interrogation and Demodulation

The accompanying software of the 83453B HRS does not permit custom sweeping methods and resolutions. If the measurement of distributed FBGs are to be optimized for the PBMR, custom software needs to be written for the HRS measurement system. The custom software must include the following key functionalities:

- Rapidly changing the sweeping speed of the laser is necessary in order to accurately scan certain wavelengths where the reflection peaks of the FBGs are, whereas other areas can be ignored.
- The current software package is only capable of scanning the wavelength band from the shorter to the longer wavelengths. Since it takes time to reset the laser to the shorter wavelengths, it would be more time efficient to sweep from shorter to the longer wavelengths and back again. Wavelength jumping can also increase the time efficiency of the system.
- The software should be able to rapidly execute peak detection algorithms and display the data appropriately. Other valuable information such as noise and attenuation losses must also be measured and displayed.
- Some wavelengths may experience more RIA than others and it will therefore be beneficial to have the ability to increase the laser power output at some wavelengths when performing a sweep.

7.2.1 Demodulation

Accurately detecting the Bragg wavelength of an FBG in the presence of noise and attenuation is critical. Genetic algorithms (GA) have been successfully used to characterize FBGs based on their reflection spectra [60]. Other hardware-specific techniques have also been employed with great peak detection accuracy [57].

The demodulation technique that will be discussed in this thesis is ideally suited for the hardware present and exploits the fact that the reflection profile (not the Bragg wavelength) of the FBG is known beforehand. Consider the WDM FBG system with added Gaussian noise and severe attenuation

presented in Figure 7.5. The Bragg wavelengths cannot be determined accurately by observation alone since a single FBG has several peaks.

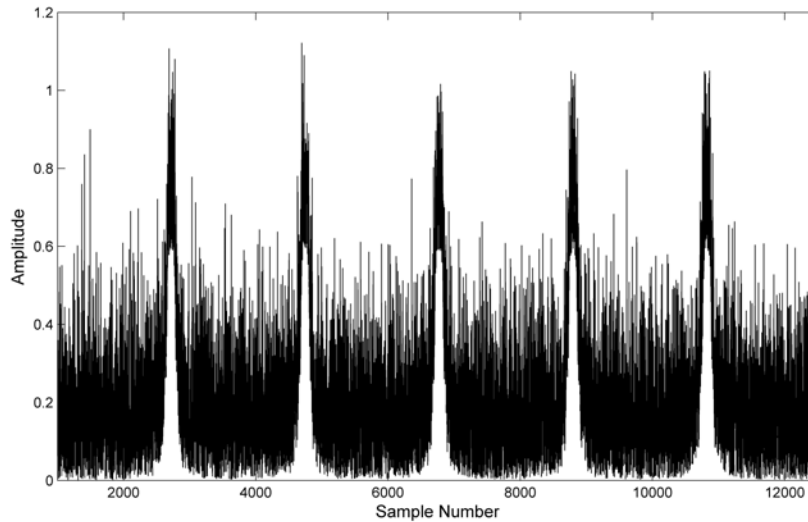


Figure 7.5: Corrupted reflection data of a WDM FBG system. The attenuation is 60% and the noise added is Gaussian in nature with a mean $\mu = 0.06$ and standard deviation $\sigma = 0.2$.

If the original reflection profile of the four identical FBGs is correlated with the data in Figure 7.5, then the data in Figure 7.6 is obtained. From Figure 7.6, however, it becomes a simple task of relating the sample number where a peak occurs back to the wavelength at which it occurred (refer to Chapter 6 for a description of this procedure).

7.2.2 Sensor Health

Ionizing radiation poses the most significant threat to the FBG sensors' long term survivability. As the exposure time to the high levels of mixed radiation increases so will the RIA; ultimately decreasing the SNR until the FBG centre reflection is no longer distinguishable. The situation where the spectral peak identification algorithm exceeds a measurement confidence boundary can then act as a reference for the sensors' health.

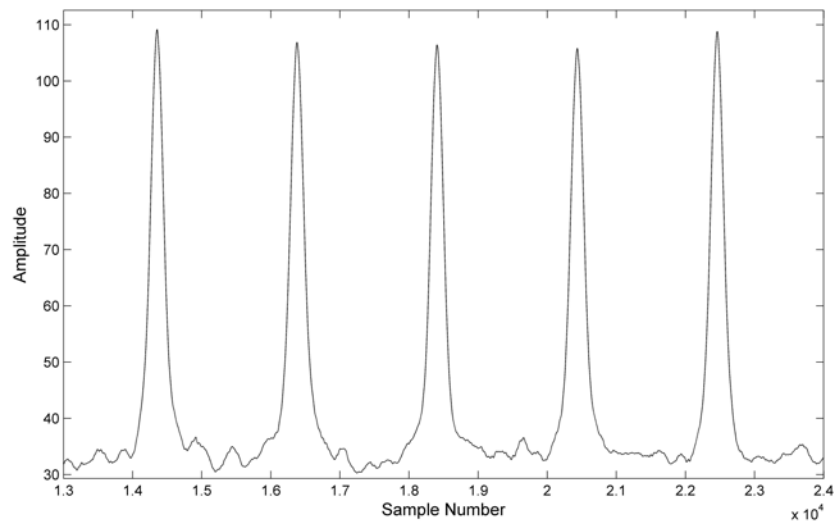


Figure 7.6: Correlation result of five noisy FBGs with their original reflection spectrum.

Chapter 8

Conclusion

Several temperature measurement technologies have been investigated by means of a literature study and it was found that FBGs are the most promising in-core temperature sensing technology currently on the market for the PBMR. Optical fibres were consequently the second part of the literature study, where special attention were given to factors that might influence the operation of an FBG.

Environmental parameters that have a detrimental effect on FBG temperature measurement, such as radiation and pressure were investigated in the literature. It was found that the effects of pressure are known and can be corrected for. The effects of radiation can be minimized through the correct manufacturing techniques and radiation hardening.

FBGs were theoretically investigated and modelled. The models implemented in Matlab can be used to simulate uniform, apodized and WDM of FBGs. Several guidelines were also provided in order to ensure the optimum performance of FBG temperature sensors in noisy and lossy environments. Optimum bandwidth utilization when using WDM FBG systems were discussed.

The test platform that was assembled performed extremely well in providing an environment where FBGs can be tested and characterized. The test platform consists mainly of an optical spectrometer, laser, circulator and fibre heater. A controller was built for the Fibheat 200 heating element capable of controlling the temperature up to 1600°C.

The measured results from the FBGs in the silica fibres correlates very well with the theoretical models and again confirms their validity. WDM of

FBGs performs as elegantly in practice as it does the theory. The apodized FBGs were first calibrated in an oil bath after which they were heated in the Fibheat 200, where higher FBG temperatures can be attained. A consistent and accurate method was formulated for demodulating the FBGs which was used throughout the project.

An interesting discovery was made; when there is a strong temperature gradient across the FBG, spectral widening of the reflection profile occurs. This fact should be taken into account when allocation bandwidth to a certain FBG and choosing a demodulation algorithm.

Finally, the application of the FBG temperature sensing technology to the PBMR have been discussed. Where possible, solutions were provided for some of the engineering challenges in the implementation of such a temperature sensor.

8.1 Future Work

The next step in the project would be to obtain sapphire fibres with FBGs inscribed using femto-second laser radiation. Other methods of FBG inscription also need to be investigated. Temperature measurement with sapphire FBGs up to 1600°C must be demonstrated, after which the effects of pressure and radiation can be investigated. Much work is required in determining the effects of radiation on the operation of FBGs in sapphire.

A suitable cladding for the sapphire fibre has not yet been identified. The long-term survivability of cladding materials currently used is very poor in radiation environments. High temperature cycles have been noted to cause severe cracks and eventual failure of the cladding. Research into the manufacturing of single mode sapphire optical fibres is also required.

Finally, the FBG peak detection and interrogation method need to be automated. In Figure 8.1, the main steps that need to be taken in the development of the FBG sensor system are highlighted. The physical implementation of the FBG temperature system in the PBMR is well beyond the scope of this research. A future vision is nevertheless provided in Figure 8.2, to show what this project is ultimately working towards.

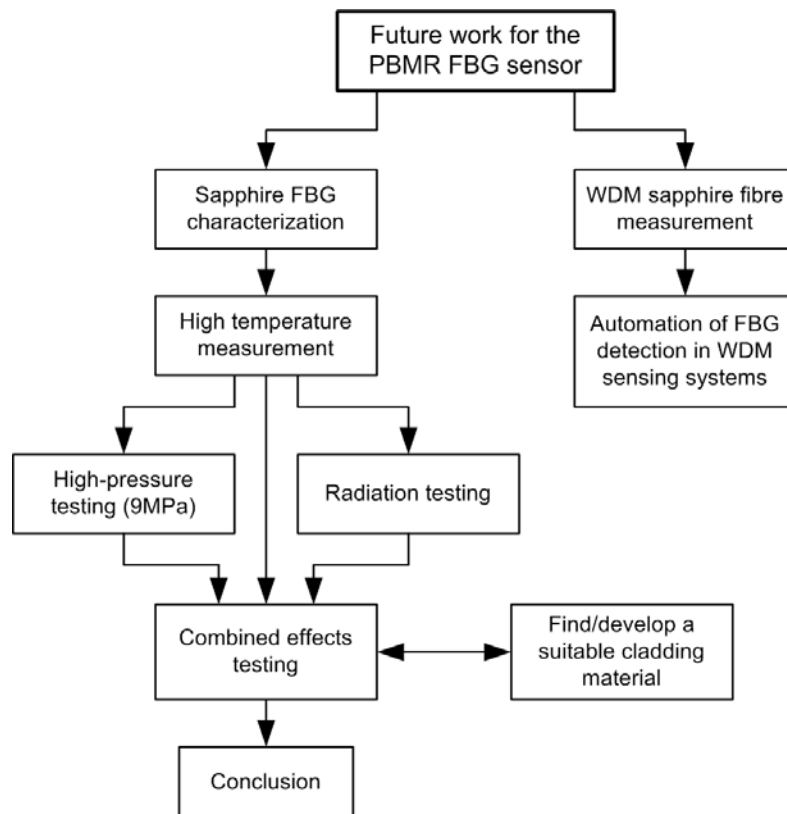


Figure 8.1: A diagram illustrating some of the future work required for the PBMR FBG sensor system.

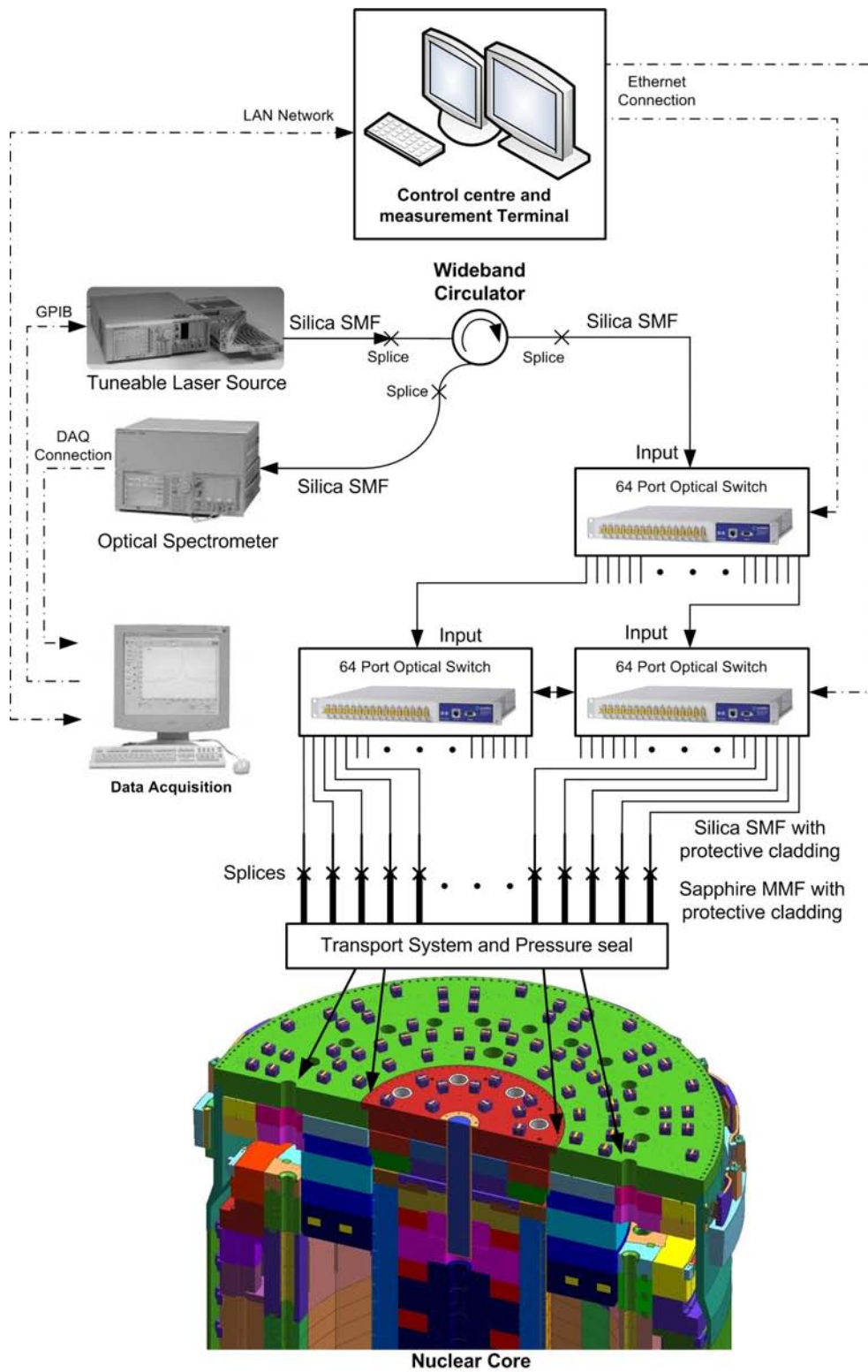


Figure 8.2: A future vision of the FBG temperature measurement system in the PBMR.

Appendices

Appendix A

HRS Wiring Diagram

The correct configuration of the tunable laser source and HRS is critical and a correct wiring diagram of the system is presented in Figure A.1. Please note that the wiring instructions in the manual is incorrect.

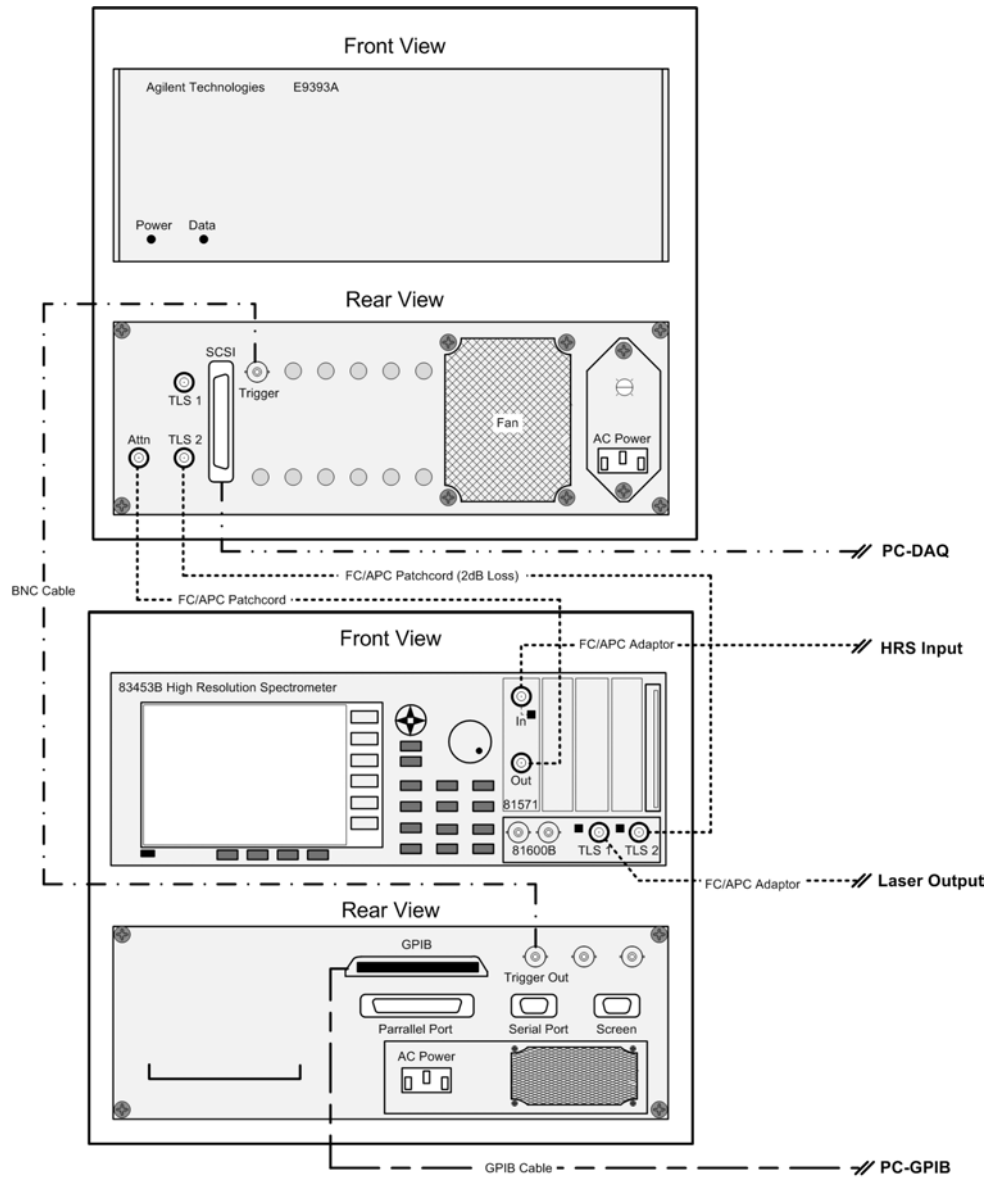


Figure A.1: Illustrating the physical connections to the HRS system. Please note that the wiring instructions in the manual is INCORRECT.

Appendix B

Software Flow Diagrams

Software flow diagrams of the microcontroller software is provided in figures B.1 to B.2. The software flow diagrams of the main control program on the PC is provided in figures B.3 to B.4.

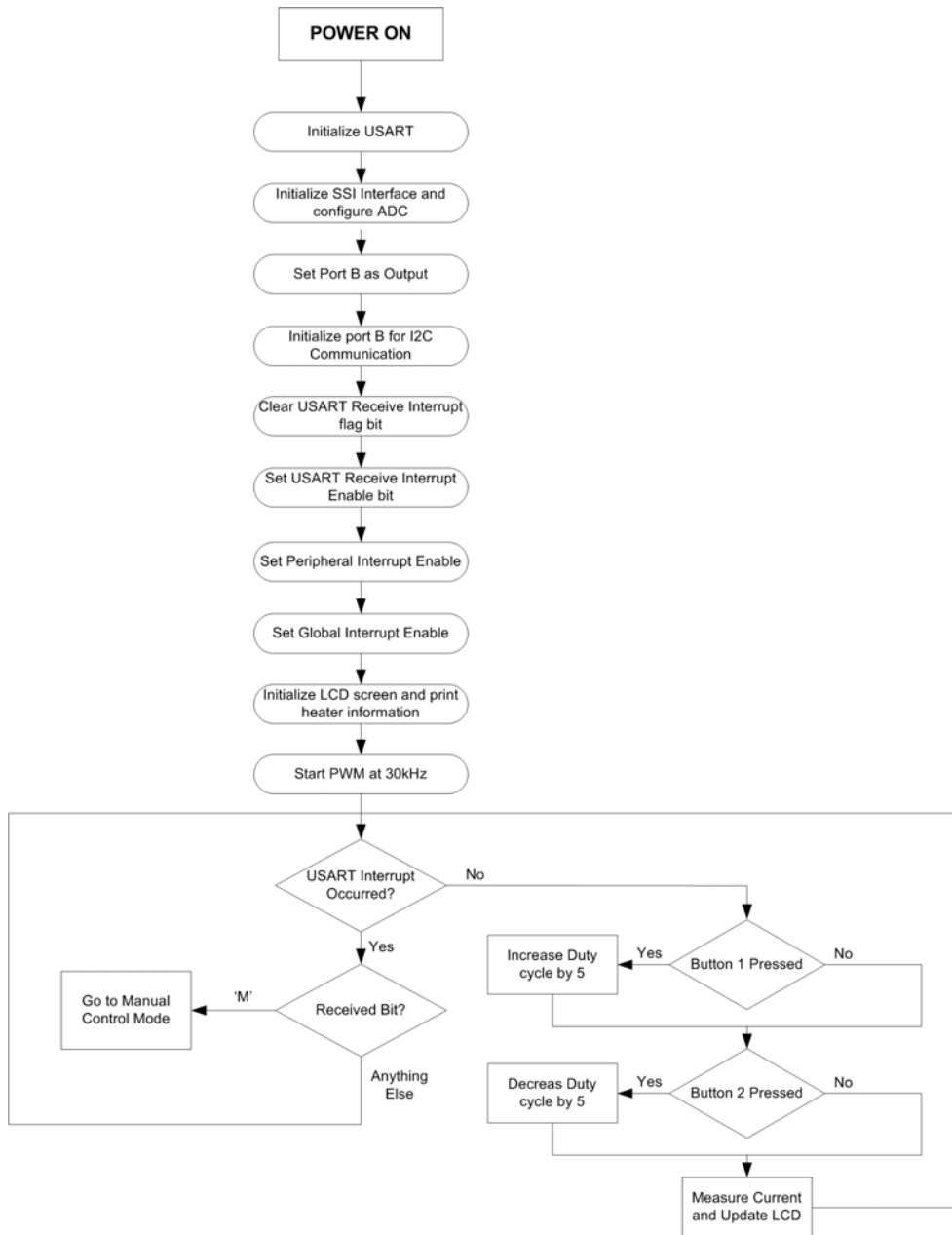


Figure B.1: Software flow diagram of the PIC microcontroller.

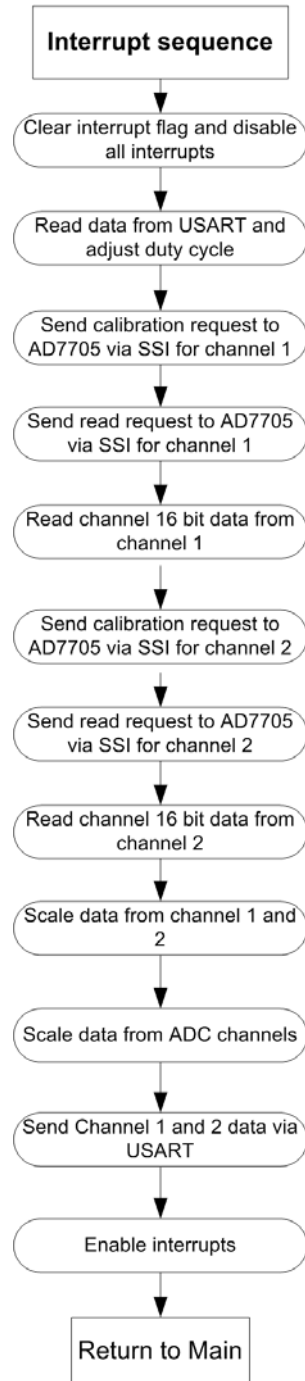


Figure B.2: Software flow diagram for the interrupt sequence of the microcontroller.

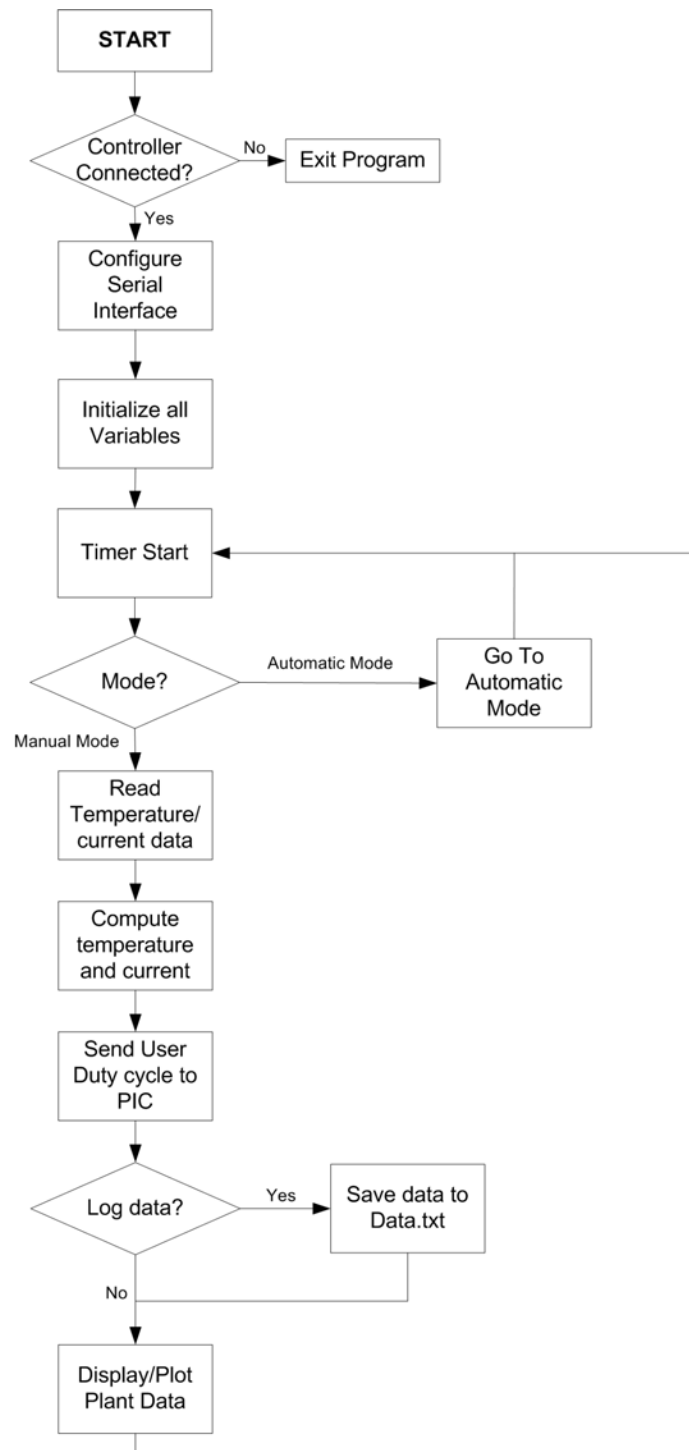


Figure B.3: Software flow diagram of the main control program on the PC.

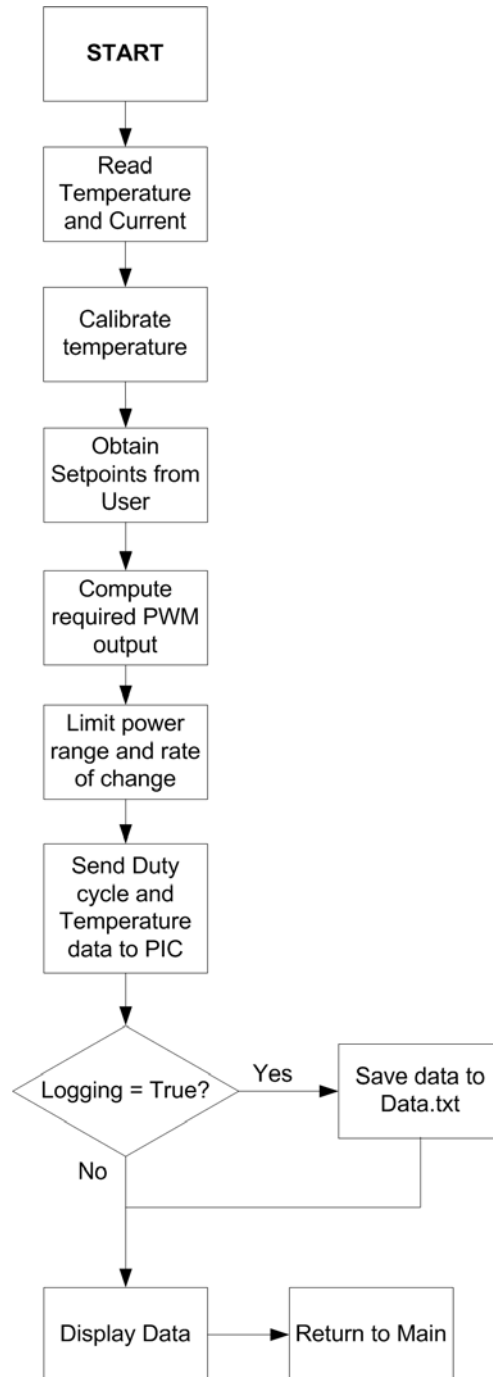


Figure B.4: Software flow diagram of the automatic control system on the PC.

Appendix C

Matlab Code

The transfer matrix method used to solve the coupled mode equations was implemented in Matlab. Many different programs were written to solve different FBG types, however, the core program structure remains the same and is illustrated here.

```
neff = 1.464;           % Effective Refractive Index
fv = 1;                % Fringe visibility
delz = 0.0055*(10^6);  % Uniform Section Length
delnbar = 4.1*(10^(-4)); % Refractive index change
periodn = 529.415;    % Grating Period
pi = 3.14159265358979;

for lambda = 1549.2:.01:1551.8
    f1 = [1 0;0 1];
    for d = 1:500           % Number Of Uniform Sections
        k = exp(-5*(((d-250)/500))^2); % Apodization Factor
        sig=(((2*pi*neff)/lambda)-(pi/periodn)+((2*pi*delnbar)/lambda));
        gammab=(((pi*fv*delnbar*k)/lambda)^2-((sig)^2))^(.5);
        f11=(cosh(gammab*delz)-sqrt(-1)*(sig/gammab)*sinh(gammab*delz));
        f22=conj(f11);
        f21=(((sqrt(-1)*pi*fv*delnbar*k)/(gammab*lambda))*sinh(gammab*delz));
        f12=conj(f21);
        f1=f1*[f11 f12;f21 f22];
    end
end
```

```
P=f1*[1;0];
po=P(1,1);
no=P(2,1);
REF(count)=(abs(no/po))^2;           % Matrix with solution
wave(count)=lambda;
count=count+1;
end
```

Appendix D

C++ Code

In this Appendix an excerpt is provided of the automatic control sequence of the heating element. The C++ code of the control actions together with the variable initializations of the program as a whole is listed here.

```
//-----  
#include <vcl.h>  
#pragma hdrstop  
#include "serial.h"  
#include "Control.h"  
#include <tchar.h>  
#include <math.h>  
#include <stdio.h>  
#include <string>  
#include <stdlib.h>  
#pragma package(smart_init)  
#pragma link "PERFGRAP"  
#include "chart.hpp"  
#pragma resource "*.dfm"  
TForm1 *Form1;  
byte Duty;  
int Voltage, Error, tel, TemperatureSet, TempInt, refA;  
char *read, *read1;  
float Current, CurrentSet, CurrentSetP, CurrentE, CurrentE1, CurrentE2,  
      CurrentE3, Temperature, TempVolt, CurrentVolt, Calibrate, Terror,
```

```

        Terror1, Terror2, NominalC;
byte TemperatureR1, TemperatureR2, Code, Setpoint, DutyP, DutyA;
CSerial serial;
FILE *fp;
bool manual,logging;

//*****Automatic start*****

else
{
    //Write Voltage and Heater Data
    read1 = &DutyA;
    serial.Write(read1);
    LONG Purge (void);
    Sleep(250);
    DWORD dwBytesRead = 0;
    BYTE abBuffer[4] = {0};
    //Read current and temperature data
    serial.Read(abBuffer,sizeof(abBuffer),&dwBytesRead);
    CurrentVolt = abBuffer[0] + 256 * abBuffer[1];
    TempVolt = abBuffer[2] + 256 * abBuffer[3];
    //Scale Temperature voltage
    TempVolt = (TempVolt*2495)/(65535*91.09);
    //Determine Temperature
    if (RadioButton1->Checked)
    {
        if (TempVolt < 0.291) Temperature = 0;
        if ((TempVolt >= 0.291) && (TempVolt < 2.431))
        {
            Temperature = 98.423321+699.71500*TempVolt-
            847.65304*pow(TempVolt,2)+1005.2644*pow(TempVolt,3)
            -833.45952*pow(TempVolt,4)+455.08542*pow(TempVolt,5)
            -155.23037*pow(TempVolt,6)+29.886750*pow(TempVolt,7)
            -2.474286*pow(TempVolt,8);
        }
    }
}

```

```
    if ((TempVolt >= 2.431) && (TempVolt < 13.820))
    {
        Temperature = 213.15071+285.10504*TempVolt-
        52.742887*pow(TempVolt,2)+9.9160804*pow(TempVolt,3)
        -1.2965303*pow(TempVolt,4)+0.1119587*pow(TempVolt,5)
        -0.0060625199*pow(TempVolt,6)+0.00018661696*pow(TempVolt,7)
        -0.0000024878585*pow(TempVolt,8);
    }
}
if (RadioButton2->Checked)
{
    if ((TempVolt >= 0) && (TempVolt < 42.919))
    {
        Temperature = 19.78425*TempVolt-0.2001204*pow(TempVolt,2)
        +0.01036969*pow(TempVolt,3)-0.0002549687*pow(TempVolt,4)
        +0.000003585153*pow(TempVolt,5)-0.00000005344285*pow(TempVolt,6)
        +0.0000000005099890*pow(TempVolt,7);
    }
}
//Compute Current and temperature
CurrentVolt = (CurrentVolt*2.5)/65535;
Current = (CurrentVolt)*27.38*3;
Temperature = Temperature + Calibrate;

//Compute temperature errors
Terror2 = Terror1;
Terror1 = Terror;
Terror = TemperatureSet - Temperature;

//Control action
CurrentSetP = CurrentSet;
CurrentSet = CurrentSetP + 0.9*(Terror-Terror1 + 1*Terror
+0.1*(Terror-2*Terror1+Terror2));

//Set Temperature control limits and maximum rate of change
NominalC = (TemperatureSet + 23.8)/15;
```

```
    if (CurrentSet < (NominalC - 3)) CurrentSet = NominalC - 3;
    if (CurrentSet > (NominalC + 3)) CurrentSet = NominalC + 3;
    if (CurrentSet > 30) CurrentSet = 30;
    if (CurrentSet < 8) CurrentSet = 8;

    //Compute current errors
    CurrentE3 = CurrentE2;
    CurrentE2 = CurrentE1;
    CurrentE1 = CurrentE;
    CurrentE = CurrentSet - (Current-1);

    //Control action
    DutyP = DutyA;
    DutyA = DutyP + 0.3*(CurrentE1-CurrentE2 + 1*CurrentE1
+0.05*(CurrentE1-2*CurrentE2+CurrentE3));

    //Set Current control limits and maximum rate of change
    if (DutyA < (DutyP - 1)) DutyA = DutyP - 1;
    if (DutyA > (1 + DutyP)) DutyA = DutyP + 1;
    if (DutyA > 51) DutyA = 51;
    if (DutyA < 15) DutyA = 15;
}

//*****Automatic end*****
```

Bibliography

- [1] Agrawal, G. P. Nonlinear fibre optics 3rd edition. Academic Press, 2001.
- [2] Andreas O., and Kyriacos K., "Fiber Bragg gratings fundamentals and applications in telecommunications and sensing." Artech House, 1999.
- [3] Benz, S.P., Martinis, J.M., Nam, S.W., Tew, W.L. and White D.R. "A new approach to Johnson noise thermometry using a Josephson quantized voltage source for calibration." Unpublished, 2003.
- [4] Benz, S.P., Martinis, J.M., Dresselhaus, P.D. and Nam, S.W. "An AC Josephson source for Johnson noise thermometry." IEEE Transactions on instrumentation and measurement, VOL 52, NO. 2, April 2002: 545-549.
- [5] Berghmans, Francis, Frans Vos, and Marc Decreton. "Evaluation of three different optical fibre temperature sensor types for application in gamma radiation environments." IEEE Transactions on Nuclear Science, VOL 45, NO. 3, June 1998: 1537-1542.
- [6] Brichard, B., A Fernandez Fernandez, F. Berghmans, and M. Decreton. "Origin of the Radiation-Induced OH vibration band in Polymer-Coated optical fibers irradiated in a nuclear fission reactor." IEEE transactions on nuclear science, Vol. 49, No. 6, December 2002: 2852-2856.
- [7] Brichard, B., Fernandez A., H. Ooms, F. Berghmans, and et. al. "Radiation-hardening techniques of dedicated optical fi-

- bres used in plasma diagnostic systems in ITER." *Journal of Nuclear Materials*, 2004: 1456-1460.
- [8] Brichard, B., H. Ooms, and C. Hendrickx. Round robin tests of optical fibres for diagnostics. SCKCEN Fusion Program, 2002.
- [9] Brichard, B., M. Van Uffelen, A.F. Fernandez, F. Berghmans, M. Decreton, and et al. "Round-robin evaluation of optical fibres for plasma diagnostics." *Fusion Engineering and Design*, 2001: 917-921.
- [10] Brichard, B., P. Borgermans, A. Fernandez Fernandez, K. Lamens, and M. Decreton. "Radiation effect on silica optical fiber exposed to intense mixed neutron-gamma radiation field." *IEEE Transactions on nuclear science*, Vol. 48, No 6, 1 December 2001: 2069-2073.
- [11] Brixy, H., et al. "Temperature, its Measurement and Control in Science and Industry." Vol. 6. New York: American Institute of Physics, 1992. 993-996.
- [12] Browning, W. E. "Methods of measuring temperature in nuclear reactors." *Progress in Nuclear energy, Series IV, Technology, Engineering and safety (Pergamon)*, 1963: Vol. 5.
- [13] Dooryhee, E., J.P. Duraud, and R. Devine. *Radiation induced defects and structural modifications*. New York: Wiley, 2000.
- [14] El-Sherif, M.A., et al. "A novel sapphire fiber- optic sensor for testing advanced ceramics." *Ceramic engineering and Science Proc.* 14, 1993: 437-444.
- [15] Erdogan, and Turan. "Journal of lightwave technology." *Journal of lightwave technology* 15, August 1997: 1277-1294.
- [16] Ferdinand, P., et al. "Optical fibre Bragg grating sensors for structure monitoring within the nuclear power plants." *Proc. SPIE* 2425, 1994: 11-20.
- [17] Fernandez, A.F., B. Brichard, F. Berghams, and M. Decreton. "Dose rate dependencies in gamma-irradiated in-fiber Bragg

- gratings." *IEEE Trans. Nucl. Sci.*, Vol. 49, December 2002: 2874-2878.
- [18] Fernandez, Alberto Fernandez, et al. Multiplexed fibre Bragg grating sensors for in-core thermometry in nuclear reactors. Belgian Nuclear research centre, Belgium, 2001.
- [19] Fernandez, Alberto Fernandez, et al. "Temperature monitoring of nuclear reactor cores with multiplexed fiber Bragg grating sensors." *Optical Engineering*, June 2002: 1246-1254.
- [20] Fredrik, B.H. Jensen, Takada Eiji, Nakazawa Masaharu, Kakuta Tsunemi, and Yamamoto Satoshi. "Consequences of radiation effects on pure silica core optical fibers used for Raman scattering based temperature measurements." *IEEE transactions on nuclear science*, Vol. 45, No. 1, February 1998: 50-58.
- [21] Gifford, Dawn K., Brian J. Soller, Matthew S. Wolfe, and Mark E. Froggatt. "Distributed Fiber-Optic Temperature Sensing using Rayleigh Backscatter." 2006.
- [22] Gill, K., R. Grabit, M. Persello, G. Stefanini, and F. Vasey. "Gamma and neutron radiation damage studies of optical fibres." *Journal of non-crystalline solids*, 1996: 1-15.
- [23] Griscom, D.L. *Applied Physics* 80(4), 1996: 2142.
- [24] Grobnic, Dan, Stephen J. Mihailov, Christopher W. Smelser, and Huimin Ding. "Sapphire fibre Bragg grating sensor made using Femtosecond laser radiation for ultrahigh temperature applications." *IEEE photonics technology letters*, Vol. 16, No. 2, November 2004: 2505-2507.
- [25] Gusarof, A.I., Starodubov, D.S., Berghmans, F., Deparis, O., Defosse, Y., Fernandez, A.F., Decretton, M., Megret, P. and Blondel, M., Design of a radiation-hard optical fibre Bragg grating temperature sensor, *Photonics for space and enhanced radiation environments*, 1999.

- [26] "g-ray-induced Optical attenuation in Ge-doped-silica optical-fibre waveguides." Vol. 78, *Journal of applied physics*, December 1995: 6696-6704.
- [27] Hai, Xiao, Deng Jiangdong, Pickrell Gary, G. May Russel, and Wang Anbo. "Single-Crystal sapphire fibre-based strain sensor for high-temperature applications." *Journal of Lightwave Technology*, Vol. 21, No. 10, October 2003: 2276-2283.
- [28] Hamza, A., A. Ghander, A. Oraby, M. Mabrouk, and J. Guthrie. "Effect of Gamma irradiation on the optical properties of fibres." *J. Ceram. Soc. Jpn.*, 1986: 899-916.
- [29] Hoitink, N.C., R.C. Weddle, and D.C Thompson, "Effects of fast neutron irradiation on the performance characteristics of reactor-grade thermocouples." *Batelle Northwest Rep. BNWL-1365*: Unpublished, 1970.
- [30] Holcomb, David E., Charles L. Britton, Roger A. Kisner, Usha Jagadish, and Michael J. Roberts. Continuous resistance temperature detector calibration using Johnson noise thermometry. Presented as part of the IAEA technical meeting on increasing instrument calibration interval through on-line monitoring technologies, September 2004.
- [31] Holcomb, David E., Roger A. Kisner, and Charles L. Britton. "Ad initio thermometry for long-term unattended space reactor operation." *Proceedings of the Space Nuclear Conference 2005*. San Deigo, California, 2005. 1170.
- [32] Holcomb, David E., Roger A. Kisner, and Charles L. Britton. "Fundamental thermometry for long-term and high-temperature deployment in generation IV reactors." Oak Ridge: Nuclear science and technology division, 2006.
- [33] Jan, J.P. *Galvanometric and thermomagnetic effects in metals*, Vol. 5. San Deigo: Academic, 1957.
- [34] Jundt, D.H., M.M. Fejer, and R.L. Byer. "Characterization of single-crystal sapphire fibers for optical delivery systems." *Applied Physics letters*, 55, 1989: 2170-2172.

- [35] Kapany, M.S. *Fiber optics - Principles and applications*. New York: Academic Press, 1967.
- [36] Kasap, S.O. *Thermoelectric effects in metals: Thermocouples*. Canada: Department of Electrical Engineering University of Saskatchewan, 2001.
- [37] Kist, R. "Fiber optic sensors for networks, in *Selected papers on fiber optic Sensors*." SPIE Optical Engineering Press: Bellingham, 1995: 65-80.
- [38] Kogelnik, H., and C.W. Shank, *Coupled wave theory of distributed feedback lasers*, *Journal of Physics*, Vol. 43, 1972, pp.2327-2336.
- [39] LaBelle, H. E., J. Serafino, and J.J. Fitzgibbon. "Recent developments in the growth of shaped sapphire crystals." *SPIE-Int. Soc. Opt. Eng. Proc. of Spie the Int. Soc. for Opt. Eng*, 1986: 36-40.
- [40] Lai, C.C., Lee, W.Y. and Wang, W.S. "Gamma radiation effect on the Fiber Fabry-Perot Interference sensor." *IEEE Photonics technology letters*, VOL. 15, NR. 8, August 2003: 1132-1134.
- [41] Lopez, N., M. Vitiello, F. Illas, and G. Pacchioni. "Interaction of H₂ with strained rings at the silica surface from ab initio calculations." *J. Applied Physics*, 2000: 56-63.
- [42] Lui, Hanying, Don W. Miller, and Joseph Talnagi. "Gamma radiation resistant Fabry-Perot fiber optic sensors." *Review of scientific instruments*, Volume 73, Number 8, August 2002: 3112-3118.
- [43] Mathieu, F., R. Meier, J. Parent, and W. Schubert. "Thermocouples: recent results on irradiation induced drift and thermocouple noise." *Specialist meeting on the In-core and primary circuit instrumentation of LMFB Reactors*. Warrington, Cheshire, UK: Unpublished, 1976. 344-349.

- [44] Meltz, G., and Morey, W.W., "Bragg grating formation and germanosilicate fibre photosensitivity." International Workshop on Photoinduced Self-Organization Effects in Optical fiber, Quebec City, Quebec, May 10-11, Proceedings SPIE, Vol. 1516, 1991, pp. 185-199.
- [45] McElhaney, S.A., D.D. Falter, R.A. Todd, M.L. Simpson, and J.T. Mihalcz. "Passive (self powered fiber optic sensors)." Conference record of the 1992 IEEE nuclear science symposium and medical imaging conference vol. 1, 1992: 101-103, 192.
- [46] Niay, P., et al. "Behaviour of Bragg gratings, written in germanosilicate fibers, against gamma ray exposure at low dose rate." IEEE Photonics Technology letters, 1994: 1350-1352.
- [47] Nieuwenhove, R. Van, and L. Vermeeren. "Irradiation effects on temperature sensors for the ITER application." Review of scientific instruments, 15 January 2004: 75-83.
- [48] Nubling, R.K., and J. Harrington. "Optical properties of single-crystal sapphire fibers." Applied Optics 32, 1997: 5934-5940.
- [49] Nyquist, H. "Thermal agitation of charge in electric conductors." Phys. Rev. 32, 1928: 110-113.
- [50] Okamoto, Katsunari. Fundamentals of Optical Waveguides. Oxford: Academic Press, 2006.
- [51] Parker, T. R., M. Farhadiroushan, V.A. Handerek, and A.J. Rogers. "Temperature and strain dependence of the power level and frequency of spontaneous Brillouin scattering in optical fibres." Optics Letters, 1 June 1997: 787-789.
- [52] Pedrazzani, Janet Renee. "High-Temperature Displacement Sensor Using a White-Light Scanning Fiber Michelson Interferometer." Master of Science in Electrical Engineering. Blacksburg, Virginia, 16 April 1996.

- [53] Primak, W. "The compacted states of vitreous silica." Studies of radiation effects in solids. New York: Gordon and Breach, Vol. 5, 1975.
- [54] Quinn, T.J. Temperature. Academic Press, 1990.
- [55] Ramaswami, Rajiv, and Kumar N. Sivarajan. Optical Networks a practical perspective. San Deigo: Morgan Kaufmann, 2002.
- [56] Reed, R.P. "Thermocouples: calibration, traceability, instability and inhomogeneity." Thermometry, 1996: 91-114.
- [57] Rochford, K.B. and Shellee, D.D. "Demultiplexing of interferometrically interrogated fiber Bragg grating sensors using Hilbert transform processing." Journal of lightwave technology, Vol. 17, NO. 5, May 1999: 831-836.
- [58] Sanjay, K., G. Shrikant, K.S. Manoj, and T.P.S. Nathan. "Development of distributed fibre optic temperature sensor with sub-metre resolution." Current Science, 10 May 2004: 1202-1204.
- [59] Shen, Yonghang, Limin Tong, Yanqi Wang, and Linhua Ye. "Sapphire-fiber thermometer ranging from 20 to 1800C." Applied Optics, 1 March 1999: 1139-1143.
- [60] Shi, C.Z., et al. "Improving the performance of a FBG sensor network using a genetic algorithm." Sensors and actuators, 1 June 2003: 57-61.
- [61] Sigal, G.H. et al. "Nuclear science." IEEE transactions, 1979: 4796.
- [62] Slabber, J., Theron, W., Matzner, H.D. "Technical description of the PBMR demonstration power plant" Copyright PBMR (Pty) Ltd, 2006.
- [63] Sporea, D., and A. Sporea. "Radiation effects in sapphire optical fibers." Wiley Interscience, 2007: 1356-1359.

- [64] Taylor, E., K. Hulick, J. Battiato, A. Sanchez, J. Winter, and A. Pirich. "Response of germania doped fiber Bragg gratings in radiation environments." *Proc. SPIE*, Vol. 3714, 1999: 106-113.
- [65] Tong, L., Shen, Y., and L. Ye. "Performance improvement of radiation-based high temperature fiber optic sensor by means of curved sapphire fiber." *Sensors and actuators - Physical A75*, 1999: 35-40.
- [66] Vaseliev, S., et al. "Performance of Bragg and long-period gratings written in n-doped and Ge-doped silica fibers under gamma radiation." *Proc. Radecs*, 1997.
- [67] Webster, John G., *Measurement, instrumentation and sensors handbook*. CRC Press in cooperation with IEEE Press, 1999.
- [68] Yariv, A., "Coupled mode theory for guided wave optics." *IEEE Journal of Quantum Electronics*, Vol. QE-9, 1973, pp.919-933.